

---

**Determining the Spin Polarization  
of Heusler Compounds  
via Femtosecond  
Magnetization Dynamics**

---

Diplomarbeit

vorgelegt von

Andreas Mann

aus

Göttingen

Georg-August-Universität zu Göttingen  
I. Physikalisches Institut

2010

**Referent:** Prof. Dr. Markus Münzenberg  
**Koreferent:** Prof. Dr. Thomas Pruschke  
**Abgabedatum:** 12. Januar 2010

# Contents

<b>List of Figures</b>	<b>v</b>
<b>1. Introduction</b>	<b>1</b>
<b>2. Theory and Fundamentals</b>	<b>3</b>
2.1. Landau-Lifshitz-Gilbert equation and macrospin model . . . . .	3
2.2. Energies in ferromagnets . . . . .	6
2.3. Half-metals, polarization, and Heusler compounds . . . . .	9
2.4. Linear and quadratic magneto-optic Kerr effect . . . . .	12
<b>3. Experiment and Models</b>	<b>20</b>
3.1. Pump-probe experiments and induced dynamics . . . . .	20
3.2. Two- and three temperature model . . . . .	24
3.3. Determining the polarization $P$ and expanding the 3TM . . . . .	30
3.4. Comments on the specific heat . . . . .	36
3.5. TRMOKE setup . . . . .	40
3.6. Sample descriptions . . . . .	44
<b>4. Measurements and Analysis</b>	<b>51</b>
4.1. $\text{Co}_2\text{MnSi}$ . . . . .	51
4.2. $\text{Co}_2\text{FeAl}$ . . . . .	58
4.2.1. Ultrafast demagnetization . . . . .	58
4.2.2. QMOKE . . . . .	59
4.3. $\text{CoFeGe}$ . . . . .	66
4.3.1. Ultrafast demagnetization . . . . .	66
4.3.2. Reflectivity experiments . . . . .	69
4.4. $\text{Co}_2\text{MnGe}$ . . . . .	72
4.5. $\text{CoMnSb}$ . . . . .	75
4.6. Comparison of results and X3TM . . . . .	80
<b>5. Summary and Outlook</b>	<b>86</b>

<b>A. Explicit calculations</b>	<b>89</b>
A.1. Analytical solution of the 2TM . . . . .	89
A.2. Analytical solution of the 3TM . . . . .	92
A.3. Solution of the 3TM for high polarization $P$ . . . . .	94
<b>B. Technical details</b>	<b>97</b>
B.1. Calculation of the laser fluence . . . . .	97
B.2. Comments on data processing . . . . .	98
<b>Bibliography</b>	<b>101</b>

# List of Figures

2.1. Illustration of the macrospin model . . . . .	4
2.2. Spin dynamics according to the LL and LLG equations . . . . .	5
2.3. Schematic density of states for a half-metal . . . . .	9
2.4. Illustration of the Heusler $C1_b$ and $L2_1$ structures . . . . .	11
2.5. Reference frame for the discussion of the MOKE . . . . .	15
2.6. Reference frame for the discussion of the QMOKE . . . . .	18
2.7. Decomposition of a hysteresis showing QMOKE . . . . .	19
3.1. Sketch of the laser excitation in terms of the DOS . . . . .	21
3.2. Spontaneous magnetization according to the mean field approximation.	22
3.3. Induced spin dynamics in the out-of-plane field configuration . . . . .	23
3.4. Induced spin dynamics in the in-plane field configuration . . . . .	24
3.5. Sketch of the two temperature model (2TM) . . . . .	25
3.6. Sketch of the three temperature model (3TM) . . . . .	29
3.7. Dependence of $\tau_M$ on $P$ as stated by Müller et al. . . . .	31
3.8. DOS and sketch of 3TM for an ideal half-metal . . . . .	32
3.9. Numerical solution of the 3TM for samples of low and high $P$ . . . . .	33
3.10. Sketch of the expanded three temperature model (X3TM) . . . . .	34
3.11. Dynamics according to the X3TM . . . . .	35
3.12. Realistic model of specific heat for Ni . . . . .	37
3.13. Numerical solutions of the 3TM for different spin specific heats $C_s$ . . . . .	39
3.14. Overview of the TRMOKE setup in use . . . . .	41
3.15. Different geometries for MOKE measurements . . . . .	42
3.16. Sample characterization for $\text{Co}_2\text{MnSi}$ , series CMSXX and He150X . . . . .	45
3.17. Sample characterization for $\text{Co}_2\text{MnSi}$ , series DE90702 . . . . .	46
3.18. Sample characterization for $\text{Co}_2\text{MnSi}$ , series DE90305C . . . . .	46
3.19. Sample characterization for $\text{Co}_2\text{FeAl}$ , series DE90225E . . . . .	48
3.20. Layer stacking for $\text{CoFeGe}$ . . . . .	49
3.21. Layer stacking for $\text{Co}_2\text{MnGe}$ . . . . .	49
3.22. Layer stacking for $\text{CoMnSb}$ . . . . .	50
4.1. Kerr rotation and reflectivity for $\text{Co}_2\text{MnSi}$ , series CMSXX and He150X	52
4.2. Kerr rotation and reflectivity for $\text{Co}_2\text{MnSi}$ , series DE90702 . . . . .	53

## List of Figures

---

4.3. Fitted timescales for Co <sub>2</sub> MnSi samples on Si and MgO substrates . . . . .	54
4.4. Kerr rotation and reflectivity for Co <sub>2</sub> MnSi, series DE90305C . . . . .	55
4.5. Fitted timescales for Co <sub>2</sub> MnSi, series DE90305C . . . . .	56
4.6. Step-like feature for Co <sub>2</sub> MnSi, series CMSXX . . . . .	57
4.7. Kerr rotation and reflectivity for Co <sub>2</sub> FeAl, series DE90225E . . . . .	58
4.8. Fitted timescales for Co <sub>2</sub> FeAl samples (annealing temperature varied) . . . . .	59
4.9. Angular dependence of Kerr rotation for Co <sub>2</sub> FeAl . . . . .	60
4.10. Angular dependence of Hysteresis loops for Co <sub>2</sub> FeAl . . . . .	62
4.11. Measurement points for Co <sub>2</sub> FeAl applying a gradually changed field . . . . .	63
4.12. QMOKE-induced oscillation in Co <sub>2</sub> FeAl . . . . .	64
4.13. Evaluation of the QMOKE-induced oscillation in Co <sub>2</sub> FeAl . . . . .	65
4.14. Kerr rotation and reflectivity for CoFeGe, series LG0611a (not annealed) . . . . .	67
4.15. Fitted timescales for all CoFeGe samples . . . . .	68
4.16. Induced stress wave in CoFeGe . . . . .	70
4.17. Correction of stress wave in CoFeGe . . . . .	71
4.18. Kerr rotation and reflectivity for Co <sub>2</sub> MnGe samples on MgO(100) . . . . .	72
4.19. Fitted timescales for all Co <sub>2</sub> MnGe samples . . . . .	73
4.20. Comparison of evaluation methods for Co <sub>2</sub> MnGe samples . . . . .	74
4.21. Fluence dependence of Kerr rotation for CoMnSb . . . . .	76
4.22. Comparison of evaluation methods for CoMnSb . . . . .	77
4.23. Stress pulse in the reflectivity of the half Heusler CoMnSb . . . . .	79
4.24. Demagnetization of samples with different polarization . . . . .	81
4.25. Relation between demagnetization time $\tau_M$ and polarization $P$ . . . . .	82
4.26. Comparison of experimental data to expanded 3TM . . . . .	83

# Chapter 1.

## Introduction

The young field of research of ultrafast magnetization dynamics has been attracting great interest ever since the first observation of demagnetization on the femtosecond timescale by Beaurepaire et al. in the mid-nineties [BMDB96]. There is a practical interest in the exploitation of femtosecond processes for new applications in electronics, for example in magnetic recording media which provide non-volatile information storage capacity accessible at high switching rates. But besides the promising practical applications, the femtosecond regime of magnetization dynamics provides an abundance of new physical phenomena yet to be fully explored and explained. Even to date, the fundamental processes involved in the magnetization dynamics are under debate. Recently, progress has been made using microscopic models to explain different aspects of the magnetization dynamics [ACFK<sup>+</sup>07, KMDL<sup>+</sup>09], but a uniform picture is still lacking.

This thesis aims at giving more insight into various aspects femtosecond magnetization dynamics. Of peculiar interest is the development of a method to determine the spin polarization of a magnetic material from its demagnetization behavior, based on important work performed by Müller et al. [MWD<sup>+</sup>09]. Materials of high spin polarization, referred to as half-metallic materials, are of interest because they provide an easy means of providing spin-polarized currents. These currents can be used to carry and process information in the framework of so-called spintronics. The different types of Heusler compounds investigated in this thesis are suited to provide insight into the range of intermediate polarization, which is up to now only sparsely covered by pump-probe investigations. The measurements on Heusler compounds reveal interesting physics by themselves, and the results are used to expand the existing model describing the impact of the spin polarization on the magnetization dynamics.

In chapter 2 of this thesis, the fundamental concepts of the physics necessary to understand the investigations of performed in this thesis are discussed. The concept of half-metallicity is introduced, and the material class of Heusler com-

pounds is presented. Also, the magneto-optic Kerr effect is discussed in details, including the quadratic contributions that can be measured in certain Heusler compounds. The experiment is explained in chapter 3, starting with the description of the mechanism of triggering femtosecond dynamics using a laser pulse. The phenomenological two- and three temperature models used to describe the magnetization dynamics on ultrashort timescales are discussed in detail. This leads to the discussion of the connection between the spin polarization and the timescale of demagnetization. In this context an expansion of the three temperature model is proposed, which is investigated in the course of this thesis. Finally, descriptions of the Heusler samples under investigation are given. These samples include the compounds  $\text{Co}_2\text{MnSi}$ ,  $\text{Co}_2\text{FeAl}$ ,  $\text{CoFeGe}$ ,  $\text{Co}_2\text{MnGe}$ , and  $\text{CoMnSb}$ , where for every compound different aspects of the dynamics are of interest. The results of the experiments are presented in chapter 4, sorted by material class. The measured demagnetization curves are evaluated using the three temperature model. The demagnetization behavior is discussed with regard to the available structural data. Besides this, the pump-probe experiment is demonstrated to be able to investigate trends in the demagnetization behavior of compounds of varying composition. Furthermore, additional phenomena occurring in the measurements are investigated, where the dynamics quadratic magneto-optic Kerr effect is particularly noteworthy.

The performed measurements are also evaluated and interpreted in a more fundamental context in chapter 4.6. The entirety of the results of the pump-probe measurements is used to develop a method to determine the spin polarization directly from the fit of the demagnetization time according to the three temperature model. In addition, it is demonstrated the the proposed expansion of the three temperature model is able to explain the wide variety of magnetization dynamics exhibited by samples of different polarizations. Finally, certain statements are made how the expanded model can be further verified, and how it is possible to include it in other current models describing magnetization dynamics. These statements can also be seen as proposals for further steps in the development of a uniform description of magnetization dynamics on the femtosecond timescale.

# Chapter 2.

## Theory and Fundamentals

### 2.1. Landau-Lifshitz-Gilbert equation and macrospin model

In this section the fundamental mechanisms that are necessary to understand the magnetization dynamics studied in this thesis will be introduced. Detailed descriptions have been given by Miltat et al. [MAT02] and by Djordjević [Djo06]. The discussion starts by deriving the equation of motion for a single spin in a magnetic field  $\vec{B}$ . From quantum mechanics it is known that the timely evolution of the expectation value of the spin operator  $\hat{S}$  is given by

$$i\hbar \frac{d}{dt} \langle \hat{S} \rangle = \langle [\hat{S}, \hat{\mathcal{H}}] \rangle. \quad (2.1)$$

The Hamiltonian  $\hat{\mathcal{H}}$  simply comprises a Zeeman term,

$$\hat{\mathcal{H}} = \frac{g\mu_B}{\hbar} \hat{S} \cdot \vec{B}. \quad (2.2)$$

Here,  $g \approx 2.002$  denotes the g-factor of the electron and the Bohr magneton  $\mu_B = \hbar e / 2m_e$  is defined to be positive. The equation of motion is derived by inserting the commutation relation for angular momenta,  $[\hat{S}_i, \hat{S}_j] = i\hbar \varepsilon_{ijk} \hat{S}_k$ .<sup>1</sup> The commutator on the right-hand side of Eq. (2.1) is calculated via

$$[\hat{S}_i, \hat{\mathcal{H}}] = \frac{g\mu_B}{\hbar} [\hat{S}_i, \hat{S}_j] B_j = -ig\mu_B \varepsilon_{ijk} \hat{S}_j B_k,$$

---

<sup>1</sup> It is assumed that the reader is familiar with the use of the Levi-Civita symbol. Note that the Einstein summation convention will be used wherever it is convenient.



**Figure 2.1.:** In the context of the macrospin model, a large set of quantum mechanical spins  $\hat{S}_i$  (left) is treated as a single macroscopic magnetic moment  $\vec{M}$  (right), which precesses in the external field  $H$ .

yielding the cross-product

$$\frac{d}{dt} \langle \hat{\vec{S}} \rangle = -\frac{g\mu_B}{\hbar} \left( \langle \hat{\vec{S}} \rangle \times \vec{B} \right). \quad (2.3)$$

Next the so-called *macrospin model* is introduced, which assumes that the magnetization  $\vec{M}$  is related to  $\langle \hat{\vec{S}} \rangle$  via the magnetic moment  $\mu_e$  of the electron:

$$\vec{M} = \mu_e \langle \hat{\vec{S}} \rangle = -\frac{g\mu_B}{\hbar} \langle \hat{\vec{S}} \rangle \quad (2.4)$$

This equation has a simple interpretation, illustrated in Fig. 2.1: In the thermodynamic limit (i.e. for a large number of spins) the observed magnetization will behave as if produced by a single macroscopic magnetic moment. The macrospin model therefore connects the quantum mechanical description of a single electron spin with the classical picture of magnetization known from electrodynamics.

Inserting the macrospin model (2.4) into the result for the timely evolution of Schroedinger's equation one arrives at

$$\frac{d}{dt} \vec{M} = -\mu_0 \frac{g\mu_B}{\hbar} (\vec{M} \times \vec{H}) = -\gamma_0 (\vec{M} \times \vec{H}), \quad (2.5)$$

where also the vacuum relation  $\vec{B} = \mu_0 \vec{H}$  has been used. Equation (2.5) is known as the *Landau-Lifshitz equation* (LL). It states that a magnetic moment will precess around an external magnetic field, as long as the field is not parallel to the moment. This motion is illustrated on the left-hand side of Fig. 2.2. It can easily be seen that Eq. (2.5) also implies conservation of  $|\vec{M}|$ .

To complete the picture of the fundamental dynamics a phenomenological element will be added to Eq. (2.5). The constant precession of a magnetic moment around an external field implied by the Landau-Lifshitz equation is definitely not a realistic state of equilibrium. The precession predicted by the equation is



**Figure 2.2.:** Spin dynamics according to the Landau-Lifshitz (LL) and Landau-Lifshitz-Gilbert (LLG) equations.

indeed observed in the experiment. However, its amplitude is damped and the magnetic moment will eventually align parallel to the external field – which is the above-mentioned state of equilibrium. The respective expansion of Eq. (2.5) was proposed by Gilbert, who introduced an ohmic-type damping term. The expanded equation reads

$$\frac{d}{dt}\vec{M} = -\gamma_0 (\vec{M} \times \vec{H}) + \frac{\alpha_G}{M_s} \left( \vec{M} \times \frac{d\vec{M}}{dt} \right). \quad (2.6)$$

$M_s$  is the saturation magnetization and the dimensionless quantity  $\alpha_G$  is known as the *Gilbert damping parameter*. Equation (2.6) is known as the *Landau-Lifshitz-Gilbert equation* (LLG) and successfully describes the magnetization dynamics on the picosecond (ps) time scale. The damped precessional motion is illustrated in the right-hand side of Fig. 2.2. Note, however, that the LLG does not include the description of longitudinal fluctuations of the magnetization, i.e. the reduction of the absolute value of the magnetization. These fluctuations can be derived using a *microspin approach* based on the *Landau-Lifshitz-Bloch equation* (LLB). The LLB has recently proven itself able to perform micromagnetic simulations of spin dynamics [ACFK<sup>+</sup>07].

As an alternative, the magnetization dynamics can also be derived using the Lagrangian formalism, but the damping term has to be inserted manually as well [MAT02]. Still there is a comment to be made about the field  $\vec{H}$  in the LLG. While for simplicity the vacuum relation  $\vec{B} = \mu_0 \vec{H}$  was used, the field acting on the magnetization is in reality composed of various contributions; this is expressed by using the term *effective field*  $\vec{H}_{\text{eff}}$ . The LLG will be taken up later on, but first the energetical properties of a ferromagnet, which are the key to understanding the emergence of  $\vec{H}_{\text{eff}}$ , will be discussed.

## 2.2. Energies in ferromagnets

The concept of the effective field  $\vec{H}_{\text{eff}}$  introduced above is easily understood in terms of the free energy  $\mathcal{F}$  of a ferromagnet [MAT02]. The field itself contains several physical effects, which can be grouped into four contributions: the *external field*, the *exchange field*, the *anisotropy field*, and the *demagnetization field*:

$$\vec{H}_{\text{eff}} = \vec{H}_{\text{ext}} + \vec{H}_{\text{exch}} + \vec{H}_{\text{anis}} + \vec{H}_{\text{demag}} \quad (2.7)$$

The effective field and its several contributions are more rigorously defined via the free energy of a magnet using the thermodynamical relation

$$\vec{H}_{\text{eff}} = -\frac{1}{\mu_0} \frac{\partial \mathcal{F}}{\partial \vec{M}}.$$

Now, a brief discussion of the individual contributions shall be given. The external field  $\vec{H}_{\text{ext}}$  gives rise to a contribution of the already mentioned Zeeman form:

$$\mathcal{F}_{\text{ext}} = -\mu_0 \vec{M} \cdot \vec{H}_{\text{ext}}$$

This term favors a parallel alignment of every individual spin to the external field and thus a homogeneous magnetization.

The exchange field regards the pairwise interaction of the spins. The corresponding energy is of the form

$$\mathcal{F}_{\text{exch}} = \frac{A}{M^2} (\nabla \vec{M})^2.$$

It prefers the parallel alignment of each pair of spins in the magnetic material. Here,  $A$  denotes the material-dependent exchange constant. The form of  $\mathcal{F}_{\text{exch}}$  can be derived from the Heisenberg Hamiltonian  $\mathcal{H}_{\text{exch}} = -J_{ij} \hat{S}_i \hat{S}_j$  by transformation to a continuous magnetization.<sup>2</sup> The value of  $A$  is of course related to the exchange constant  $J_{ij}$  of the Heisenberg Hamiltonian. Note that this contribution does not favor a specific direction.

The next contribution considers the (bulk) anisotropy of the sample. The anisotropy field is in general governed by the magneto-crystalline anisotropy, which reflects the crystallographic symmetries of the magnet. The spins are coupled to the crystal lattice and its symmetries via spin-orbit coupling. Here, the discussion will be limited to the case of uniaxial anisotropy. The corresponding free energy

---

<sup>2</sup> Note that again the summation convention is used.

consists of several contributions reflecting the symmetry. In this context, the first two will be noted, namely:

$$\mathcal{F}_{\text{anis}} = K_1 \sin^2(\theta - \theta_1) + K_2 \sin^4(\theta - \theta_2).$$

$K_1$  and  $K_2$  are the anisotropy constants and  $\theta - \theta_i$  denotes the angle between the magnetization and the prominent axis. Note that the symmetry axes may in general have a different orientation for the second and the fourth order term.<sup>3</sup> Due to crystal symmetry only even terms are allowed in the anisotropy energy. Most of the time one can also neglect the fourth order term. The sign of the remaining constant  $K_1$  is then solely responsible for determining whether the prominent axis is an easy axis or a hard axis. The anisotropy energy is also influenced by magneto-elastic contributions; however, these can be treated in the same way. An interesting feature of the anisotropy energy is that while its absolute value is much smaller than e.g. the exchange energy, it nevertheless determines the actual direction of the magnetization with no external field present. This is simply due to the fact that it is the only non-isotropic contribution to the free energy for a bulk ferromagnet. Another important point is that the anisotropy constants  $K_i$  strongly depend on the lattice temperature. It is this fact that will turn out to be of fundamental importance for triggering the precessional motion according to the LLG in pump-probe experiments, as is discussed in chapter 3.1.

Given the fact that the studies in this thesis are performed on thin films, also the demagnetization field of the samples has to be taken into account. The terms *stray field* and *shape anisotropy field* are used as synonyms for the demagnetization field. The origin of this contribution lies in the interaction of the magnetization of the thin film with the magnetic field it produces. This is easily understood in terms of Gauss' law for the magnetic flux  $\vec{B}$ :

$$\nabla \vec{B} = \mu_0 \nabla (\vec{H} + \vec{M}) \stackrel{!}{=} 0$$

The demagnetization field can thus be defined via  $\nabla \vec{H}_{\text{demag}} = -\nabla \vec{M}$ . It turns out that the field can be expressed in an elegant way using the *demagnetization tensor*  $\underline{N}$ :

$$\vec{H}_{\text{demag}} = -\underline{N}\vec{M}$$

In the case of an infinitely extended thin film, the only non-zero entry of the

---

<sup>3</sup> This is e.g. the case if the first term is caused by strains induced by lattice mismatch between sample and substrate and the second term by the fourfold symmetry of the lattice, whose orientation differs from the direction of substrate strain.

demagnetization tensor is the component along the  $z$ -axis (the film normal). The associated demagnetization energy is then given by

$$\mathcal{F}_{\text{demag}} = \frac{1}{2}\mu_0 \left(\vec{M} \cdot \vec{e}_z\right)^2$$

The demagnetization energy is thus responsible for the phenomenon of *shape anisotropy*. Note that in the field one almost always encounters in-plane anisotropy, whereas out-of-plane anisotropy remains an exception for continuous films.

All the terms can now be summed up to receive the equation for the total free energy of the ferromagnet, which is the analogon to Eq. (2.7):

$$\mathcal{F}_{\text{fm}} = \mathcal{F}_{\text{ext}} + \mathcal{F}_{\text{exch}} + \mathcal{F}_{\text{anis}} + \mathcal{F}_{\text{demag}} \quad (2.8)$$

As mentioned above, this equation is used to derive the effective field. Both the exact form and the relative magnitude of its four contributions determine the magnetic properties of a sample. Since the state of equilibrium is the state where  $\vec{M} \parallel \vec{H}_{\text{eff}}$ , the dynamics will have to be induced by tilting the magnetization away from the direction of the effective field. Having done so, one can observe the precessional motion according to the LLG (2.6). These considerations will be taken up again in chapter 3.1.

There is a final warning that has to be made to avoid misunderstandings: The concept of the free energy as a (thermodynamic) potential stems from the formalism of equilibrium thermodynamics. However, the magnetization dynamics that are discussed in this thesis are mostly of a non-equilibrium nature. And even in the static case, there are severe constraints on the concept. While the free energy is helpful in understanding the different contributions that affect the behavior of magnetic samples, it is not possible to apply the standard thermodynamic approach. This is easily seen by the fact that one would normally expect to be able to derive the magnetization of the sample from the free energy. However, this is not possible, because the real magnetization almost never lies in the global minimum of  $\mathcal{F}$  that is obtained from thermodynamics, but rather in a local minimum. This is, in fact, a necessity if one wants the model of a magnetic sample to show effects like hysteresis, and in particular a remanence, i.e. a behavior, where the minimum of  $\mathcal{F}$  is not unambiguous, but rather determined by the previous history of the sample. Therefore, the models introduced in chapter 3.2 to describe magnetization dynamics use a different approach, describing the dynamics via coupled heat baths.

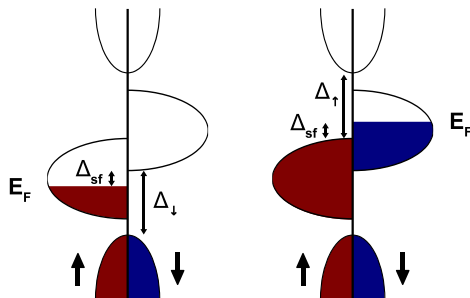


**Figure 2.3.:** Schematic density of states for a half-metal of type Ia (left) and type Ib (right), after Coey and Venkatesan [CV02]. Note that besides the band gap  $\Delta_{\uparrow\downarrow}$  there is also a spin-flip energy  $\Delta_{sf}$ , which denotes the energy necessary to enable electrons excited from the Fermi level to perform spin-flips.

## 2.3. Half-metals, polarization, and Heusler compounds

In the past years major efforts have been made to predict and substantiate the half-metallic nature of certain materials. After a brief introduction to half-metallicity in general the class of *Heusler compounds* will be presented, quite a number of which are promising candidates for half-metals.

The physical definition of a half-metal is simple: An ideal half-metal is a material with a *spin gap*  $\Delta_{\uparrow\downarrow}$  at the Fermi level, which is a band gap *for one type of spin only*. The half-metal is therefore 100% spin-polarized. This basic definition is in the literature classified as a type I half-metal, if remaining electrons at the Fermi energy  $E_F$  are itinerant, whereas a type II half-metal features localized electrons. The subtypes a and b denote whether these electrons are situated on the spin up or the spin down side, respectively.<sup>4</sup> A sketch of the spin-resolved density of states (DOS) for type I half-metals is depicted in Fig. 2.3. It illustrates the position of the spin gap  $\Delta_{\uparrow\downarrow}$  around the Fermi energy  $E_F$ . Besides the spin gap, there is also a smaller *spin-flip energy*  $\Delta_{sf}$ , which corresponds to the energy necessary to excite an electron from the Fermi level to the upper end of the spin gap. This is a gauge for the energy that is required to enable the electron to perform a spin-flip. The parameter  $\Delta_{sf}$  will play an important role in the expansion of the conventional model for spin dynamics, as is discussed later on in chapter 3.3.

Further types of half-metals are discussed in the literature [CV02]. However, the type I and II definitions are sufficient for understanding all phenomena pre-

<sup>4</sup> By convention, the 'up' and 'down' directions of the spins are used for majority and minority spins, respectively.

sented in the context of this thesis. They fall under the category of *half-metallic ferromagnets* (HMF), having a ferromagnetic band structure for the remaining spins at  $E_F$ , whereas different types of half-metals can have band structures similar to semi-metals or semiconductors. At this point it should also be noted that there is a necessary condition for a material to be a half-metal called the *integer spin moment criterion*. It simply states that the presence of a gap at the Fermi level requires the numbers  $n_\uparrow$  and  $n_\downarrow$  of electrons per unit cell to be an integer. Therefore, the difference is also an integer, resulting in an integer spin moment.<sup>5</sup> However, this condition is not sufficient, because half-metallicity is also influenced by effects like spin-orbit coupling.

Defining the quantitative degree of half-metallicity, a major issue is the definition of the *spin polarization*  $P$ . While it is obvious that  $P = 100\%$  for an ideal half-metal, a general definition has to regard certain subtleties. In the context of this thesis, the discussion will be restricted to the simple definition

$$P := \frac{N_\uparrow - N_\downarrow}{N_\uparrow + N_\downarrow}, \quad (2.9)$$

where  $N_\uparrow$  and  $N_\downarrow$  denote the number of electrons at the Fermi level in the up and down band, respectively. In a more general approach these quantities are weighted by powers of the Fermi velocity  $v_{F,\uparrow/\downarrow}$  to account for the mechanisms involved in measuring  $P$ . In general, experimental values of the spin polarization depend on the measurement technique applied and thus care has to be taken when comparing different results for  $P$ . In addition, the established techniques for measuring  $P$  – namely photoemission, point-contact magneto-resistance, tunneling magneto-resistance, Andreev reflection, and the Meservey-Tedrov technique – all have their own experimental challenges. The method of determining  $P$  via an all-optical pump-probe experiment is discussed in this respect later on. Nevertheless, the common approach seems to be to perform a band structure calculation to identify a potential half-metal and then check its experimental value of  $P$  applying different techniques. This way has also been chosen with many Heusler compounds, which will now be discussed.

To understand the great scientific interest in compounds one can first take a look at the band structure of a typical transition metal ferromagnet. While e.g. the elements cobalt and nickel have fully polarized  $3d$  bands, they are not half-metals due to the fact that the Fermi level crosses the (unpolarized)  $4s$  band, lowering the polarization well below 100% to values of about 40%, which for themselves

---

<sup>5</sup> Of course, this argumentation only holds for  $T = 0$ .

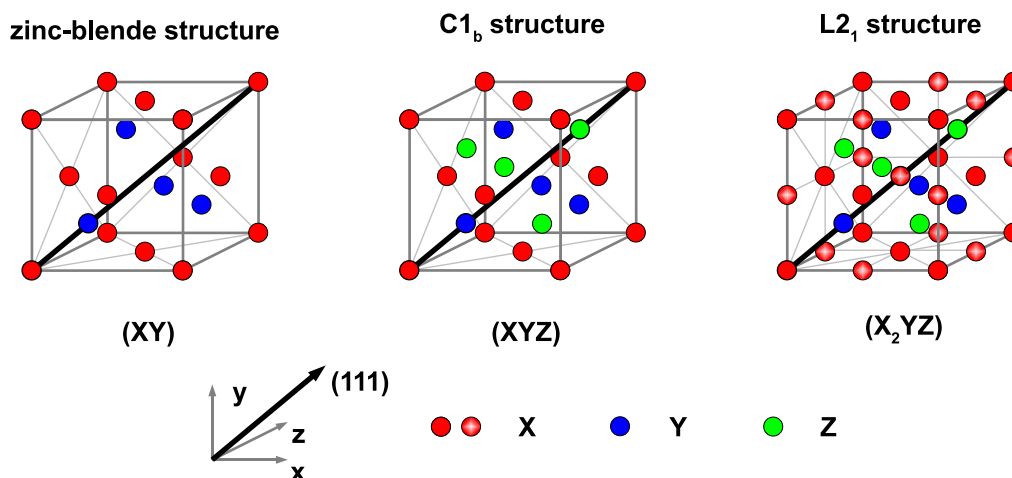


**Figure 2.4.:** Illustration of the Heusler  $C1_b$  and  $L2_1$  structures. A unit cell is shown for different structures, where the thick black line indicates the (111) direction, i.e. the diagonal of the cell. Starting from the zinc-blende structure (left) with chemical formula  $XY$ , one arrives at the half Heusler  $C1_b$  structure by positioning a third fcc sublattice of  $Z$  atoms at three quarters of the diagonal. The full Heusler  $L2_1$  structure is derived by adding a fourth fcc sublattice of  $X$  atoms at the middle of the diagonal. Note that in the right picture there are actually four whole atoms per sublattice included in the unit cell, because as usual only part of the atoms in the corners and planes are actually inside the cell.

are only achieved because of  $sd$  hybridization [CS04]. On the other hand, the hybridization can be employed to gain access to the complete polarization of the  $d$  band by either raising the  $4s$  band above the Fermi level or depriving the system of electrons until the Fermi level is situated below the  $4s$  band.<sup>6</sup> Both ways can be realized by the transition from a pure metal to an alloy (or a compound). The class of Heusler compounds is of particular interest in this respect, because Heusler compounds offer a wide range of composition variations while retaining their crystal structure.

Heusler compounds can be divided into two classes: the *full Heusler compounds* and the *half Heusler compounds*. Both types of compounds consist of three elements: A high-valence transition or noble metal atom  $X$  (often cobalt), a low-valence transition metal  $Y$  (e.g. manganese or iron), and a  $sp$ -type element  $Z$  (like silicon or aluminum). The full Heusler compounds are of the chemical formula  $X_2YZ$ , while the half Heusler compounds are of the form  $XYZ$ . The corresponding crystal structures of highest order are the  $L2_1$  structure and the  $C1_b$

<sup>6</sup> These facts are the reason there are no half-metals among pure elements at all.

structure, respectively.<sup>7</sup> Figure 2.4 illustrates the two Heusler structures. These structures are easily understood if one starts from the well-known zinc-blende structure. The zinc-blende structure is a fcc Bravais lattice with a dual basis of  $(0, 0, 0)$  and  $(1/4, 1/4, 1/4)$ . Adding a third atom at position  $(3/4, 3/4, 3/4)$  to the basis one arrives at the  $C1_b$  structure, where the sites are occupied by X, Y, and Z atoms respectively. Adding a second atom of type X at the position  $(1/2, 1/2, 1/2)$  the  $C1_b$  structure is transformed into the  $L2_1$  structure. Note that the latter has an additional inversion symmetry center with respect to the former, which will have an impact on the electronic structure.

## 2.4. Linear and quadratic magneto-optic Kerr effect

In this section *magneto-optic Kerr effect* is discussed, which is the tool of choice for examining magnetization dynamics. While the Kerr effect is long known, it is amazing how essential it proves for today's high-end physics: It provides a fast, simple, and contact-free method for measuring magnetic properties, even capable of capturing dynamics beyond the picosecond range. This section starts with an overview of the discovery and the early interpretation of the Kerr effect, which involves the linear MOKE with a signal nearly proportional to the sample magnetization. However, only recently scientific discussion became more focused on the *quadratic magneto-optical Kerr effect* (QMOKE), which is of second order in the magnetization. In particular, it has been discussed to what extent it reveals details on the process of magnetization reversal. The QMOKE is easily observable in a number of systems which have cubic symmetry. Therefore, it will also appear in the study of (full) Heusler compounds. It will also come to mention that for anisotropic samples it features an extremely strong angular dependence.

The reflective magneto-optic effect that affects polarized light is named after its discoverer, John Kerr. In his original publication [Ker77], Kerr already stresses the strong relation of this effect to the magneto-optic effect in transmission, the *Faraday effect*. The main aspect exploited when performing MOKE measurements is that a polarized beam of light reflected off a magnetic surface will have its plane of polarization rotated by an amount proportional to the magnetization of the surface, thus making this magnetization measurable. Considering the general case of an elliptically polarized beam (which includes circular and linear polarizations as special cases), one observes that both the direction of the main axis of the

---

<sup>7</sup> Note that in particular the highly ordered  $L2_1$  structure may change to different structures depending on external parameters promoting disorder.

ellipse and its ellipticity are changed. These observations are summarized in the *complex Kerr amplitude*

$$\phi := \theta - i\epsilon,$$

which comprises the *Kerr rotation*  $\theta$  and the *Kerr ellipticity*  $\epsilon$ .

Now to a note on the underlying physics. Consider an elliptically polarized plane wave, expressed here by its electric field vector  $\vec{E}$ :

$$\vec{E}(\vec{r}, t) = \vec{E}_0 \cdot e^{i(\vec{k}\vec{r} - \omega t)}$$

If the beam WLOG travels along the  $z$  direction, the *polarization vector*  $\vec{E}_0$  can be represented in the orthonormal basis  $\{\vec{E}_l, \vec{E}_r\}$  of the circularly polarized states

$$\vec{E}_l = \frac{1}{\sqrt{2}} \begin{pmatrix} 1 \\ i \\ 0 \end{pmatrix}, \quad \vec{E}_r = \frac{1}{\sqrt{2}} \begin{pmatrix} 1 \\ -i \\ 0 \end{pmatrix}.$$

These states are the helicity eigenstates of the photon (called left- and right-handed, respectively). The eigenstates are converted into each other via a point reflection, which is also called *parity transformation*<sup>8</sup>. If it is stated that the Kerr effect changes the ellipticity of a polarized light beam, this is only possible by treating left- and right-handed helicities differently. To be more precise, the indices of reflection  $n_l$  and  $n_r$  for the two helicities must be different due to the effect of the magnetization, a phenomenon denominated as *magnetic circular dichroism* (MCD). This in turn means that parity must be violated in the considered system. This violation is caused by the magnetization of the medium reflecting the beam. The magnetization  $\vec{M}$  is a pseudovector,<sup>9</sup> i.e. it is invariant under parity transformations. Therefore, light of a certain helicity in a medium of magnetization  $\vec{M}$  behaves identically to light of the opposite helicity experiencing the magnetization  $-\vec{M}$ . This in turn corresponds to a discrimination between the helicity eigenstates, breaking parity invariance.

After this very fundamental discussion the classical derivation of the Kerr effect is outlined. It will turn out that classical electrodynamics can only explain the Kerr effect in non-magnetic media, so a quantum mechanical description will

---

<sup>8</sup> This part of the discussion follows the nomenclature of particle physics to avoid the ambiguity concerning the definitions of 'left' and 'right' encountered in optics.

<sup>9</sup> As a reminder: This is easily seen from the Lorentz force  $\vec{F}_l = q\vec{v} \times \vec{B}$ . From the fact that  $\vec{F}_l$  and  $\vec{v}$  are polar vectors and the properties of the cross-product it becomes clear that  $\vec{B}$  (and thus also  $\vec{M}$  and  $\vec{H}$ ) are pseudovectors.

follow afterwards. From the macroscopic point of view, the MCD is reflected by an asymmetric form of the *dielectric tensor*  $\underline{\underline{\varepsilon}}$ , where the well-known relation

$$\vec{D} = \underline{\underline{\varepsilon}} \cdot \vec{E} \quad (2.10)$$

holds.<sup>10</sup> A valuable instrument for the discussion is the application of *Onsager's principle* [Ons31a, Ons31b], which states

$$\varepsilon_{ij}(\vec{H}) = \varepsilon_{ji}(-\vec{H}).$$

This makes it possible to write  $\underline{\underline{\varepsilon}}$  as an expansion in  $\vec{H}$ , which to linear order reads

$$\underline{\underline{\varepsilon}} \approx \underline{\underline{\varepsilon}}^{(0)} + \underline{\underline{\varepsilon}}^{(1)} \quad \text{with} \quad \underline{\underline{\varepsilon}}^{(1)} = \begin{pmatrix} 0 & \varepsilon_{12} & -\varepsilon_{13} \\ -\varepsilon_{12} & 0 & \varepsilon_{23} \\ \varepsilon_{13} & -\varepsilon_{23} & 0 \end{pmatrix}, \quad (2.11)$$

where  $\underline{\underline{\varepsilon}}^{(0)} = \varepsilon_0$  is (in the present case of a cubic crystal) of zeroth order, i.e. a scalar. From this explicit expression it can be seen that (as for any antisymmetric  $3 \times 3$  matrix) there exists a vector  $\vec{g} \in \mathbb{R}^3$  such that

$$\underline{\underline{\varepsilon}}^{(1)} \cdot \vec{E} = \vec{E} \times \vec{g}.$$

Since the magnetic field provides the only distinct external direction,  $\vec{g}$  must be parallel to  $\vec{H}$  and also proportional to its magnitude, thus  $\vec{g} = \alpha \vec{H}$ . When put into Maxwell's equations, this finally leads to the aforementioned dichroism [MLBZ89]:

$$n_{r,l}^2 = \varepsilon_0 \mp i\alpha H_{\parallel} \quad (2.12)$$

Here,  $H_{\parallel}$  denotes the absolute value of the projection of  $\vec{H}$  onto the vector  $\vec{n}$  associated with the index of refraction, which points along the wave vector  $\vec{k}_T$  of the transmitted beam. The situation is illustrated in Fig. 2.5. The main result up to now is that the classical Kerr effect is proportional to the portion of the magnetic field  $\vec{H}$  which is parallel to the transmitted beam of light. Furthermore, it is now possible to derive the quantitative values of the complex Kerr rotation

---

<sup>10</sup> The relations following from Maxwell's equation have been discussed extensively in literature [MLBZ89, Mey03].

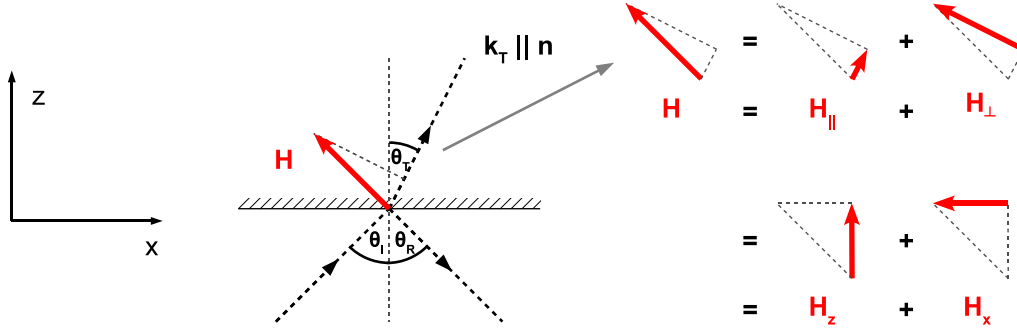


Figure 2.5.: Reference frame for the discussion of the MOKE

$\phi_{p,s}$  for  $p$ - and  $s$ -polarized light:

$$\phi_p = \frac{\alpha}{\varepsilon_0 - 1} \cdot \frac{H_z \sqrt{\varepsilon_0 - \sin^2(\theta_I)} + H_x \sin(\theta_I)}{\varepsilon_0 - \sin^2(\theta_I) - \sqrt{\varepsilon_0 - \sin^2(\theta_I)} \cdot \sin(\theta_I) \tan(\theta_I)} \quad (2.13)$$

$$\phi_s = \frac{\alpha}{\varepsilon_0 - 1} \cdot \frac{H_z \sqrt{\varepsilon_0 - \sin^2(\theta_I)} - H_x \sin(\theta_I)}{\varepsilon_0 - \sin^2(\theta_I) + \sqrt{\varepsilon_0 - \sin^2(\theta_I)} \cdot \sin(\theta_I) \tan(\theta_I)} \quad (2.14)$$

In these equations, the Kerr rotation is already expressed by means of the  $x$ - and  $z$ -components of the magnetic field  $\vec{H}$  and the angle of incidence  $\theta_I$ , which are all depicted in Fig. 2.5. The Kerr rotations  $\theta_{p,s}$  can be calculated via

$$\theta_p = -\Re\{\phi_p\} \quad \text{and} \quad \theta_s = \Re\{\phi_s\}.$$

Now it is time to turn towards the quantum mechanical explanation of the Kerr effect. It is of utmost importance to do so, because the derivation given above has two issues. First, it states that  $\theta \sim H$ , in contrast to the experimental observation that  $\theta \sim M$  for ferromagnets. This is, however, not a problem, if it holds that  $\vec{H} \sim \vec{M}$ , which is given in the framework of this simplified classical derivation. In that case, one can simply redo the symmetry considerations given above replacing  $\vec{H}$  with  $\vec{M}$ . Nevertheless, the classical picture completely fails to correctly estimate the value of the Kerr rotation  $\theta$ . The estimated values for  $\theta$  are about five to six orders of magnitude (!) too low. The reason for this becomes obvious in the discourse on MOKE given by Argyres [Arg55]. The classical discussion of MOKE is often explained by the electrons of the medium being forced into circular motion with orientation determined by the left and right circular polarized fractions of the incident light beam. The MOKE is invoked by the Lorentz force induced by the external magnetic field  $\vec{H}$ , which acts differently depending on the orientation

of the circular motion, changing its radius and ultimately the index of refraction for the helicities of the light. In ferromagnetic materials this effect is in principle present, too, but it is overridden by the effect of *exchange interaction* and *spin-orbit coupling*. Argyres explains this mechanism in terms of band structures. The exchange interaction causes magnetism, i.e. a state where the numbers of spin up and spin down electrons are unequal. The spin-orbit coupling between the *angular momentum*  $\vec{L}$  and the already mentioned spin angular momentum  $\vec{S}$  spawns an additional energy term of the form

$$E_{SO} = \xi \vec{L} \cdot \vec{S}. \quad (2.15)$$

The constant  $\xi$  is called the *spin-orbit coupling parameter*. The coupling can be interpreted as an effective magnetic field of vector potential

$$\vec{A}_{SO} \sim \vec{\mu} \times \vec{E}_{\text{intr}},$$

where  $\vec{\mu}$  is the magnetic moment of the electron and  $\vec{E}_{\text{intr}}$  is the intrinsic electric field of the medium, i.e. the field exerted by its Coulomb potential. The 'magnetic field' produced by this effect is of sufficient magnitude to explain the observed strength of the Kerr rotation. In practice, its contribution is often only detectable when the magnetic material is already saturated. Also, the giant contribution of the spin-orbit coupling to the MOKE has the welcome side effect that the rotation caused directly by an external field will be negligible in the case of a ferromagnet. In addition, it is now clear that for a non-magnetic material the classical explanation is sufficient, because the magnetic moments in the medium are compensated pairwise and their magnetic moments cancel each other.

In the following, rather than reproducing the whole quantum mechanical calculation of the MOKE, only the important steps will be sketched. The magneto-optical properties are calculated via determining the current density  $\vec{j}$  induced by the incident light beam. This is achieved by applying perturbation theory to the Hamiltonian of a one electron system, yielding the *conductivity* and *polarizability tensors*  $\sigma_{ij}$  and  $\alpha_{ij}$ , respectively. The result is the macroscopic current density  $\vec{J}$  which reads

$$\vec{J} = \underline{\underline{\sigma}} \cdot \vec{E} + \underline{\underline{\alpha}} \cdot \frac{\partial \vec{E}}{\partial t}.$$

Note that the tensors can both be expanded analogously to Eq. (2.11). Since the calculation performed is semiclassical, the results for the Kerr rotation  $\theta$  and the Kerr ellipticity  $\epsilon$  are obtained in a similar way compared to the classical derivation of MOKE: First, one obtains the expression for  $\theta$  and  $\epsilon$  as a function of the index

of refraction  $n_{l,r}$  with regard to the helicity of the incident light. One easily identifies  $\theta$  and  $\epsilon$  to be proportional to a sum containing the first order terms of the expansions for  $\underline{\alpha}$  and  $\underline{\alpha}$ . These in turn are (by definition) proportional to the magnetization  $\vec{M}$  of the sample, which is the desired result. The discussion is ended here to give more room for the description of the QMOKE.

To start the discussion of the quadratic Kerr effect, the reader should again take a look back at the expansion of the dielectric tensor in Eq. (2.11). It has to be stated that in principle the expansion performed can be continued to second order. The notation will be slightly altered from now on and the dielectric tensor is written as

$$\varepsilon_{ij} = \varepsilon_{ij}^{(0)} + \varepsilon_{ij}^{(1)} + \varepsilon_{ij}^{(2)} = \varepsilon_0 + K_{ijk}M_k + G_{ijkl}M_kM_l, \quad (2.16)$$

where  $K_{ijk}$  and  $G_{ijkl}$  denote the linear and quadratic magneto-optic tensors. An elaborate discussion of these tensors for various crystal symmetries has been performed by Vishnovsky [Vis86]. As stated above, the Kerr effect in ferromagnets stems from spin-orbit coupling. In fact, the magnitude of the Kerr effect is proportional to the spin-orbit coupling constant  $\xi$ . Now remember that it was found that in the classical derivation the Kerr effect is proportional to  $H_{\parallel}$  (see Eq. (2.12)). Therefore it is clear that due to its analogous structure the quantum mechanical calculation results in a proportionality to  $M_{\parallel}$ . This, however, is only true for the first order contribution. In second order a Kerr signal is measured which is sensitive to the perpendicular component  $M_{\perp}$  of the magnetization and also proportional to  $\xi^2$ . Osgood et al. explained this phenomenon with the polarization dependence of transitions between the energy bands split by spin-orbit coupling [OIBC<sup>+</sup>98]. This leads to the conclusion that the occurrence of a strong QMOKE signal indicates a large contribution to the spin-orbit coupling which is of second (or higher) order [HBG<sup>+</sup>07].

The discussion of second order MOKE is continued by elaborating on the actual dependence of the QMOKE on the sample orientation and the magnetization components. For this discussion the frame of reference shown in Fig. 2.6 is used where the magnetization vector  $\vec{M}$  lies 'in-plane' and the magnetic field  $\vec{H}$  is applied in the x-direction, which lies in the plane of incidence of the probing light beam. The plane of incidence again corresponds to the xz-plane (as in Fig. 2.5), which is perpendicular to the sample surface. The sample is rotated (also in-plane) by an angle  $\alpha$ . The value  $\alpha = 0$  corresponds to a direction of high symmetry (e.g. the (100) direction of a L2<sub>1</sub> lattice) oriented parallel to the magnetic field. The magnetization is split into the longitudinal component  $M_L$ , which is parallel to

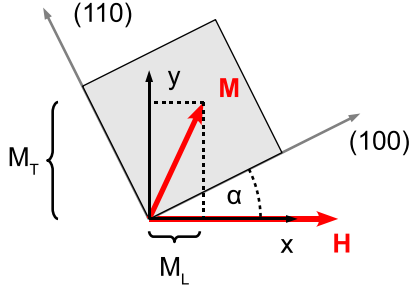


**Figure 2.6.:** Reference frame for the discussion of the QMOKE.

the plane of incidence, and the transverse component  $M_T$ , which is perpendicular to the plane of incidence.<sup>11</sup> While Osgood et al. stated that the QMOKE signal depends on a term proportional to  $M_L M_T$ , it was later stated by Postava et al. that there is also a contribution proportional to  $M_L^2 - M_T^2$  [PHP<sup>+</sup>02]. It is the latter term that is directly dependent on the sample orientation  $\alpha$  and incloses the anisotropy of the QMOKE.

From the symmetry considerations by Vishnovsky [Vis86] it can be seen that in the case of a cubic crystal (i.e. in particular for all  $L2_1$  Heusler structures) the dielectric tensor from Eq. (2.16) only has five degrees of freedom: To zeroth order, there is the single element  $\varepsilon_0 = |n|^2$ , where  $n$  is the complex index of refraction. To first order there is also only one element  $K = K_{123} = K_{312} = K_{231}$ . Finally, there are three elements in the second order term, namely  $G_{11}$ ,  $G_{12}$  and  $2G_{44}$ .<sup>12</sup> This yields the final form for the tensors of different order in Eq. (2.16):

$$\begin{aligned}\varepsilon_{ij}^{(0)} &= \delta_{ij}\varepsilon_0 \\ K_{ijk} &= \varepsilon_{ijk}K \\ G_{ijkl} &= \delta_{ij}\delta_{jk}\delta_{kl}G_{11} + \delta_{ij}\delta_{kl}(1 - \delta_{jk})G_{12} + \delta_{ik}\delta_{jl}(1 - \delta_{ij})G_{44}\end{aligned}\quad (2.17)$$

From this one is able to calculate the dielectric tensor and thus the complex Kerr amplitude  $\phi_{s,p}$  for  $s$ - and  $p$ -polarized light. To keep things short, only the final result stated by Hamrle et al. [HBG<sup>+</sup>07] is discussed, which reads

$$\begin{aligned}\phi_{s,p} &= \pm A_{s,p} \left[ 2G_{44} + \frac{\Delta G}{2}(1 - \cos(4\alpha)) + \frac{K^2}{\varepsilon_0} \right] M_L M_T \\ &\mp A_{s,p} \frac{\Delta G}{4} \sin(4\alpha) (M_L^2 - M_T^2) \mp B_{s,p} K M_L.\end{aligned}\quad (2.18)$$

The *optical weighting functions*  $A_{s,p}$  and  $B_{s,p}$  are even and odd functions of the angle of incidence  $\theta_I$ , respectively. Also, the *magneto-optical anisotropy parameter*  $\Delta G = G_{11} - G_{12} - 2G_{44}$  was introduced, which is present in all non-isotropic samples (i.e. above all the samples are neither polycrystalline nor amorphous).

Equation (2.18) can be used to clearly identify the different contributions to the Kerr signal. First, there is the last term, which is proportional to  $M_L$ . It

<sup>11</sup> Note that the directions of  $M_L$  and  $M_T$  are fixed and in particular independent of  $\alpha$ .

<sup>12</sup> The short-suffix notation applied here reads '11  $\equiv$  1111', '12  $\equiv$  1122', and '44  $\equiv$  2323'.

describes the known longitudinal MOKE.<sup>13</sup> The longitudinal MOKE is sometimes abbreviated LMOKE; this is not to be mixed up with the term 'linear MOKE'. Secondly, the Kerr rotation contains the above-mentioned contributions proportional to  $M_L M_T$  and  $M_L^2 - M_T^2$ . Thirdly, the QMOKE signal alone is sensitive to the sample orientation  $\alpha$ , that is to say via the magneto-optical anisotropy parameter (hence the name). It is this dependence that allows for inferences on the microscopic process of magnetization reversal [HBG<sup>+</sup>07]. Finally, the quadratic contribution proportional to  $K^2/\varepsilon_0$  stems from the squaring of  $\varepsilon_{ij}$ . Thus it is present even if the quadratic magneto-optic tensor vanishes, but its amplitude is assumed to be small in the majority of cases. Note, however, that it does not indicate an intrinsic quadratic dependence of  $\varepsilon_{ij}$ . In theory, the tensor elements from Eq. (2.17) can be determined from angular-dependent QMOKE measurements exploiting Eq. (2.18).

It is still necessary to find a method to decompose the measured Kerr signal into its linear and quadratic parts. Fortunately, this turns out to be quite simple, and is discussed for example by Hamrle [HBG<sup>+</sup>07]. In Fig. 2.7, an example for the decomposition of a measured hysteresis curve (black) into its asymmetric (red) and symmetric (blue) parts is shown for a  $\text{Co}_2\text{FeAl}$  sample.<sup>14</sup> At every point of the hysteresis, the strength of the QMOKE is proportional to the difference of the two branches of the symmetric part for a constant applied field. The small artifacts of the QMOKE appearing at  $\mu_0 H = H_C$  are treated in the course of the discussion of the QMOKE in chapter 4.2.

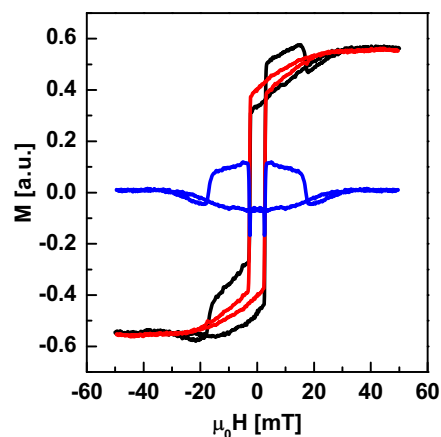


*Figure 2.7.: A hysteresis showing QMOKE is decomposed into its asymmetric and symmetric parts.*

All the theoretical background needed to discuss the QMOKE is now available. Nevertheless, the analysis of the angular dependence of the QMOKE is hampered by the fact that the contributions are in general extremely sensitive even to small changes in angle when the magnetization is near the prominent symmetry directions of a sample.

<sup>13</sup> For more details on MOKE measurement geometries cf. section 3.5.

<sup>14</sup> The same sample is used in chapter 4.2 for the detailed investigation of the QMOKE.

# Chapter 3.

## Experiment and Models

### 3.1. Pump-probe experiments and induced dynamics

In the following, the physics of the experimental technique of choice for this thesis, the *all-optical pump-probe experiment*, is presented. The discussion is kept slightly more general than would be necessary to solely understand the measurements performed in this thesis. This way, the reader gets an idea of how the regime of dynamics this thesis focuses on is embedded in the overall scheme of spin dynamics.

The all-optical pump-probe technique applies laser pulses of very short duration both to excite magnetization dynamics in thin film samples and to measure them with high spatial and temporal resolution. One can simply use the beam from a pulsed laser and split it into two beams, the *pump* and the *probe*, where the former carries the majority of the total laser power and the latter only as much as is needed for low-noise detection. During the discussion, the effect of the pump pulse is explained in detail; concerning the probe pulse only its use as a measurement tool is of interest. As discussed in chapter 3.5, the experimental challenge lies in extracting a clear signal from the probe beam and interpreting its behavior.

While the spatial resolution of the experiment can be adjusted using focusing optics, the temporal resolution is roughly given by the pulse length  $w$  of the laser beam. Today's high-end pulse lasers are scratching the attosecond (as) regime, with pulse durations of several tens of as ( $1 \text{ as} \hat{=} 10^{-18} \text{ s}$ ). Systems with pulse durations in the 10 fs range are already commercially available. One sweeping success of the all-optical pump-probe technique is the possible implementation of *time resolved MOKE* (TRMOKE) investigations. These investigations require a timely delay  $\Delta\tau$  between the pump and probe which is simply realized by altering the optical path length of the pump with respect to the probe beam. One can imagine the TRMOKE measurement performed by the probe as a stroboscopic illumination of the state of magnetization of the sample at variable delay times. One of the

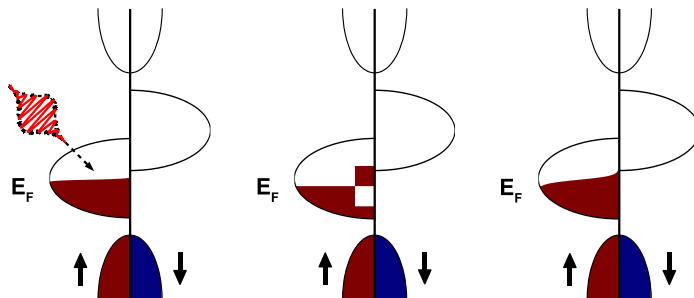


**Figure 3.1.:** Sketch of the laser excitation in terms of the DOS: Before the laser pulse arrives, the sample is assumed to be in thermal equilibrium, so the electrons obey a Fermi-Dirac distribution (left). The laser pulse excites a number of electrons to non-thermal states (middle). The excited electrons thermalize until a new equilibrium with a Fermi-Dirac distribution at a higher temperature is reached (right). The width of the distribution is exaggerated for clarification.

probably best known examples of a TRMOKE measurement is the one performed by Beaurepaire et al. [BMDB96] in the mid-nineties. The authors investigated the demagnetization of a thin nickel film and for the first time observed dynamics on the sub-ps timescale. Following this rather recent discovery, ultrafast dynamics have attracted a great amount of scientific interest among solid state physicists.

Now to the description of the dynamics triggered by the pump pulses. The process is sketched in terms of the density of states (DOS) in Fig. 3.1. As the sample is hit by a laser pulse, it will demagnetize to a certain degree, whereby it takes the following steps: It is assumed that directly before the pulse hits the sample ( $\Delta\tau < 0$ ), the sample is in equilibrium (in a thermodynamical sense), i.e. in particular its electrons occupy states according to the Fermi-Dirac distribution for room temperature  $T_R \approx 300$  K. The very short pulse of high fluence  $F$  (in units of power per unit area) arriving at  $\Delta\tau = 0$  will transfer its energy to the electrons of the sample. At the beginning each absorbed photon, which in the setup used carries the energy  $h\nu \approx 1.5$  eV, will excite one single electron. Thus a portion of the electrons will be transformed into *non-thermal electrons* (sometimes called *hot electrons*), meaning they occupy states of high energy and do not follow the Fermi-Dirac distribution. The non-thermal electrons typically last for timescales up to  $\Delta\tau \sim 100$  fs. After this the electrons will have reached a new state of equilibrium, this time again according to the Fermi-Dirac distribution, but for a higher temperature  $T_R + \Delta T_e$ . To understand how this now triggers the spin dynamics observed in the experiment, a description within the scope of the heat baths for electrons, spins, and lattice is chosen, as it is used for the three temperature model introduced in chapter 3.2. The electrons are in general coupled to both the lattice and the spin system of the sample. Since both the lattice and

the spins are nearly inert on the timescale of electron thermalization, they are still at room temperature  $T_R$ . Now the electrons will transfer part of their energy to the lattice and the spin system.<sup>15</sup>

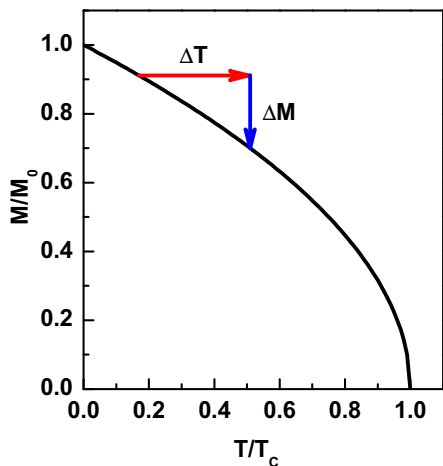


**Figure 3.2.:** Spontaneous magnetization according to the mean field approximation.

Of special interest is the energy transfer to the spin system. The increase of the spin temperature  $T_s$  will lead to a demagnetization of the sample. In the mean field approximation, a *critical exponent* of  $1/2$  is derived for the temperature dependence of the demagnetization [Sch00]. This leads to the known square-root-like  $M(T)$  curve for the spontaneous magnetization shown in Fig. 3.2, where the arrows indicate the change in magnetization  $\Delta M$  caused by the temperature increase  $\Delta T$ . However, this is a very coarse approximation. On the one hand, it is derived for  $H_{\text{ext}} = 0$ . It becomes especially bad when  $T + \Delta T$  comes close to  $T_C$ , where the critical isotherm predicts a behavior of  $M/M_0 \sim \sqrt[3]{H_{\text{ext}}}$ , while the  $M(T)$  curve in Fig. 3.2 states a vanishing magnetization. On the other hand, it is derived from equilibrium thermodynamics, whereas the system under study is definitely in a non-equilibrium state. Still, the estimate of the temperature increase is not bad as a first approximation. Nevertheless, a thorough calculation would at least have to regard the lateral temperature profile in the sample to connect the demagnetization to the sample temperature. Finally, all three systems will approach a new equilibrium at a temperature  $T + \Delta T$ . On an even larger timescale, the thermal diffusion of the heat will lead to a cooling of the heated spot, which finally reaches room temperature again.

While thus far only the effect of the heated electrons has been considered, the dynamics in the picture of thermal effects of the sample will now be discussed briefly. This will lead to the magnetic precession mentioned during the discussion of the LLG in chapter 2.1. First, it is assumed that the external field  $\vec{H}_{\text{ext}}$  is applied at an angle  $\phi_H > 0$  with respect to the sample surface and observe the effect of sample heating by the pump pulse. The situation is illustrated in Fig. 3.3. In equilibrium (i.e for  $\Delta\tau < 0$ ) the effective field  $\vec{H}_{\text{eff}}$  and thus the magnetization  $\vec{M}$  will be slightly tilted out of the sample surface towards the direction of the

<sup>15</sup> While this description of energy transfer may seem rather short, it will be elaborated on intensively in the next section.

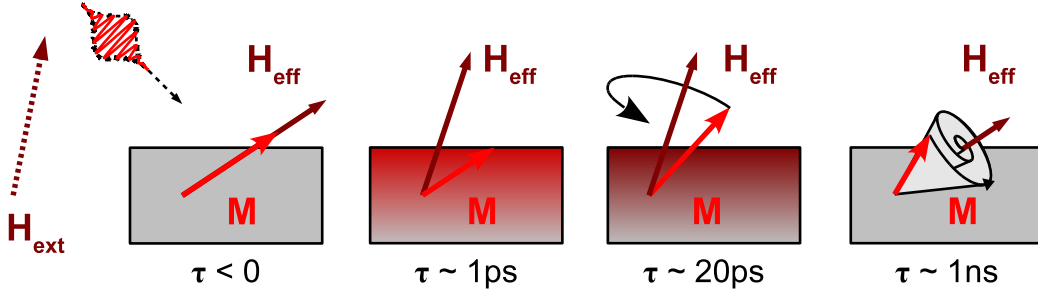


**Figure 3.3.:** Induced spin dynamics in the out-of-plane field configuration. The heating by the laser pulse (first picture) shifts the effective field for a short time (anisotropy pulse). This demagnetizes the sample (second picture), but it also tilts the magnetization out of its original direction (third picture). After the anisotropy pulse vanishes and the sample cools down sufficiently, the effective field returns to its original direction and the magnetization, which is still tilted out, starts to precess according to the LLG (fourth picture).

external field. The reader is reminded that the highly temperature-dependent anisotropy constants  $K_i$  of the sample contribute to the effective field. The lattice is now heated up following the arrival of the laser pulse. Its temperature, which is commonly referred to as 'the temperature of the sample', will therefore change considerably on a timescale of  $\Delta\tau \sim 1$  ps. This triggers a change of the anisotropy constants that effectively reduces the anisotropy of the sample. The mechanism can be described as an *anisotropy field pulse* that is added to the effective field, but lasts only for about 20 ps [Djo06]. During this time, the magnetization, which was still in its original position and therefore out of equilibrium with respect to the temporarily altered effective field, will start to precess around the new  $\vec{H}_{\text{eff}}$ . While the anisotropy pulse lasts too short to allow for the magnetization to equilibrate with the altered  $\vec{H}_{\text{eff}}$ , the magnetization will now also be out of equilibrium when the anisotropy field pulse vanishes and the effective field returns to its original position. This provides the displacement of the magnetization that is required to trigger the precession according to the LLG, as discussed in section 2.1. The length of this precession depends on the Gilbert damping parameter  $\alpha$  and is e.g. for nickel of the order of 1 ns. Note that the form of the precession is only determined by  $\alpha$  and the original effective field  $\vec{H}_{\text{eff}}$ , but not by the anisotropy pulse. The latter only determines the initial precession amplitude and influences the starting phase of the precession.

The general part of the description of TRMOKE measurements using the all-optical pump-probe technique is now finished. At this point it has to be clarified, that (i) as will be seen further on, for the investigations presented it is mostly the dynamics in the ultrashort ( $< 1$  ps) regime that is of interest, and (ii) in

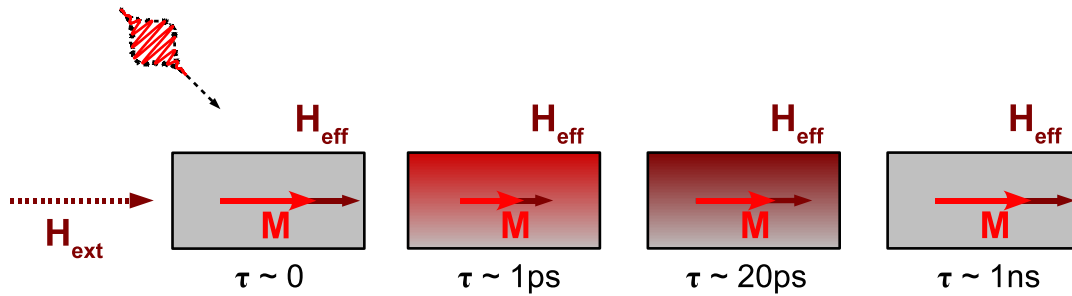


**Figure 3.4.:** Induced spin dynamics in the in-plane field configuration. In this case, the heating by the laser pulse leads to a demagnetization of the sample, but the direction of the magnetization remains in the plane of the sample. The following cooling process is accompanied by the remagnetization of the sample.

the performed experiments, the external field is applied in-plane and therefore no precession of the magnetization is observed.<sup>16</sup> This leads to a slightly different picture (shown in Fig. 3.4), because the sample is only demagnetized by the pulse, and the direction of the magnetization remains in the plane of the sample. This situation is not described very conclusively by the picture of the anisotropy pulse, which is the convenient explanation for the precessional dynamics observed in the out-of-plane configuration. Nevertheless, it is considered important to know where to file the performed investigations in the context of applications of the all-optical pump-probe technique. Following this overview, the modeling of energy transfer processes in the sample is discussed, which is more suited to explain the magnetization dynamics in the ps range.

## 3.2. Two- and three temperature model

Since the pump pulses demagnetize the samples by thermal excitation, some time will be taken to elaborate on the transfer of thermal energy in the samples. At the start, a quick overview of this section is given. As already noted, the pump will transfer energy to the electrons. The electrons pass energy to the lattice via electron-phonon scattering.<sup>17</sup> In the most basic approach, these two subsystems can be considered as thermodynamical heat baths and temperatures are assigned to them, namely the *electron temperature*  $T_e$  and the *lattice temperature*  $T_l$ . To describe realistic scenarios one also has to include heat diffusion, which is performed

<sup>16</sup> At least no precession triggered by the anisotropy pulse, that is.

<sup>17</sup> Note that the electrons and the lattice (and later on, the spins) are treated as distinguishable systems. Every single system is assumed to be in equilibrium if not otherwise stated, for the physical quantity 'temperature' is only well-defined in this case.

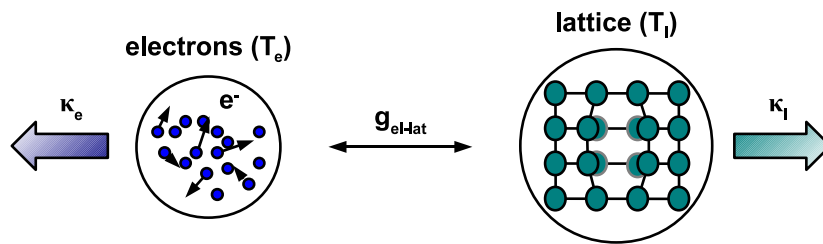


**Figure 3.5.:** Sketch of the two temperature model (2TM), visualizing the coupled baths for electrons and lattice and the heat diffusion from both.

by describing each system using a heat conduction equation. The resulting set of equations describing the two subsystems is the so-called *two temperature model* (2TM) [Hoh98, Mül07]. The 2TM is sketched in Fig. 3.5. It is suitable to model the absorption of the pump pulses. Yet it does not describe magnetization dynamics. For this, one must add the spin subsystem as a third heat bath and couple it to the other two. This yields the *three temperature model* (3TM) introduced by Beaurepaire et al. [BMDB96] to describe their measurements of sub-picosecond dynamics on nickel. Of course, the 3TM will also be used to describe the dynamics of the Heusler samples investigated in this thesis and the model is applied to determine the samples' degree of half-metallicity. To understand the applicability of the 3TM for doing so, the description of half-metals in the context of the 3TM is discussed. The role of the non-thermal electrons, which are sometimes included in the model, shall also be explained. It is later on proposed that it is these non-thermal electrons that play an important role in the dynamics of (almost) half-metallic Heusler compounds and therefore a corresponding expansion of the 3TM is proposed in chapter 3.3. These models will be used to describe the demagnetization curves of the samples.

As stated above, two temperatures  $T_e$  and  $T_l$  are introduced, assuming at first that the electrons and the lattice are individually in equilibrium for all times  $t$ . The two systems are coupled via the process of *electron-phonon scattering*. The *electron-phonon coupling constant*  $g_{el-lat}$  is a benchmark for the probability of such scattering events. Note that the electron may to a certain probability flip its spin while being scattered at a phonon. This will become important for half-metals. In the general case, the 2TM also includes diffusion for both the electrons and the lattice.

Now for the solution of the 2TM. First, its differential equations as given by

Hohlfeld [Hoh98] are presented. The full model reads as follows:

$$C_e \cdot \frac{\partial T_e}{\partial t} = \nabla(\kappa_e \nabla T_e) + g_{el-lat} \cdot (T_l - T_e) + P(\vec{r}, t) \quad (3.1)$$

$$C_l \cdot \frac{\partial T_l}{\partial t} = \nabla(\kappa_l \nabla T_l) + g_{el-lat} \cdot (T_e - T_l) \quad (3.2)$$

Here as well as in the following, the values  $C_i$  will denote *specific heats*, while the  $\kappa_i$  stand for *heat conductivities*.<sup>18</sup> The *source term*  $P(\vec{r}, t)$  is of special interest, for it contains the details of the optical excitation. Note that in this discussion the sample surface is assumed to lie in the xy-plane, and also normal incidence is given, i.e. the light pulse travels along the z-axis. For a sample of finite thickness  $d$  the source term is then given by

$$P(\vec{r}, t) = \frac{\alpha_{abs} \cdot F(\vec{r}, t) \cdot e^{-z/\lambda}}{\lambda \cdot (1 - e^{-d/\lambda})}. \quad (3.3)$$

The most important term in this formula is the established exponential factor in the numerator that was taken from the Lambert-Beer law. It includes the *optical penetration depth*  $\lambda$ , which is given by

$$\lambda = \frac{\lambda_0}{4\pi n_i},$$

where  $\lambda_0$  is the wavelength of the incident light (for the setup in use roughly 800 nm) and  $n_i$  is the imaginary part of the complex index of refraction of the sample [Hec05]. In this form,  $\lambda$  describes the decay of the amplitude.<sup>19</sup> The factor  $\alpha_{abs}$  in Eq. (3.3) is the *absorption coefficient* of the sample and is given by

$$\alpha_{abs} = 1 - R - T, \quad (3.4)$$

with  $R$  being the reflectivity of the sample and  $T$  its transmittivity.<sup>20</sup> Next is the function  $F(\vec{r}, t)$  that describes the fluence of the incident light as a function of space and time. The space dependency will basically be neglected in the discussion (i.e.  $F(\vec{r}, t) \equiv F(t)$ ) and it is assumed that  $F(t)$  is either a  $\delta$ -pulse,  $F(t) \sim \delta(t)$ ,

---

<sup>18</sup> The indices  $i = e, l, s$  stand for electrons, lattice, and spins, of course.

<sup>19</sup> Instead, some sources provide the penetration depth for the intensity, which corresponds to  $2\lambda$ .

<sup>20</sup> Frankly, this relation is not as easy to apply as it seems. This problem will be briefly addressed at the end of chapter 3.4

or of Gaussian type,  $F(t) \sim G(t)$ , where

$$G(t) = \sqrt{\frac{2}{\pi w}} \cdot e^{-\frac{2t^2}{w^2}}.$$

This turns out to be a good approximation, because the theoretical shape of the pulse is a hyperbolic secant [MFG84]. Finally, the factor in the denominator of Eq. (3.3) ensures the normalization demanded by energy conservation,  $\int_0^d P(\vec{r}, t) dz = \alpha_{abs} \cdot F(\vec{r}, t)$

A remarkably simple situation arises from Eq. (3.2) if on the one hand one neglects heat conduction ( $K_i = 0 \forall i$ ), assuming that the sample is homogeneously heated, and on the other hand the exact form of  $P(\vec{r}, t)$  is 'outsourced' from the system.<sup>21</sup> The latter is done by assuming the excitation is described by a  $\delta$ -like function (and thus finally can be expressed as an initial condition, i.e., as starting values for  $T_e$  and  $T_l$ ). The source term then takes on the form

$$P(t) = P_0 \cdot \delta(t), \quad P_0 = \frac{\alpha_{abs} F}{d}.$$

To a posteriori account for the form of the incident pulse, one can convolute the result with the source term [Dal08]. The simplified system reads

$$\begin{aligned} C_e \cdot \frac{\partial T_e}{\partial t} &= g_{el-lat} \cdot (T_l - T_e) \\ C_l \cdot \frac{\partial T_l}{\partial t} &= g_{el-lat} \cdot (T_e - T_l) \end{aligned} \tag{3.5}$$

and the dynamics is contained in only one variable  $\Delta T = T_e - T_l$  describing the dynamics of electrons and lattice. It can be solved analytically, as is shown in chapter A.1 in the appendix.<sup>22</sup> Neglecting the initial temperature  $T_0$  one can write the solution in the form

$$T_e(t) = T_1 + (T_{2,e} - T_1) e^{-t/\tau_E} \tag{3.6}$$

$$T_l(t) = T_1 \left(1 - e^{-t/\tau_E}\right), \tag{3.7}$$

where certain abbreviations have been introduced: The phenomenological *electron*

<sup>21</sup> The case of the 2TM with diffusion was discussed by Hohlfeld [Hoh98] and Müller [Mül07].

<sup>22</sup> The system is singular, thus the eigenvalue problem ansatz fails. However, the solution is simply obtained by inserting the equations into each other.

*relaxation time*

$$\tau_E = \left( g_{el-lat} \cdot \frac{C_e + C_l}{C_e C_l} \right)^{-1}$$

determines the time it takes for the sample to reach equilibrium after excitation. While in the context of the 2TM it is actually exact, i.e. identical to the electron-lattice relaxation time  $\tau_{el}$ , it is referred to as 'phenomenological', because after inclusion of the spin bath it no longer represents a fundamental material constant. The temperature  $T_1$  determines the new point of equilibrium; due to the fact diffusion has been neglected this equilibrium will exceed room temperature. In the context of the 2TM the temperature  $T_{2,e}$  represents the maximum temperature for the electrons. Both temperatures are of course determined by the fluence of the incident light, and also by several material constants. The exact dependencies are given by

$$T_1 = \frac{P_0}{C_e + C_l}, \quad T_{2,e} = \frac{P_0}{C_e} \quad (3.8)$$

as one would expect from its meanings. Next, one has to convolute the results with  $G(t)$  to achieve a more realistic description of the dynamics. The results for these functions, namely

$$[T_e * G](t) \quad \text{and} \quad [T_l * G](t),$$

are a bit lengthy and therefore only given as Eqs. (A.6) in chapter A.1 in the appendix.

Now the next step is taken by including the spin system, thus receiving the full 3TM. Diffusion is still neglected, as it is usually done when describing dynamics on the range of a few ps. The spin system is assigned a *spin temperature*  $T_s$ . It may be unintuitive at first to assign a temperature to the spins that is different from the electron temperature, because the concept of the spin describes an inherent property of the electron and thus one would assume  $T_s$  to be equal to  $T_e$  for all times. However, one has to keep in mind that the laser pulse transfers its energy only to the electrons, and it takes a finite time to pass the energy on to the spins. The spin system is coupled to both electrons and lattice, the corresponding coupling constants being  $g_{el-sp}$  and  $g_{lat-sp}$ . The equation for the spin system then reads

$$C_s \cdot \frac{dT_s}{dt} = g_{el-sp} \cdot (T_e - T_s) + g_{lat-sp} \cdot (T_l - T_s). \quad (3.9)$$

An important fact is that the coupling of the electrons to the spins, and thus  $g_{el-sp}$ , is mainly determined by spin-flip scattering processes of the *Elliot-Yafet* type [Mül07]. This will be discussed later on.

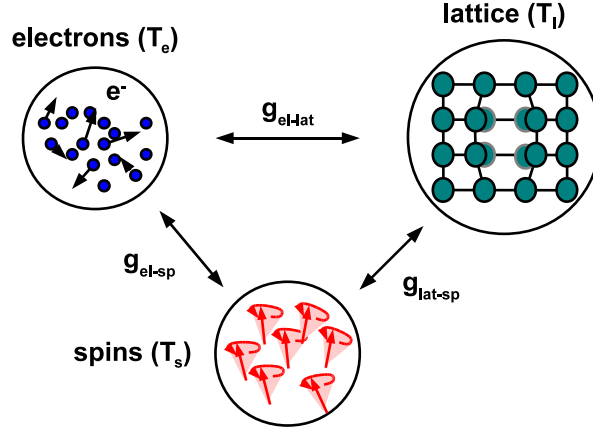


**Figure 3.6.:** Sketch of the three temperature model (3TM) neglecting diffusion. In comparison to Fig. 3.5, a new heat bath for the spins is introduced, which is in general coupled to both the electrons and the lattice.

The complete 3TM is sketched in Fig. 3.6. The equations for the complete system read

$$\begin{aligned}
 C_e \cdot \frac{\partial T_e}{\partial t} &= g_{el-lat} \cdot (T_l - T_e) + g_{el-sp} \cdot (T_s - T_e) \\
 C_l \cdot \frac{\partial T_l}{\partial t} &= g_{el-lat} \cdot (T_e - T_l) + g_{lat-sp} \cdot (T_s - T_l) \\
 C_s \cdot \frac{dT_s}{dt} &= g_{el-sp} \cdot (T_e - T_s) + g_{lat-sp} \cdot (T_l - T_s).
 \end{aligned} \tag{3.10}$$

For the solution of the 3TM the spin system is assumed to take on the role of a spectator, following the dynamics of electrons and lattice without giving any feedback. As can be seen later on, this assumption is justified by the fact that the specific heat  $C_s$  of the spin system is small compared to the specific heats of electrons and lattice, which is fulfilled for  $T_s \ll T_C$ . Therefore, one can simply use the solution of the 2TM (A.4) and plug it into the equation for the spin temperature.<sup>23</sup> This is equivalent to neglecting the terms coupling electrons and lattice to spins in Eqs. (3.10). Proceeding as discussed in the appendix (cf. chapter A.2), one arrives at

$$T_s(t) = T_1 + \frac{1}{\tau_E - \tau_M} \cdot \left[ (T_1 \tau_M - T_2 \tau_E) \cdot e^{-\frac{t}{\tau_M}} + (T_2 - T_1) \tau_E \cdot e^{-\frac{t}{\tau_E}} \right] \tag{3.11}$$

The new timescale  $\tau_M$  is called the (phenomenological) *demagnetization time* and

<sup>23</sup> Actually, the assumption of a negligible  $C_s$  should not be taken lightly, as is discussed in chapter 3.4.

is given by

$$\tau_M = \left( \frac{1}{\tau_{es}} + \frac{1}{\tau_{ls}} \right)^{-1} = \left( \frac{g_{el-sp} + g_{lat-sp}}{C_s} \right)^{-1}. \quad (3.12)$$

In this notation it is evident that the demagnetization time is composed of two contributions,  $\tau_{es}$  and  $\tau_{ls}$ , which are based on the energy transfer from electrons to spins and from lattice to spins, respectively. Note also that a new constant  $T_2$  ( $\neq T_{2,e}$ ) appears, which is defined as

$$T_2 = \frac{P_0 \cdot g_{lat-sp}}{C_e(g_{el-sp} + g_{lat-sp})}.$$

Again, the solution

$$[T_s * G](t)$$

for the convolution with the Gaussian pulse is given in the appendix (Eq. (A.12) in chapter A.2). Note that this is the function that can be fitted to the dynamic magnetization signal obtained from the measurements. Equation (3.11) describes a characteristic double-exponential behavior of the spin temperature  $T_s$ , as is observed in generic measurements.

### 3.3. Determining the polarization $P$ and expanding the 3TM

In this section, the possibility to extract a value for the spin polarization  $P$  (as defined in Eq. (2.9)) from measured magnetization dynamics is discussed. Müller et al. established a method to determine  $P$  via the demagnetization time  $\tau_M$  of the 3TM [MWD<sup>+</sup>09]. It is imperative for the discussion to understand the correlation of  $\tau_M$  and  $P$ , especially with regard to the differences in dynamics between materials of different  $P$ . Concerning the latter, the promised expansion of the 3TM shall be presented.

The result of Müller et al. is reproduced in Fig. 3.7 and shall be discussed in the following. The demagnetization time  $\tau_M$  is found to be roughly inversely proportional to  $(1 - P)$ . The authors state that a material is half-metallic if its polarization  $P$  is higher than 80%, indicated by the vertical gray line. Also, for a fully polarized material, the demagnetization  $\tau_M$  takes on a value of about 4 ps, as indicated by the horizontal gray line. The crucial part of the determination of  $P$  is to link the experimentally observed demagnetization time  $\tau_M$  to the fundamental microscopic processes contributing to it. Taking a look back at the schematic for

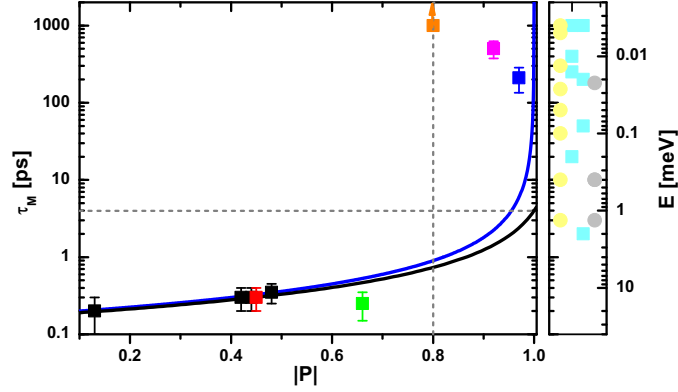


**Figure 3.7.:** Dependence of  $\tau_M$  on  $P$  as stated by Müller et al. [MWD<sup>+</sup>09]. As discussed in the text, the demagnetization time  $\tau_M$  is roughly inversely proportional to  $(1 - P)$ . A material is said to be half-metallic, if its polarization  $P$  is higher than 80%, as indicated by the vertical line. For a value of  $\tau_M$  higher than 4 ps (horizontal line), the Elliot-Yafet scattering is completely blocked. Details on the figure are given in the reference.

the 3TM in Fig. 3.6, the reader should remember that the spin temperature  $T_s$ , and therefore the magnetization dynamics, is influenced by the interaction with the electrons and the lattice. In the solution of the 3TM the fact emerged that one can link the mentioned interactions to two distinct timescales  $\tau_{es}$  and  $\tau_{ls}$ . What are their microscopic origins? It has already been mentioned that the electron-spin interaction is governed by Elliot-Yafet spin-flip scattering. An approach based on Fermi's golden rule yields the following formula for the electron-spin relaxation time  $\tau_{es}$  [MWD<sup>+</sup>09]:

$$\tau_{es} = \frac{\tau_{el,0}}{c^2} \cdot \frac{1}{1 - P} \quad (3.13)$$

In this equation,  $\tau_{el,0}$  is the *electron momentum scattering rate*, which represents the scattering rate for a non-magnetic material, and  $c$  is the parameter introduced by Elliot [Ell54] to describe the admixture of the spin variables at the Fermi level. It holds that

$$c \sim \frac{\zeta_{SO}}{\Delta E_{exch}}, \quad (3.14)$$

where  $\zeta_{SO}$  is the strength of the spin-orbit interaction and  $\Delta E_{exch}$  is the energy splitting at a band crossing.

It was also already noted that the lattice-spin relaxation time  $\tau_{ls}$  is related to anisotropy fluctuations. The mechanism was discussed in detail by Hübner

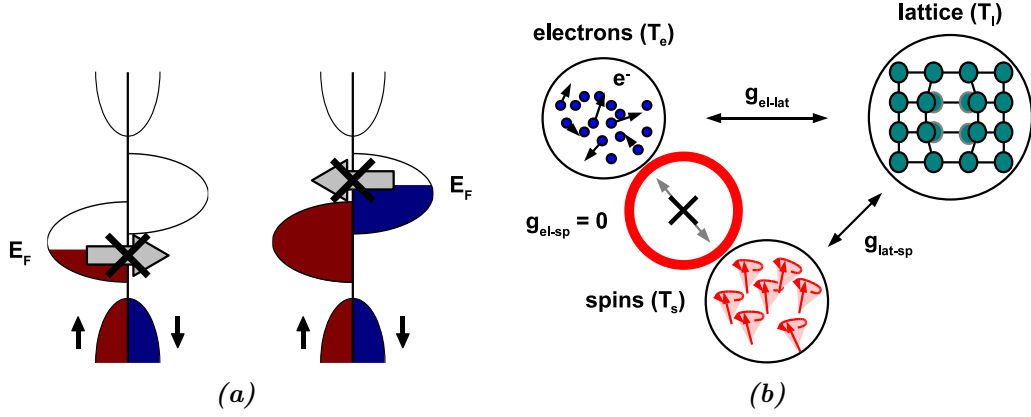


**Figure 3.8.:** DOS and sketch of 3TM for an ideal half-metal: An ideal half-metal does not possess target states for spin-flip scattering at the Fermi level in its density of states (a). Therefore, the direct scattering channel between electrons and spins is blocked in the 3TM (b) and energy can only be transferred from the electrons to the spins via a detour over the lattice.

[HB96], who established a relation stating

$$\tau_{ls} = \frac{1}{A_{\theta_D}(T)|E_{\text{aniso}}|^2}. \quad (3.15)$$

$A_{\theta_D}$  is a function describing the temperature dependence of  $\tau_{ls}$ ,  $E_{\text{aniso}}$  is the anisotropy energy. In general, both scattering channels contribute to the demagnetization time  $\tau_M$ , and therefore the two timescales have to be inversely added (cf. Eq. (A.10)), resulting in

$$\tau_M = \frac{\tau_{es}\tau_{ls}}{\tau_{es} + \tau_{ls}}. \quad (3.16)$$

Next, the focus is directed to the case of the half-metal. The observant reader will already have a hint on the specialty of the description of half-metals in the 3TM. According to Eq. (3.13),  $\tau_{es}$  diverges for  $P \rightarrow 1$ , which corresponds to an ever smaller probability for spin-flip scattering of electrons. This behavior is easily illustrated by means of the density of states for a half-metal. As stated above in chapter 2.3, a half-metal is characterized by having no electronic states at the Fermi level for one type of spin. However, it has just been stated that the coupling between the electrons and the lattice is mediated by the Elliot-Yafet mechanism, which is a spin-flip process. Since the electrons that take part in the dynamics stem from the vicinity of the Fermi edge, it is concluded that the Elliot-Yafet scattering mechanism is blocked in an ideal half-metal. The simple reason is, that the density of states does not provide any target states for the scattering electrons, as illustrated in Fig. 3.8(a). This will of course have a dramatic impact

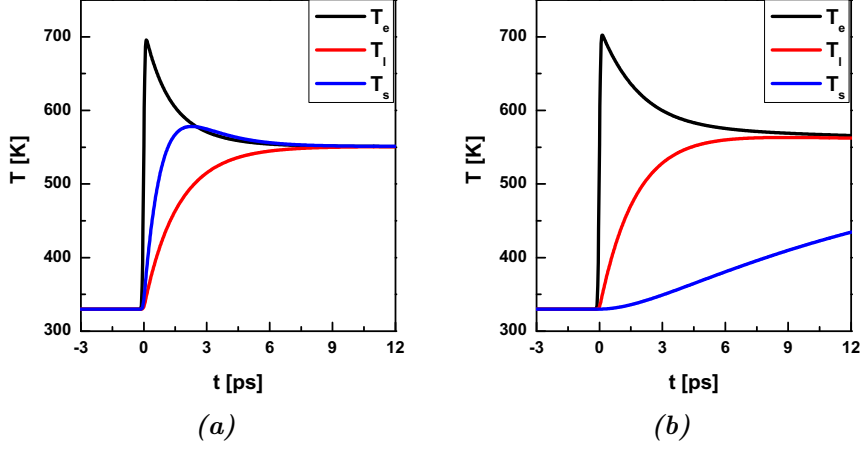


**Figure 3.9.:** Numerical solution of the 3TM for samples of (a) low and (b) high polarization  $P$ . The difference in polarization is modeled by a difference in the electron-spin coupling constant  $g_{el-sp}$ . This results in a completely different behavior of the spin temperature, and thus, the magnetization. The increase in electron temperature as the pulse arrives and the following equilibration with the lattice are almost identical in both cases, because the spin specific heat  $C_s$  is assumed to be very low. All parameters other than  $g_{el-sp}$  have been taken from Beaurepaire [BMDB96].

on the 3TM. If the scattering channel between electrons and spins is blocked, the electrons excited in the pump-probe experiment can transfer their energy only by taking the indirect route via energy transfer to the lattice and from the lattice to the spins, as depicted in Fig. 3.8(b). One will have to regard this by setting the electron-spin coupling constant  $g_{el-sp}$  to (almost) zero. As a conclusion, the spin temperature  $T_s$  is expected to no longer primarily follow the electron temperature  $T_e$ . Instead, it will have a shape similar to that of the lattice temperature  $T_l$ , but with a greatly enlarged characteristic timescale, due to the fact that the demagnetization is mediated by the lattice and thus includes the product of  $g_{el-lat}$  and  $g_{lat-sp}$ . The latter one, associated to  $\tau_{ls}$ , is assumed to be small, because energy transfer from lattice to spins is only provided by anisotropy fluctuations [HB96]. Figure 3.9 shows numerical solutions of the 3TM for the cases of low and high polarization  $P$ . For both cases, the electron and lattice temperatures  $T_e$  and  $T_s$  obey the exponential behavior predicted by the 2TM in Eq. (3.7). In contrast, the spin temperature  $T_s$  shows a clearly different behavior for the two cases: For a low value of  $P$ ,  $T_s$  equilibrates with  $T_e$  during the first three ps, while for high  $P$  it rises extremely slow, reaching the new equilibrium temperature after several hundred ps. The latter scenario is indeed observed in the experiment for good half-

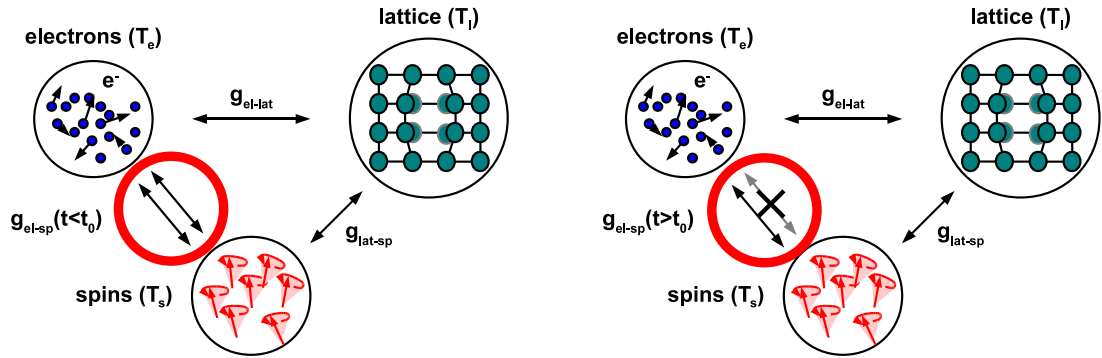


**Figure 3.10.:** Sketch of the expanded three temperature model (X3TM). In contrast to Fig. 3.8, the channel between electrons and spin is not assumed to be completely blocked, but time dependent. For times  $t < t_0$  (left), there are two channels for the coupling available, so the coupling is stronger than for times  $t > t_0$  (right).

metals (where 'good' means 'high  $P$ '), e.g. for  $\text{CrO}_2$  (cf. Fig. 4.24(b)). However, half-metallic samples show a small step-like change in the magnetization directly after the excitation. The fact that such a feature is also observed for materials of low polarization will play an important role in the course of this thesis, starting with the expansion of the 3TM in the next paragraphs and ultimately leading to a complete picture of the spectrum of demagnetization curves for different polarizations in chapter 4.6.

Now the mentioned expansion of the model is discussed, which aims to include the effect of a finite polarization  $P$  smaller than 100% into the 3TM. The reader should remember the description of the excitation performed by the laser pulses in the pump-probe experiment. It has been said that a portion of the electrons in the sample are transformed into non-thermal electrons. In the experiment, one excites the electrons with photons of an energy  $h\nu \approx 1.5 \text{ eV}$ , which is more than the typical width of the spin gap  $\Delta_{\uparrow\downarrow}$  for Heusler compounds.<sup>24</sup> Also, the spin-flip energy  $\Delta_{sf}$  (cf. Fig. 2.3) is by definition always smaller than the spin gap, and thus even further below 1.5 eV. From this one can deduce that a great portion of the non-thermal electrons is in fact raised to energies above the spin gap and therefore very well able to take part in spin-flip processes. On the other hand, it has been noted that the life time of these non-thermal electrons is very short, between 5 and 20 fs, depending on the energy above the Fermi level. This leads to the proposal of the following *expansion of the three temperature model* (X3TM), illustrated in Fig. 3.10: The energy transfer from electrons to spins is possible not only via one, but via two channels. The first channel, identified with a timescale

<sup>24</sup> For  $\text{Co}_2\text{MnSi}$ , for example, the spin gap is about 0.4 meV [SHO<sup>+</sup>07].

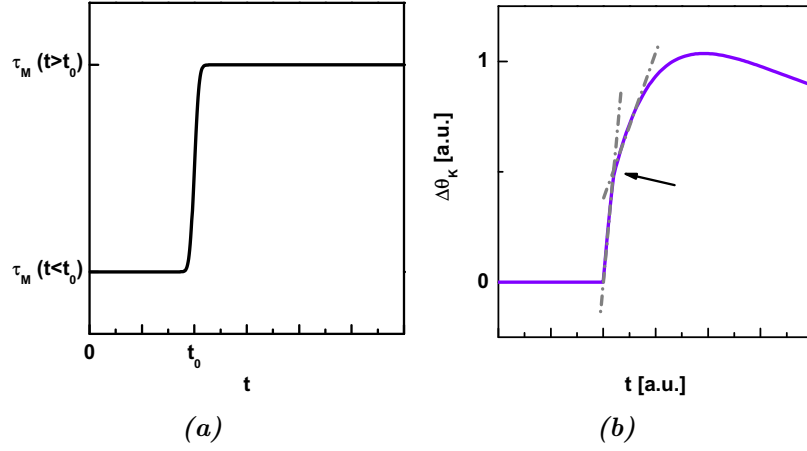


**Figure 3.11.:** Dynamics according to the X3TM: (a) timely evolution of the demagnetization time  $\tau_M$ , (b) numerical solution of the X3TM showing a step-like feature. The gray lines are guides to the eye and cross at a time of approximately  $t_0$ .

$\tau_{es,1}$ , is a temporary one, provided by non-thermal electrons with energies above the spin gap. It is therefore independent of the spin polarization  $P$  of the material, but sensitive to the value of the spin-flip energy  $\Delta_{sf}$ . Also, the channel will only open up for a short period following the excitation. After a time  $t_0$  which can be estimated by the thermalization time of the hot electrons, it will no longer be available. The second channel, connected to a timescale  $\tau_{es,2}$ , is the known channel provided by Elliot-Yafet type spin-flip processes. It is a permanent channel which is sensitive to the spin polarization  $P$  of the material.

This behavior is reflected in the electron-spin contribution  $\tau_{es}$  to the demagnetization time  $\tau_M$ , which now becomes time-dependent by itself. For  $t < t_0$ , the energy transfer from the electrons to the spin system will be higher, and therefore

$$\tau_{es}(t < t_0) = \left( \tau_{es,1}^{-1} + \tau_{es,2}^{-1} \right)^{-1} \quad (3.17)$$

and also  $\tau_M$  will be smaller. For times  $t > t_0$ , the first channel from electrons to spins is blocked, resulting in an enlarged  $\tau_{es}(t > t_0) = \tau_{es,2}$ . If the time-dependent  $\tau_M$  is inserted into the differential equation for the spin temperature given in Eq. (3.9) and the equation is solved numerically (still using the analytical results from the 2TM for  $T_e$  and  $T_l$ ), one observe the advent of a new feature for a certain range of parameters, shown in Fig. 3.11: The demagnetization observed now shows a 'step-like' feature, where the loss of magnetization is steeper for small times (up to about  $t = t_0$ ), and more gradual later on. Such a feature is very prominent in the data for  $\text{CrO}_2$  and LSMO (cf. Fig. 4.24). It is also observable for certain

Heusler compounds, as it will be shown in the analysis of the measured data in chapter 4.1. Note that both cases can be explained using the expanded model. In chapter 4.6, the validity and reach of the proposed expansion of the three temperature model will be discussed.

### 3.4. Comments on the specific heat

Some time is taken to have a closer look on the role of the specific heat  $C = C_e + C_l + C_s$  for the discussion of the 3TM. The analytical solution of Eqs. (3.5) and later on Eq. (3.9) assumes  $C_i$  to be constant. This, however, is not true in real systems. The lattice contribution  $C_l$  is probably the least problematic part. It can be estimated according to the Debye model and spawns an approximately constant value at room temperature  $T_R$ . Even if  $\theta_D > T_R$ , variations of  $C_l$  do not exceed a few percent. The specific heat  $C_e$  of the electrons, however, is already clearly temperature dependent. A good approximation is a linear relation between  $C_e$  and  $T$ , which is written in the form

$$C_e(T) = \gamma \cdot T. \quad (3.18)$$

This fact is known for low temperatures; it holds for higher temperatures, too, but the coefficient  $\gamma$  may be different [BMDB96].

The spin contribution  $C_s$  is a more complex issue, especially if one approaches  $T_C$ . While in the context of the 3TM  $C_s$  has been considered to be small (in comparison to  $C_e$  and  $C_l$ , that is), this is only valid for temperatures clearly below  $T_C$ . From thermodynamics it is known that since at  $T_C$  the ferromagnetic sample undergoes a second order phase transition, the specific heat will diverge when approaching  $T_C$ . Orehotsky and Schröder investigated the phase transition and performed series expansion calculations on the Heisenberg and Ising model. They succeeded in modeling experimental data on specific heat for various NiFe and NiCo alloys with a logarithmical relationship between  $C_s$  and  $T$ , namely

$$C_s \sim \ln \left\{ \left| \frac{T}{T_C} - 1 \right|^A \right\}. \quad (3.19)$$

While this law technically only holds for  $T > T_C$ , it may to a certain point also be applied for the range  $T < T_C$ , but with a different critical exponent  $A$ . In the latter case,  $A$  is typically below, but close to, a value of one; only for pure nickel it is about 0.2. Nevertheless, the specific heat will not diverge in real

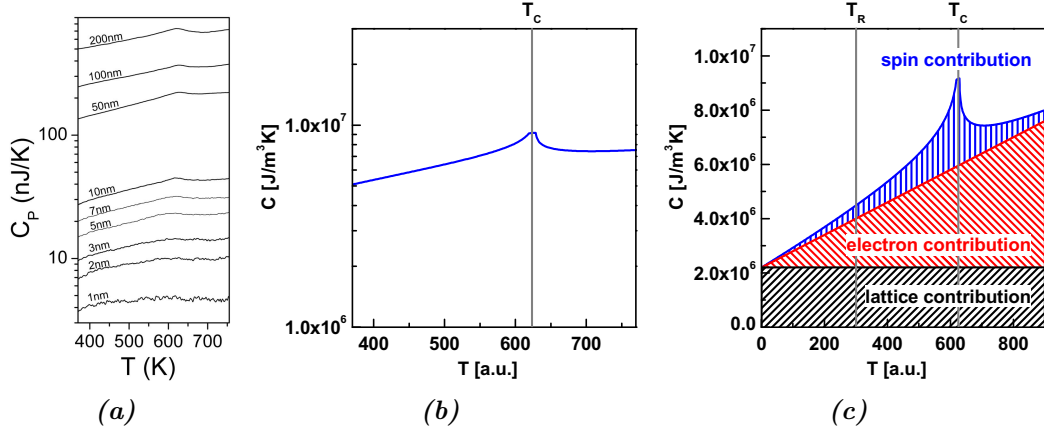


**Figure 3.12.:** Realistic model of specific heat for Ni: (a) nanocalorimetric measurements on Ni films by Lopeandia et al. (taken from [LPRV08]), (b) model of specific heat  $C$  for a 20 nm Ni film used for 3TM simulations, (c) different contributions to the modeled specific heat. The splitting of  $C$  reveals that near  $T_C$  the spin contribution is of the same order as the electron and lattice contributions. Note the logarithmic scales for (a) and (b).

samples, but it will rather show a rounded peak around  $T_C$ . Maszkiewicz et al. [MMW79] investigated the dependence of the peak on the sample purity for the case of nickel. They found that, although the peak width is dependent on the sample purity, it remains even for samples of highest purity and can therefore be seen as an intrinsic property of the phase transition at  $T_C$ . They also managed to predict the occurrence of the peak using a fluctuation model. Since there is no equivalent study on Heusler samples available, the shape and the amplitude of the peak at  $T_C$  are not known and thus their exact impact on the specific heat cannot be predicted. However, it can be assumed that the magnitude of the spin contribution is of the same order of magnitude as for nickel. This seems reasonable, since the measurements quoted by Orehotsky and Schröder show that altering the sample composition it is mainly the shape of the peak that changes, while the height of the peak never encounters a change by more than a factor of two. The use of the analogous treatment is bolstered by the fact that the nickel samples of Orehotsky and Schröder are alloyed with iron and cobalt, which are both elements used in many of the Heusler compounds in this sample.<sup>25</sup>

In the context of this thesis, a numerical solution of the 3TM for a nickel film using a realistic model of the specific heat is presented, where both the elec-

<sup>25</sup> In fact, all samples contain cobalt, while most of the others contain iron, or manganese, its predecessor in the PTE.

tron contribution  $C_e$  and the spin contribution  $C_s$  are temperature-dependent.<sup>26</sup> Thereby one can demonstrate the influence of regarding  $C_s$  in the specific heat  $C$  on the dynamics at all. The study that will be referred to in order to model the behavior of  $C_s$  is a recent nanocalorimetric investigation on nickel films by Lopeandia et al. [LPRV08], that is reproduced in Fig. 3.12(a). The study is giving detailed  $C_s(T)$  curves for thin films of various thicknesses. Rounding of the specific heat at  $T_C$  can also be observed for the samples. It is strongest for very thin films ( $d < 10$  nm), a fact the authors attribute to the decreasing magnetic interaction length caused by the formation of smaller grains in the polycrystalline samples of lesser thickness. The Heusler samples investigated in this thesis are in general of high compositional purity and well ordered, so there should be no small grains. Therefore, a rather sharp peak that is well described by a logarithmic function according to (3.19), should occur in their specific heat, too. As to the estimation of the actual maximum value of  $C_s$  (occurring at  $T_C$ , of course), the following observations are made based on the data from Lopeandia et al. and the values provided for the three temperature model by Beaurepaire [BMDB96]: At room temperature, the values for  $C_e$  and  $C_l$  are almost exactly the same, whereas  $C_s$  is small (about 10% of  $C_e$ ) and can be neglected. At a temperature of  $T_C$ , the lattice contribution is still the same according to the Debye model, but the electron contribution is roughly twice the one for room temperature. However, the total value  $C$  for the specific heat itself is at  $T_C$  twice as high as the value for room temperature. Therefore, the contribution  $C_s$  of the spin system must have reached a value of approximately the same magnitude as the lattice contribution  $C_l$ . From this, parameters can be deduced for a realistic model of the temperature dependent specific heat  $C(T)$  and its consequences for the solutions of the 3TM can be investigated.

The specific heat following from these considerations is shown in Fig. 3.12(b). In a very small range around  $T_C$ , the logarithmic contribution has been cut off and replaced by the maximum value. Obviously, the model matches the measurements extremely well, though Lopeandia et al. did not perform a measurement on a film of the assumed thickness of  $d = 20$  nm. Note also the decomposition of the specific heat into its three contributions  $C_e$ ,  $C_l$ , and  $C_s$  in Fig. 3.12(c). There, the difference in the relations of the contributions between the values at room temperature  $T_R$  and at Curie temperature  $T_C$  is of interest. As mentioned above, the contribution from the spins is negligible at  $T_R$ , but at  $T_C$  it is of the same order of magnitude as the electron and lattice contributions and can thus no longer be

---

<sup>26</sup> Unfortunately, there is no longer an analytical solution of the 3TM including the temperature-dependent values of  $C_e$  and  $C_s$ .

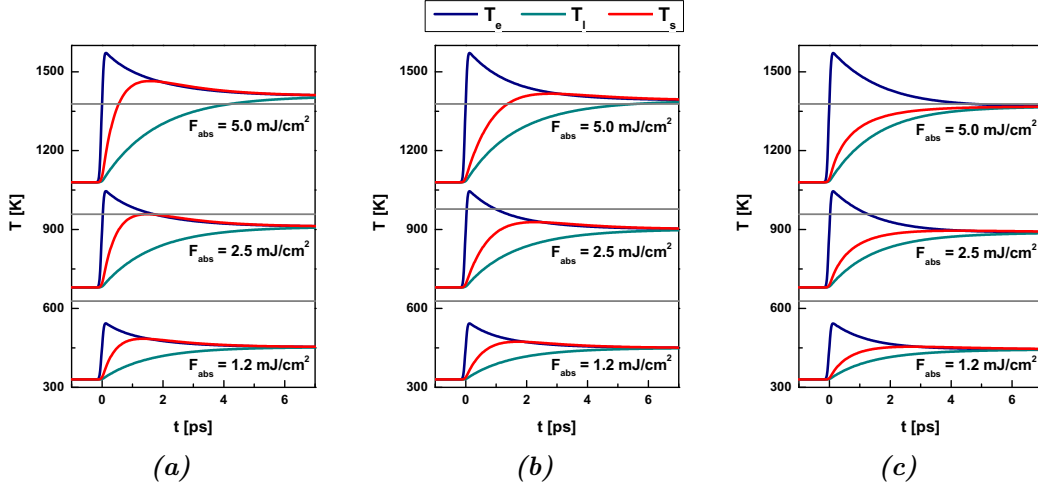


**Figure 3.13.:** Numerical solutions of the 3TM for different pump fluences with varied assumptions for the spin specific heat  $C_s$ : (a) constant  $C_s$ , (b) linear temperature dependence ( $C_s \sim T_s$ ), (c)  $C_s$  modeled according to Lopeandia et al. [LPRV08]. Curves are shifted for clarification. The gray lines mark the bulk Curie temperature  $T_C = 628$  K for nickel. All other parameters are taken from Beaurepaire [BMDB96].

neglected when nearing  $T_C$ .

The model of the specific heat from Fig. 3.12(b) is now compared to the simple assumption of a constant specific heat  $C$  and a model with constant  $C_s$ , but linear temperature dependence of  $C_e$ . All three models are applied in numerical solutions of the 3TM (see Eqs. (3.10)). The results are shown in Fig. 3.13, where for each model calculations are performed for three different values of absorbed fluence  $F_{abs}$ . The three curves have been shifted, and in addition the Curie temperature  $T_C = 628$  K (for nickel) was inserted for each curve. For the case (a) of constant specific heat the form of the curves is of course independent from the absorbed fluence. For the assumption of a linear electronic contribution  $C_e$  (b), the maximum value of  $T_s$  is smaller, and the maximum is slightly retarded. The overall form of the curve is still the same, but for higher values of  $F_{abs}$  the new equilibrium temperature is already slightly lower, because for temperatures above  $T_R$  the total specific heat  $C$  is greater than in case (a). These trends are even stronger in case (c), where the model from Fig. 3.12(b) is used. The maximum of the spin temperature  $T_s$  is now barely visible. The demagnetization time is clearly enlarged, as is indicated by the dependence of  $\tau_M$  on  $C_s$  (cf. Eq. (3.12)). Also, the new equilibrium temperature does not rise above  $T_C$  for the highest value of  $F_{abs}$ , in contrast to the two other models.

The simulations performed demonstrate a clear difference in the behavior of

the spin temperature  $T_s$  depending on the model for the specific heat. However, for the simulations all other parameters, in particular the coupling constants  $g_{i-j}$ , have been kept constant. Adjusting them can very well restore the form of the spin temperature, even for the case (c) of the specific heat modeled according to the measurements of Lopeandia. This in turn means that the estimation of these constants by Beaurepaire [BMDB96] is not useful for the determination of their real values. Also, the values of demagnetization determined from the hysteresis (cf. Fig. 3.2) seldom reaches values above 20%, suggesting that the spin temperature is still considerably below  $T_C$ . Additionally, it means that the absorbed fluence is very low, about 1/30 of the incident fluence  $F$ . Unfortunately, it is not possible to double-check this value by determining the value of  $\alpha_{abs}$  (see Eq. 3.4) via measuring the reflectivity  $R$  and transmission  $T$ . While the reflectivity  $R$  in general takes on values of about 50%, the transmission is almost impossible to determine for the samples in use. For the samples on Si the substrates (and in some cases, the underlayers of the Heusler films, too), are not transparent, while for samples on MgO the transmitted light is strongly scattered due to the rough backside of the substrate. The only estimation possible is that  $\alpha_{abs}$  is lower than 25%, which is still an order of magnitude above the values suggested by the simulations and the degree of demagnetization. Nevertheless, the simulations performed provide insight into the importance of the modeling of the specific heat.

### 3.5. TRMOKE setup

To conclude the discussion of the experimental techniques the setup used for the all-optical pump-probe experiments is presented and details on the various investigated Heusler compounds are given. The setup was described extensively in various other theses [Djo06, Mül07, Wal07, Len08], so the description will be restricted to a short overview.

The setup consists of a self-built *titanium sapphire laser* (Ti:Sa), which is pumped by a commercial *Verdi V18 solid state laser* (Verdi) from Coherent Inc. and amplified with a *regenerative amplifier* (RegA 9050) also manufactured by Coherent. Figure 3.14(a) shows a schematic overview of the laser system. The continuous pump beam of 16.5 W at a wavelength of 532 nm is split up between the Ti:Sa and the RegA with the bigger portion going to the RegA. In the Ti:Sa, the pump beam is coupled to a resonator containing the Ti:Sa crystal ( $\text{Ti:Al}_2\text{O}_3$ ), where it is reflected back and forth to increase pump efficiency. The pumped Ti:Sa crystal provides a very broad gain spectrum of about 200 nm width at wavelengths

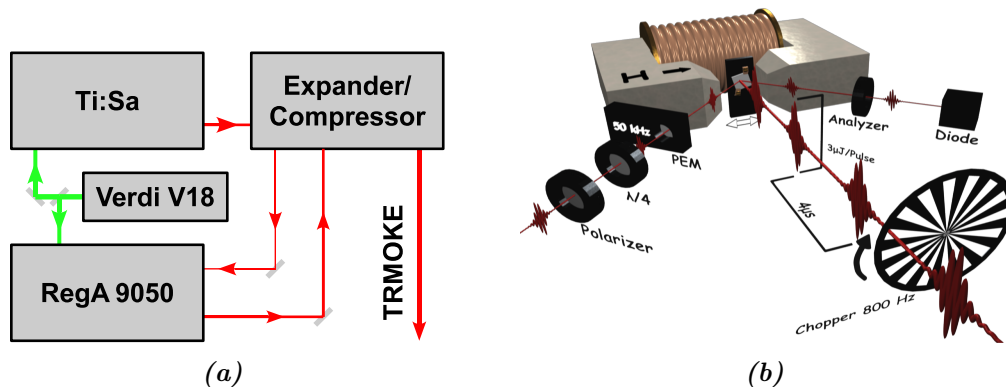


**Figure 3.14.:** Overview of the TRMOKE setup in use: (a) schematic of the laser system, (b) key components of the double-modulated TRMOKE setup (rendered by J. Walowski). In (b), the sample holder between the poles of the magnet is visible at the center. The sample is hit by the pump and by the probe, and the reflected probe beam is steered into the diode for measurement.

around 790 nm. From this the folded oscillator used to produce the ultrashort laser pulses via mode-coupling selects a spectral range of roughly 30 nm width (FWHM) around 815 nm. Mode-coupling is achieved by operating the laser in the unstable continuous regime and disturbing the oscillator (i.e., tapping one of the end mirrors). Operation of the Ti:Sa in the mode-coupling state is facilitated by self-focusing in the crystal on the one hand and by compensation of dispersion in the oscillator on the other hand. The latter is achieved by inserting two prisms in the beam path. Both mechanisms are needed to maintain the fixed phase relation for the wave package shaping the ultrashort laser pulse.

The pulses produced have a timely width  $w$  of about 60 fs and are emitted from the Ti:Sa with a repetition rate of  $f = 80$  MHz. Since the laser has an output power of roughly 500 mW, the energy per pulse is about 6 nJ. The timely shape of the pulses is a hyperbolic secant [MFG84], but for all practical purposes one can assume it to be of Gaussian form. The spectrum of the Ti:Sa can be monitored using a spectrometer. This is in particular necessary to ensure that there is no cw contribution to the spectrum. It is also assumed that the cross section of the pulses is Gaussian, which is important to calculate the fluence of the beam (cf. chapter B.1). The Ti:Sa pulses are chirped in the expander before being amplified in the RegA. This is necessary to reduce the peak intensity of the pulses, averting damage from the RegA crystal. The RegA itself basically just works like a q-switched, second oscillator with additional components to couple in single pulses, amplify them, and finally extract them. Coupling in and extracting the pulses needs to be done with accurate phase relations to the pulse, which is steered by

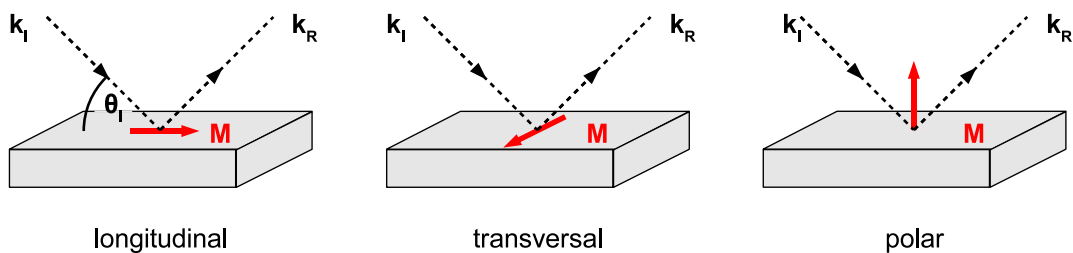


**Figure 3.15.:** Different geometries for MOKE measurements. For the setup in use, the longitudinal configuration was adapted.

electronics. The extracted pulses are sent through the compressor to restore the original pulse shape. The beam now has a power of approximately 800 mW and a repetition rate of 250 kHz, resulting in an energy of about  $3 \mu\text{J}$  per pulse. The pulses are p-polarized, i.e. the vector  $\vec{E}$  of the light lies in the plane of incidence. Before being sent to the experiment, the power is adjusted using a  $\lambda/2$  plate and a polarizer. The temporal width can be monitored via an autocorrelator using a  $\beta$ -barium borate (BBO) crystal.

Next is the description of the actual TRMOKE measurements. In general, there are three main geometries to perform MOKE measurements, that are illustrated in Fig. 3.15. For the setup in use, the longitudinal configuration was adapted. Also, the angle of incidence  $\theta_I$  is noted. In general, the strength of the linear MOKE signal decreases with increasing  $\theta_I$ , while the QMOKE is strongest for normal incidence. In the setup used,  $\theta_I$  is roughly  $30^\circ$ , enabling measurements of both linear and quadratic MOKE signals.

For the evaluation of the TRMOKE signal the *double modulation technique* is used. Since there are various descriptions of this technique available in literature, this thesis will not elaborate on it. In fact, it is only applied to easily access the Kerr rotation of the sample and to improve the signal to noise ratio of the measurement. A mathematically rigorous description was given by Koopmans [Koo03]. An illustration of the key components of the TRMOKE setup is provided by Fig. 3.14(b). The incoming laser beam is split into pump and probe, where in this case the pump carries over 90% of the incident energy. The pump is modulated by a mechanical chopper at a frequency of 800 Hz<sup>27</sup> and focused to a diameter of about  $60 \mu\text{m}$  on the sample. The probe is first sent through a quarter-wave plate to adjust its incident polarization, and then passes a *photoelastic modulator* (PEM) operated at 50 kHz. It is focused to a diameter of about  $30 \mu\text{m}$  on the sample.

<sup>27</sup> Modulation of pump and probe are only necessary for the double modulation scheme and therefore not discussed any further in this context.

The sample itself is mounted between the poles of a water-cooled electromagnet capable of applying an in-plane field of 150 mT. The sample mount can be adjusted vertically using a micrometer screw and shifted horizontally by a stepper motor. The reflected probe passes an analyzer and then enters the photodiode used in the actual measurement. Note that in order to create the temporal delay of the probe required for time-resolved measurements, a retroreflector on a mechanical delay stage is installed in the beam path of the probe (not shown in Fig. 3.14(b)). It allows for a range of the *delay time*  $\Delta\tau$  of about 1 ns with a typical minimum step width of 20 fs. The signals of the photodiode are processed using digital *lock-in amplifiers* from Stanford Research Systems (type SR 830 DSP). The beam diameters of pump and probe can be checked observing the power of the reflected pump beam while moving the sample so that the pump passes a straight sample edge. Since the beam profile is Gaussian, the reflected power describes an error function as a function of the sample position when the beam is clipped off by the edge of the sample. This function can be fitted to obtain the width of the pump.

The working setup extracts the change  $\Delta\theta_K$  of the Kerr rotation. Since  $\Delta\theta_K$  is rather small, it is assumed to be proportional to the change  $\Delta M$  of the magnetization (cf. Fig. 3.2), which in turn is assumed to be proportional to the change of spin temperature  $\Delta T_s$ . Therefore, the measured TRMOKE signal can be compared to the solution of the 3TM (cf. e.g. Fig. 3.9). Of course, if the changes in temperature and magnetization become high, especially when nearing the Curie temperature  $T_C$ , the simplifying assumptions made can easily become too coarse and have to be reevaluated. In the course of this thesis, however, values of the (relative) demagnetization are of the order of 10% and the linearizations are of sufficient accuracy for the evaluation.

The TRMOKE setup can be slightly modified to measure the reflectivity of the sample. This is done using the method of balanced photodiodes described by Koopmans [Koo03]. The required reference beam is split from the probe before passing the quarter-wave plate. The reflectivity is of interest, because it resembles the electron and lattice dynamics according to the 2TM. The result for the electron and lattice temperatures  $T_e$  and  $T_l$  from the 2TM is also included in the analytical solution of the 3TM (Fig. 3.9). A discussion of the physics involved in reflectivity measurements has been performed by Djorjđević et al. [DLM<sup>+</sup>06]. The important fact is that the reflectivity of the sample changes by an amount  $\Delta R$  because of two mechanisms invoked by the laser excitation. First, the excitation of the electrons leads to an altered occupation of the density of states, which affects the optical response of the system. This contribution can increase or decrease the reflectivity, depending on the details of the density of states. The second mechanism involves

the rise of the lattice temperature  $T_l$  triggered by the energy transfer from the electrons. Since the lattice excitation displaces the lattice atoms, it shifts the energy bands of the lattice. This results in a change of both initial and final states for excitation of the electrons and thus spawns a second contribution to the reflectivity change. Both the electron-induced change  $\Delta R_e$  and the lattice-induced change  $\Delta R_l$  overlap. Since their absolute values are small, they are proportional to the temperatures  $T_e$  and  $T_l$ , respectively. Djorjdević et al. therefore propose the following equation for the change of the reflectivity of the excited sample:

$$\Delta R = \Delta R_e + \Delta R_l = a\Delta T_e + b\Delta T_l \quad (3.20)$$

The constants  $a$  and  $b$  are material-dependent. Since according to the 2TM (cf. Eq. A.1) both  $T_e$  and  $T_l$  are governed by the relaxation time  $\tau_E$ , it seems possible to extract this parameter from the reflectivity measurements. However, it is important to remember that the constant  $a$  and/or  $b$  may be negative, which affects the shape of the reflectivity signal. Additionally, the excitation profile in the film is different depending on the ration of the film thickness  $d$  and the optical penetration depth  $\lambda$ . While the discussion here will not go into detail here (see [DLM<sup>+</sup>06] for further reading), this causes a qualitative difference in the measured reflectivity signal. The analysis of the reflectivity is therefore often quite intriguing, and an evaluation of the reflectivity signal with the aim of determining  $\tau_E$  is not always possible. This issue will be addressed in the evaluation of the experimental data in chapter 4.

A concluding remark: The setup used is highly complex and adjustment can be very tedious once one is outside a small window of working parameters. Stable operation is only made possible by using the setup in strictly controlled environmental conditions, with stability of temperature being the most critical point. However, the working setup provides an excellent tool for pump-probe experiments, combining powerful laser pulses with a very high repetition rate. This is vital to the measurements performed, ensuring results of high quality, especially concerning the signal to noise ratio.

## 3.6. Sample descriptions

It is now time for the description of the Heusler samples on which measurements are performed. For every material a short overview including the layer stacking of the samples is given. For samples of the compounds  $\text{Co}_2\text{MnSi}$  and  $\text{Co}_2\text{FeAl}$  there is also structural data available, which comes in two forms: The magnetic moment of

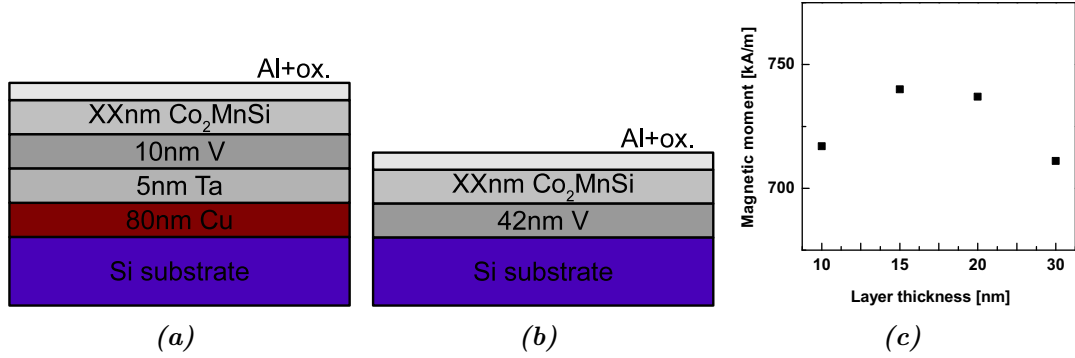


**Figure 3.16.:** Sample characterization for  $\text{Co}_2\text{MnSi}$ , series CMSXX and He150X: layer stacking for (a) CMSXX and (b) He150X, (c) magnetic moment for CMSXX. The magnetization of the CMSXX samples is roughly the same for all thicknesses of the Heusler layer.

the samples has been measured using an *advanced gradient magnetometer* (AGM). Also, the structural properties of most of the samples were investigated by means of x-ray diffraction (XRD). The results of XRD measurements are presented using the so-called *netarea*, which is the integrated intensity of the  $L2_1$  (004) peak of the Heusler structure. It is a measure for the textured area of the sample. All structural data measurements have been performed externally by the collaborators that produced the samples.

First is the full Heusler  $\text{Co}_2\text{MnSi}$ . This compound has received large interest in the past few years, especially for its use in the design of *magnetic tunnel junctions* (MTJ). Sakuraba et al. found *tunneling magnetoresistance* (TMR) values of up to 570% at low temperatures [SHO<sup>+</sup>07],<sup>28</sup> using tunnel elements of  $\text{Co}_2\text{MnSi}$  with aluminum oxide as barrier material. These were then the highest TMR values achieved for Heusler electrodes. From the theoretical point of view, Picozzi et al. predicted  $\text{Co}_2\text{MnSi}$  to be half-metallic [PCF04].

The samples investigated in this thesis have been prepared in the group of professor G. Reiss at the University of Bielefeld. The samples have been sputtered from stoichiometric targets. Samples of different series will be investigated with the main difference being the substrate. The samples from the first series, named CMSXX (XX = 10,15,20,30 denotes the Heusler thickness in nm) and He150X (X=2,6) are grown on a silicon substrate with a buffer of copper, tantalum, and vanadium for CMSXX and a vanadium buffer for He150X. The Heusler layer is then (100)-oriented. The layers are capped with up to 2 nm of oxidized aluminum. The stacking is illustrated in Figs. 3.16(a) and (b), respectively. All samples have

<sup>28</sup> The TMR ratios named use the definition by Julliere, which corresponds to  $2P_L P_R / (1 - P_L P_R)$ . Here,  $P_i$  are the polarizations for the left and the right electrode, respectively.

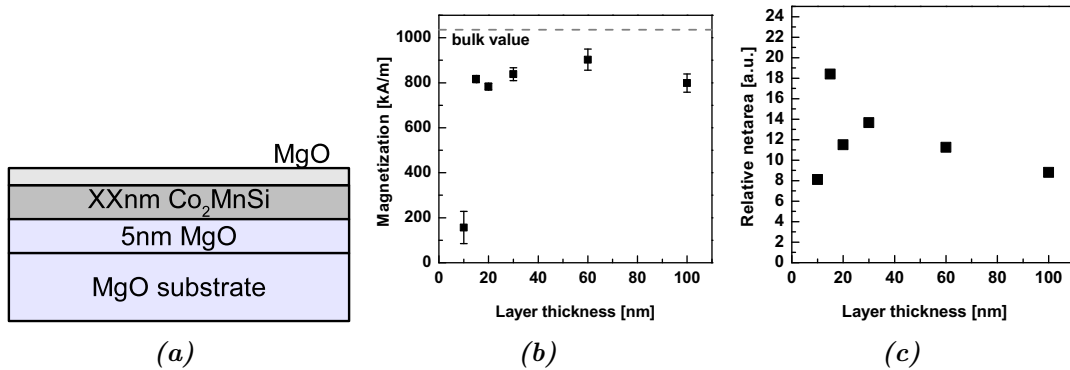


**Figure 3.17.:** Sample characterization for  $\text{Co}_2\text{MnSi}$ , series DE90702: (a) layer stacking, (b) magnetic moment, (c) relative textured sample area, given as the netarea divided by the sample thickness in nm. Except for the thinnest film, all samples show about the same amount of ordering, reaching magnetic moments of 80% of the bulk value.

been annealed at temperatures above  $400^\circ\text{C}$  for one hour. Concerning structural data, only the AGM measurement for the samples of series CMSXX is available, shown in Fig. 3.16(c). It shows that the magnetization of the films of  $d = 15$  and  $20$  nm is slightly higher, but overall variations are small. The  $\text{Co}_2\text{MnSi}$  samples show polarizations of  $P = 66\%$  in tunnel experiments [SKRH05].

Samples from the second set, comprising the series DE90702 and DE90305C, are grown on 5 nm MgO on top of a MgO(100) substrate with an 1.8 nm MgO cap layer. The stacking is depicted in Fig. 3.17(a) and 3.18(a), respectively. Samples from the series DE90702 vary in the thickness of the Heusler layer and are compared to the samples on Si with the same Heusler thickness. All samples from this

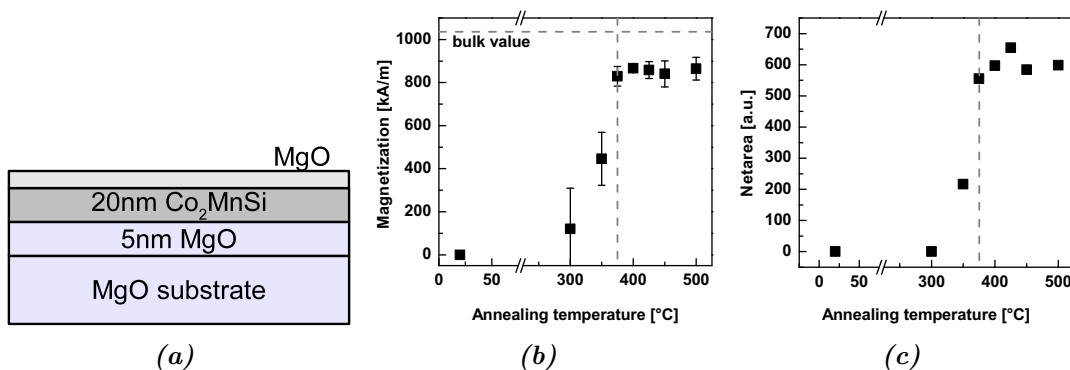


**Figure 3.18.:** Sample characterization for  $\text{Co}_2\text{MnSi}$ , series DE90305C: (a) layer stacking, (b) magnetic moment, (c) textured sample area. Samples annealed at temperatures of  $375^\circ\text{C}$  and higher are magnetic, as indicated by the vertical lines.

series have been annealed at 400° C for one hour. Structural data (magnetic moment by AGM and the netarea of the XRD (004) peak) is provided in Figs. 3.17(b) and (c). All samples show a high magnetization, except for the thinnest Heusler film ( $d = 10$  nm), for which the magnetic moment is considerably lower. The former samples reach values of about 80% of the bulk value of  $M_s$ . However, these values are not corrected concerning a possible decrease of the Heusler thickness during the process of annealing. For this special series of samples, the netarea in Fig. 3.17(c) has been divided by the thickness of the Heusler film to allow for comparison between films of different thickness. The films of higher  $d$  show a decreased relative textured area, if one disregards the film of  $d = 10$  nm with its low magnetic moment.

Due to structural disorder,  $\text{Co}_2\text{MnSi}$  samples are in general non-magnetic after sputtering if produced at room temperature. To improve order and reach a magnetic state, the samples are annealed at high temperatures. The effect of varying the annealing temperature is studied systematically in the case of series DE90305C. It can be seen from the magnetization data in Fig. 3.18(b) that the samples become magnetic if annealed at temperatures of 375° C and higher, indicated by the vertical line.<sup>29</sup> Beyond this, there is no trend visible for the variation of the annealing temperature. Again, values of about 80% of the bulk value of  $M_s$  are reached. The variation of the XRD results (again displayed in terms of the netarea) in Fig. 3.18(c) shows the same trend. Finally it should be noted that up to now attempts at tunneling experiments with  $\text{Co}_2\text{MnSi}$  tunnel electrodes grown on MgO from the target used to produce the samples under investigation did not yield any results. The problem here is that the high required annealing temperatures lead to diffusion of atoms from the Heusler film into the barrier. In particular there is no proof that the polarization  $P$  is higher than for electrodes grown on Si, as one would expect for the epitaxially grown samples on MgO.

The second Heusler compound investigated is  $\text{Co}_2\text{FeAl}$ . While it was originally predicted to be half-metallic, recent investigations found that  $\text{Co}_2\text{FeAl}$  is not a half-metal by itself. Calculations by Sargolzaei et al. resulted in a spin polarization of only 38% [SRK+06]. The calculation scheme used by the authors was the *full potential local-orbital* (FPLO) minimum-basis band structure method. Actual measurements performed by Karthik et al. using *point contact Andreev reflection* (PCAR) found a value of 56% [KRT+07]. Nevertheless, this difference in results can be attributed to the difference of methods used for determination of  $P$ . While the obtained values of  $P$  might seem as if  $\text{Co}_2\text{FeAl}$  is an unsuitable material

---

<sup>29</sup> Only these samples can be used for TRMOKE measurements.

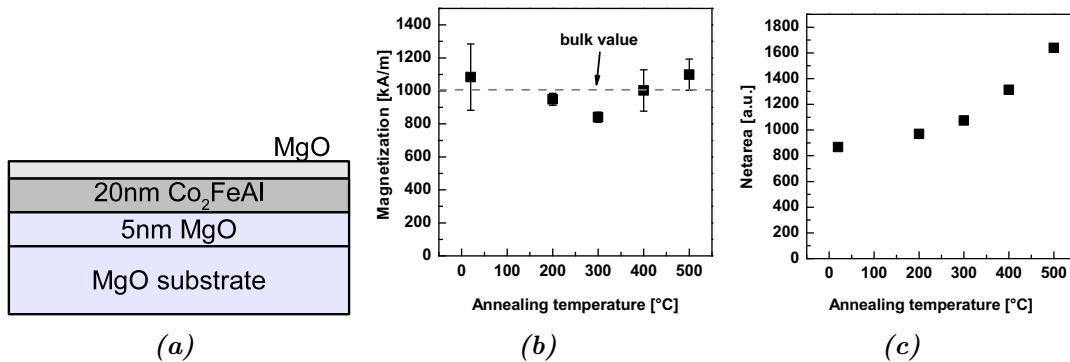


**Figure 3.19.:** Sample characterization for  $\text{Co}_2\text{FeAl}$ , series DE90225E: (a) layer stacking, (b) magnetic moment, (c) textured sample area.

for the search of a half-metal, it is nevertheless widely used in composite alloys, where the iron is gradually substituted with e.g. chromium as performed by Fecher and coworkers [FKW<sup>+</sup>05]. Pure  $\text{Co}_2\text{FeAl}$  only shows a very small band gap of 0.1 eV with the Fermi  $E_F$  energy almost touching the lowest unoccupied minority band. This is often cited as the reason why no half-metallicity is found at finite temperature. The case of doping  $\text{Co}_2\text{FeAl}$  with chromium is of special interest, because the lattice mismatch between  $\text{Co}_2\text{FeAl}$  and  $\text{Co}_2\text{CrAl}$  is negligibly small, so in a first approximation one can assume that the only effect induced by substituting Fe with Cr is a reduction of the number of  $d$ -electrons. By doping  $\text{Co}_2\text{FeAl}$  with chromium it is possible to widen the very small band gap of pure  $\text{Co}_2\text{FeAl}$  to up to 0.8 eV. This is one of the examples showing the wide range of applicability of Heusler compounds in the search of half-metals.

Coming back to the present study, only samples of pure  $\text{Co}_2\text{FeAl}$  will be investigated. Like the previous  $\text{Co}_2\text{MnSi}$  samples, they have been prepared in the group of professor G. Reiss at Bielefeld. For the series investigated (DE90225E) the annealing temperature was varied. This should affect the ordering and therefore, of course, the polarization. The samples consist of a 20 nm Heusler layer grown on an 5 nm MgO buffer on top of a MgO(100) substrate and are capped with 1.8 nm MgO. The stacking along with the structural data is shown in Fig. 3.19. From the magnetic moment exhibited by the films (see Fig. 3.19(b)) one can deduce that the Heusler is to a certain degree already ordered at room temperature, as opposed to  $\text{Co}_2\text{MnSi}$ . The films reach values of the magnetic moment equivalent to the bulk value. The results of the XRD measurements displayed in Fig. 3.19(c) indicate that the ordering of the Heusler films increases monotonously with increasing annealing temperature up to a maximum at 500° C (and maybe even beyond this

value, where no samples were available). The parameter given is again the net area of the XRD (004) peak. In contrast to the theoretical predictions, tunnel experiments with a  $\text{Co}_2\text{FeAl}$  electrode at Bielefeld have shown that the samples exhibit a spin polarization of up to 86%. In addition  $\text{Co}_2\text{FeAl}$  exhibits a strong quadratic Kerr effect. This will hamper the analysis, as will be discussed in chapter 4.2.

The next samples are of the half Heusler compound  $\text{CoFeGe}$ . The samples were provided by Hitachi Global Storage Technologies. There are three series of samples with varying Heusler compositions, and all samples contain a 25 nm Heusler layer. The first two samples (series LG0514CO2) have been deposited at high temperatures onto  $\text{MgO}(100)$  and  $\text{MgO}(110)$ , which causes the Heusler layer to be epitaxial with orientations of (100) and (211), respectively. These samples are of the composition  $(\text{CoFe})_{72}\text{Ge}_{28}$ . These films tend to grow in a B2 structure rather than an  $\text{L2}_1$  structure [LWM<sup>+</sup>09], the difference being that the former has a disorder between the X,Y sites (Co,Fe) and the Z sites (Ge) of the structure (cf. Fig. 2.4). For high Ge concentrations (above 30%) the samples become microcrystalline. However, for the samples under investigation XRD measurements (not shown here) indicate good epitaxy of the Heusler layers. The second series, LG0611B0X ( $X=1..4$ ), comprises polycrystalline samples grown at room temperature on glass with germanium concentrations of 25% and 28%. Two samples of each composition are capped with ruthenium in order to investigate the effects of capping layers on the pump-probe investigation. All samples are provided in a non-annealed (set a) and an annealed (set b) version. The third series, LG0603B0X ( $X=1,3$ ), compares epitaxial Heusler films with 25% Ge on  $\text{MgO}(100)$  and (110) to pure CoFe on similar substrates. These last samples have also been deposited at high temperatures, but are not annealed. The stacking for all  $\text{CoFeGe}$  (and CoFe) samples is sketched in Fig. 3.20

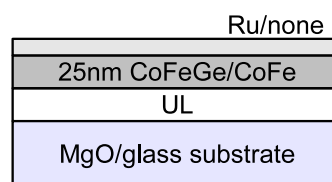


**Figure 3.20.:** Layer stacking for  $\text{CoFeGe}$ .

The next series, LG0604B0X ( $X=1..6$ ), is of the full Heusler compound  $\text{Co}_2\text{MnGe}$ . These samples have also been provided by Hitachi GST. There are three series with Ge concentrations varying from 21% to 29%. For every concentration there are epitaxial samples on  $\text{MgO}(100)$  and (110) and polycrystalline samples on glass. The stacking is sketched in Fig. 3.21. These series can be used to investigate the effect of gradual variation of the Ge concentration, but also to check if the all-optical approach is capable of visualizing the effects of these gradual changes.



**Figure 3.21.:** Layer stacking for  $\text{Co}_2\text{MnGe}$ .

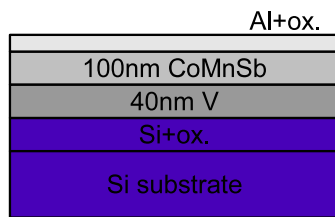


**Figure 3.22.:** *Layer stacking for CoMnSb.*

Lastly, the half Heusler compound CoMnSb is studied. This compound is of interest, because it has been predicted by Galanakis and Mavropoulos to be clearly half-metallic with a spin polarization of 99% at the Fermi level [GM07]. Also, the  $Z$  element antimony is the heaviest element on this site for all Heusler samples investigated in this thesis. This results in an enlarged spin-orbit coupling parameter  $\zeta_{SO}$  (cf. Eq. (3.14)), which should work against the spin polarization. The sample investigated was again prepared in the group of professor G. Reiss at Bielefeld. It consists of a 100 nm CoMnSb film grown on an oxidized silicon layer and capped with 1.6 nm aluminum oxide, as sketched in Fig. 3.22. The exact composition of the Heusler is  $\text{Co}_{32.4}\text{Mn}_{33.7}\text{Sb}_{33.8}$ .

# Chapter 4.

## Measurements and Analysis

The presentation of the results for the measurements has to be preceded by some comments. The data will be presented by type of material, where for every material an additional aspect of the evaluation is presented. For example, the presentation of the results for  $\text{Co}_2\text{MnSi}$  will lead to the discussion of the appearance of the step-like feature discussed in chapter 3.3. In the course of the discussion, both demagnetization and reflectivity measurements are presented. The Kerr signal in the demagnetization curves is always the difference from two measurements of opposite directions of the applied field  $\vec{H}$ . All demagnetization data are inverted in order to match the 3TM fit, which shows the rise in temperature. The actual magnetization is of course decreased. If multiple curves appear in one graph, they have been shifted for clarification. All fits according to the 3TM are performed using Eq. (A.12) if not stated otherwise. Details on the data processing and the fit procedure are given in chapter B.2.

### 4.1. $\text{Co}_2\text{MnSi}$

First in the presentation of the results is  $\text{Co}_2\text{MnSi}$ . In the following, also the application of the data evaluation method to measurements will be explained and the occurrence of the 'step-like' feature introduced in the expansion of the 3TM (chapter 3.3) will be discussed.

Figure 4.1 shows demagnetization and reflectivity data for  $\text{Co}_2\text{MnSi}$  films of various thicknesses grown on Si. Note that the reflectivity measurements (Fig. 4.1(b)) do not represent the relaxation time  $\tau_E$  observed in the measurement of the Kerr rotation. This can be seen for films of 30 nm and 60 nm, where a weak additional oscillation is present. Such a phenomenon can be attributed to a thermally induced stress wave. A detailed analysis will follow later on during the discussion of the measurements on CoFeGe (chapter 4.3). For the discussion

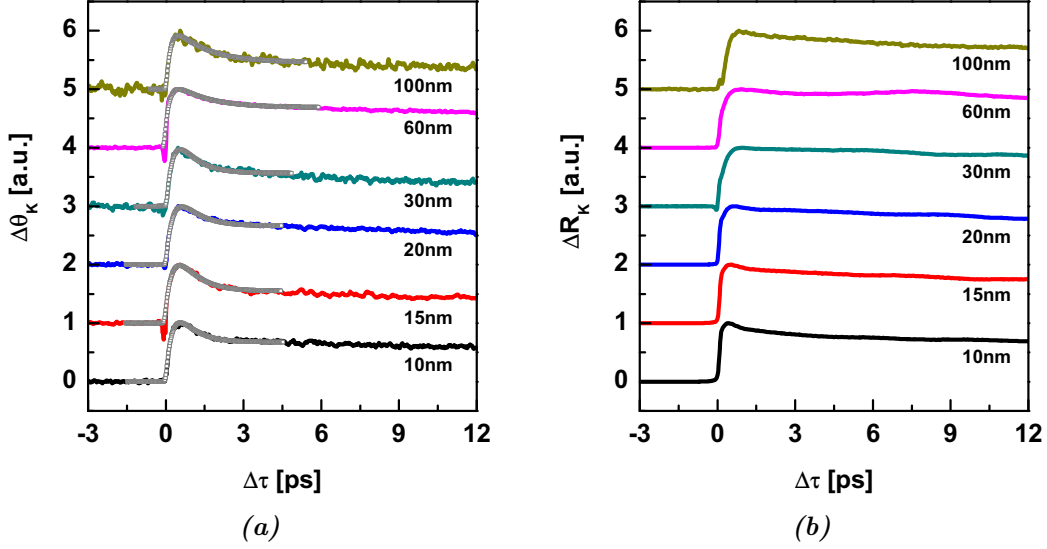


**Figure 4.1.:**  $\text{Co}_2\text{MnSi}$ , series CMSXX and He150X: (a) Kerr rotation, (b) reflectivity. The gray squares represent a fit of the Kerr signal according to the 3TM. The reflectivity is not fitted due to the presence of thermally induced stress wave, as visible for the films of  $d = 30$  and  $d = 60$  nm.

of the present measurements it is therefore better to resort to a direct fit of both timescales to the demagnetization curves in Fig. 4.1(a).

In order to investigate the influence of the substrate type on the ordering and the polarization, the results for the samples on Si have to be compared to those for the samples on MgO.<sup>30</sup> The latter are shown in Fig. 4.2. The Si substrate with V buffer and the MgO(100) substrate stabilize the growth of the Heusler layer in the (110) and the (100) direction, respectively.

It is obvious that the demagnetization measurements on the  $\text{Co}_2\text{MnSi}$  samples on MgO exhibit stronger noise.<sup>31</sup> This time, additionally, the reflectivity reveals a clearly different behavior for the four thinnest films. For these films of thickness  $d$  up to 30 nm the signal changes its sign shortly after an initial peak. This is an effect of the overlap of the electron and lattice contributions of different sign mentioned in the discussion of Eq. (3.20) describing the change  $\Delta R$  of the reflectivity. With increasing sample thickness the sign and the magnitude of these contributions change, leading to the observed trends. Again, there is a stress

<sup>30</sup> These samples were annealed at  $400^\circ\text{C}$  for one hour.

<sup>31</sup> Nevertheless, this is a special feature of this particular measurement and not a generic feature of the MgO substrate, as can be seen by comparing these measurements to those of Fig. 4.4.

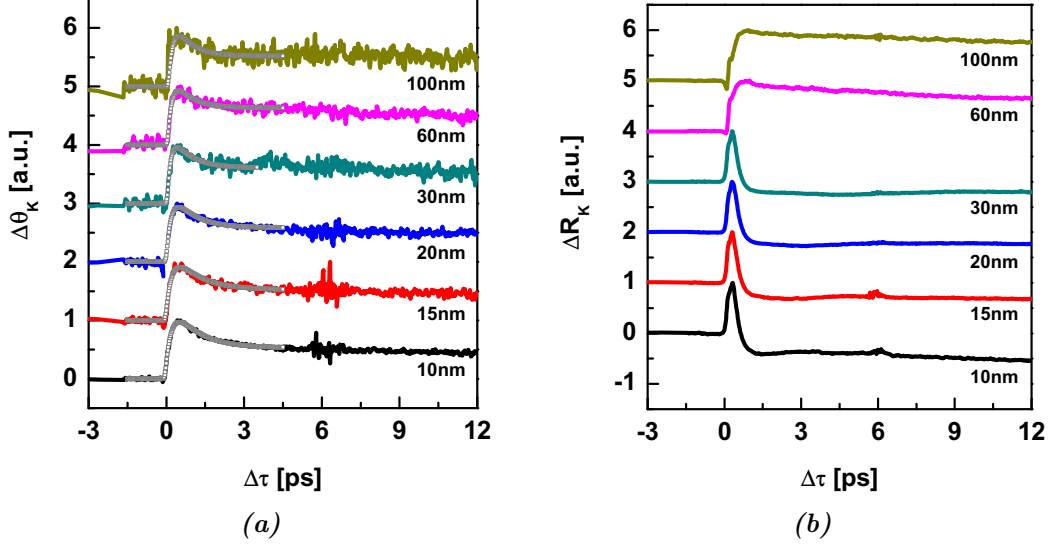


**Figure 4.2.:** Co<sub>2</sub>MnSi, series DE90702: (a) Kerr rotation, (b) reflectivity. The gray squares represent a fit of the Kerr signal according to the 3TM. Note the different characteristics of the reflectivity signal for thicknesses of  $d = 60$  and  $100$  nm and those of  $d = 30$  nm and less. For the latter, the reflectivity changes its sign after an initial peak. Also, the final slope of the reflectivity has a different sign for the samples of  $d = 15$ ,  $20$ , and  $30$  nm than for the other samples. These observations reveal a difference in sign of the electron and the lattice contribution to the reflectivity and the presence of a thermally induced stress wave, respectively.

wave present, causing the different slopes of the reflectivity at  $\Delta\tau = 12$  ps for the four thinner films. The two thickest films ( $d = 60$  and  $100$  nm) behave similar to their analogues on Si. This is expected, because in general the influence of the underlayer on the ordering of the sample should diminish with increasing layer thickness. Likewise, the dynamics of films of thickness  $d \gg \lambda$  should not be strongly influenced by the attributes of the sample. The penetration depth  $\lambda$  for Heusler alloys is about 20 nm. Additionally, as stated during the discussion of the contributions to  $\Delta R$ , for the case of  $d \gg \lambda$  the excitation profile in the film is different, leading to the observed different relaxation behavior in this case.

The fitted timescales for the samples on Si and MgO are compared in Fig. 4.3. Here, it is gainful to connect the observations made in Figs. 4.1 and 4.2 to the received timescales. First, the values of the demagnetization time  $\tau_M$  obtained for each individual thickness  $d$  of the Heusler layer are higher for the samples on Si than for those on MgO as long as the  $d$  does not exceed 30 nm. Nevertheless, the relative variation of  $\tau_M$  for each series is similar. The samples of series He150X ( $d = 60$  and  $100$  nm on Si) show the same  $\tau_M$  as the corresponding films on MgO,

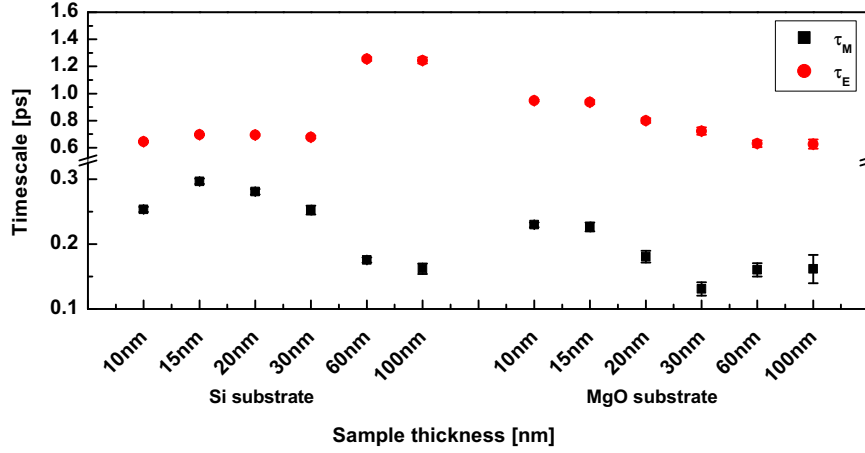


**Figure 4.3.:** Comparison of fitted timescales for  $\text{Co}_2\text{MnSi}$  samples on Si (left) and MgO (right) substrates. For the four thinner films on Si, the values for the demagnetization time  $\tau_M$  resemble the AGM data from Fig. 3.16(c). The samples on MgO show a similar trend. The two thickest films demagnetize on the same timescale, independent of the substrate.

but have a clearly enlarged relaxation time  $\tau_E$ . The samples on MgO show a monotonous decrease in  $\tau_E$ .

As already mentioned, a different relaxation behavior for the two thickest films is expected, because their thickness clearly exceeds the penetration depth of roughly 20 nm, leading to different excitations than in the case of the thinner films [DLM<sup>+</sup>06]. The decrease of  $\tau_E$  with  $d$  for the films on MgO can be explained by decreasing thermal influence as the film thickness increases. A stronger heating of the sample leads to a slowing down of the relaxation because of increased fluctuations of the magnetization. It would take too long to explain this mechanism in detail. However, the slowing down of the relaxation is a natural result from microscopic modeling using the Landau-Lifshitz-Bloch equation [ACFK<sup>+</sup>07].

It is interesting that the trend in  $\tau_M$  among the four thinnest films ( $d \leq 30$  nm) on Si resembles the AGM data from Fig. 3.16(c). The same trend is also visible for the films on MgO substrate, even though the absolute values of  $\tau_M$  and thus  $P$  are lower for the samples on MgO. Also, for the latter the trend is broken for the 10 nm film, whose demagnetization time is increased against the trend visible for the films on Si. However, structural data from Fig. 3.17(b) shows that this particular film has a very low magnetic moment, indicating a poor order of the Heusler layer. Consistent with the assumption that the substrate does not influence thicker films, the demagnetization time for the thickest films ( $d = 60$  and 100 nm) is independent of the substrate type. For the samples on Si, the

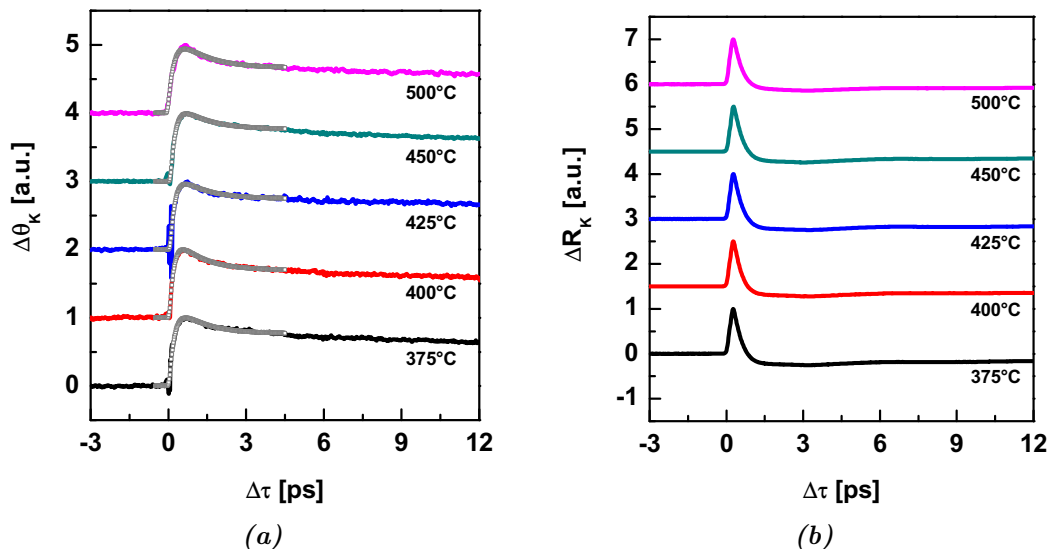


**Figure 4.4.:** *Co<sub>2</sub>MnSi*, series DE90305C ( $d = 20$  nm): (a) Kerr rotation, (b) reflectivity. Note that the reflectivity is similar to the one of the corresponding sample of  $d = 20$  nm in Fig. 4.2(b).

values of  $\tau_M$  are clearly lower for the two thickest films than for the four thinner films. However, these values are not fully comparable for the case of Si substrate, since the two sets of samples stem from series with different buffer layers.

The results for the samples on MgO can be compared to the structural data provided in Fig. 3.17. Except for the film of  $d = 10$  nm on MgO all samples show a similar magnetic moment without specific trends, which is also the result of the TRMOKE measurements. Overall, the faster demagnetization observed in the measurements indicates a considerably smaller polarization  $P$  for the films on MgO. This might be surprising because the epitaxial films on MgO are normally assumed to have a higher degree of order and thus a higher polarization visible as a lower demagnetization time. There is, however, no contradiction present, because (as of now) there are no data available that indicate that  $P$  is indeed higher for samples on MgO than for those on Si.

Next, the results for Series DE90305C comprising Co<sub>2</sub>MnSi samples on MgO annealed at various temperatures between 375° and 500° C are discussed. The measurements are shown in Fig. 4.4. The reflectivity curves for these films with a thickness of  $d = 20$  nm all look very similar to the corresponding case of Fig. 4.2. This proves that the form of the reflectivity curve is not affected by the ordering of the Heusler film but is rather shaped by the mentioned overlap of electron and lattice contributions to the reflectivity signal and possibly by heating of the

sample. The fit results are shown in Fig. 4.5. The relaxation times  $\tau_E$  are about

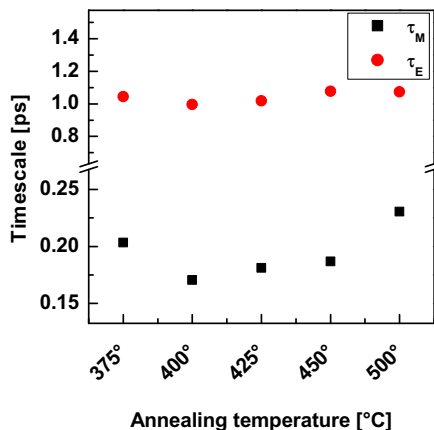


**Figure 4.5.:** Fitted timescales for  $\text{Co}_2\text{MnSi}$ , series DE90305C.

the same for all samples. This indicates that even if thermal effects (which lead, for example, to a slowing down of the dynamics) are present, they have the same impact on all samples, preserving the relative trends which could influence the values of  $\tau_M$ . The demagnetization times  $\tau_M$  do indeed differ, but they do not show a clear trend. The largest values are determined for the samples annealed at 375° C and 500° C, while the samples in between show a lower  $\tau_M$  which slowly increases with annealing temperature. However, as stated in the discussion of the structural data, there is not necessarily a pronounced effect of the variation of the annealing

temperature on the sample ordering above the critical value of 375° C.

Last in the discussion of the  $\text{Co}_2\text{MnSi}$  samples is the appearance of the step-like feature introduced in 3.3. This feature is visible for almost all samples of series CMSXX and DE90305C, but it is more pronounced for certain measurements than with the rest.<sup>32</sup> This is due to the fact that the feature appears on a timescale where the raw data shows an autocorrelation artifact from the overlap of the pump and the probe beam, as discussed in chapter B.2. After extracting the Kerr signal by subtracting the curve for one field from the other there is a residuum left due to non-perfect match of the artifacts for both curves.

Figure 4.6 shows the step-like feature for two samples from series CMSXX. The film thicknesses are 15 and 20 nm, respectively. In Fig. 4.6(a) the prominent change in the slope of the demagnetization is clearly visible. The gray lines indicate the different slopes, the arrows point at the intercepts appearing about 100 fs after demagnetization sets in. The observations can be attributed to the fact that the demagnetization time  $\tau_M$  changes over time, with lower values (i.e., faster demagnetization) directly after  $\Delta\tau = 0$  and higher values (slower demagnetization) later on. This is consistent with the proposed expansion of the 3TM. As already mentioned, the expanded 3TM can be solved numerically, and the resulting curves also show a step-like feature. A comparison between a measured curve and a generic result of the numerical simulation is displayed in Fig. 4.6(b). The feature appears in both curves and on the same timescale, although the slopes

<sup>32</sup> Unfortunately, the results for series He150X and DE90702 show too much noise to clearly assess the appearance of the feature.

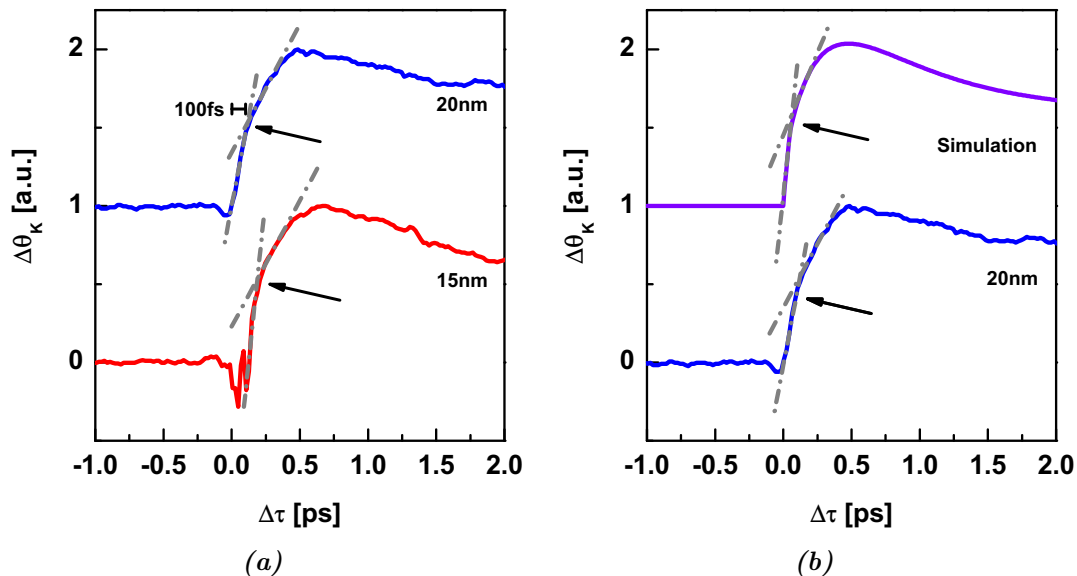


**Figure 4.6.:** Step-like feature on the very short timescale in Co<sub>2</sub>MnSi, series CMSXX: (a) appearance in 15 nm and 20 nm sample, (b) comparison between step for 20 nm sample and a numerical solution of the expanded 3TM (cf. Fig. 3.10). The change in slope appearing at a delay time  $\Delta\tau$  of about 100 fs is clearly visible. The gray lines are guides to the eye, illustrating the two different slopes of the demagnetization process. The arrows mark the intercept of the two lines.

are slightly different. This is, however, only a matter of the exact choice of the parameters used in the simulation. Of course, the curves can be brought to accordance by fitting the parameters of the simulation, but this task is rather tedious. The important point is that the step-like feature appearing on the timescale of 100 fs can be described by the expansion of the 3TM. Nevertheless, it is difficult to gain information on the most interesting part, namely the exact behavior before the change of slope appears. This takes place on a timescale too close to the resolution of the experiment<sup>33</sup> to yield reliable statements on the details of the step-like feature. The discussion of the observations made will be taken up again in chapter 4.6.

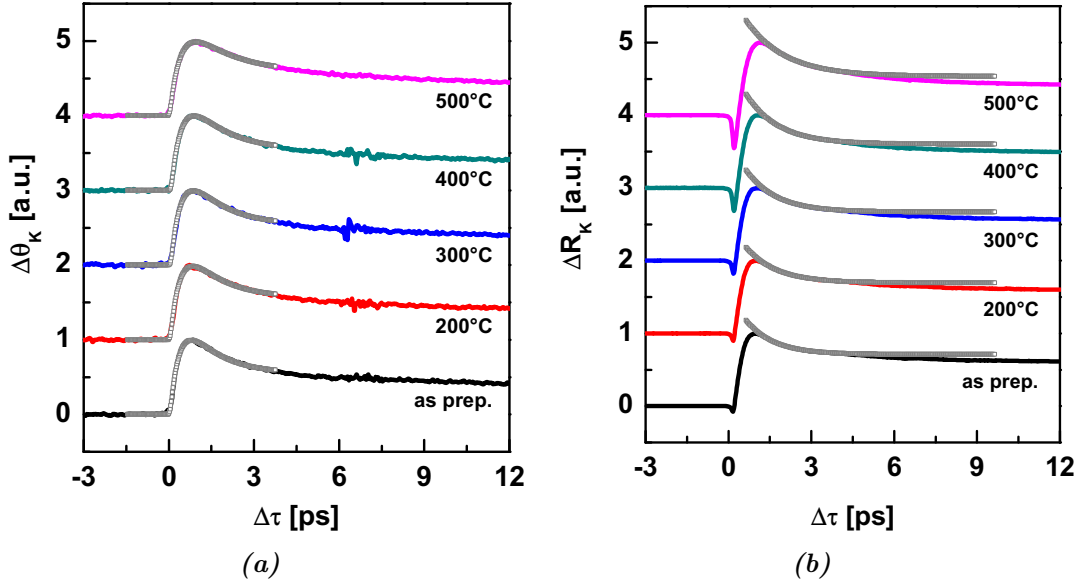


**Figure 4.7.:** *Co<sub>2</sub>FeAl*, series DE90225E: (a) Kerr rotation, (b) reflectivity. In this case, the reflectivity was fitted to extract the relaxation time  $\tau_E$ . Note that the reflectivity shows a feature around  $\Delta\tau = 0$  that gradually changes with annealing temperature and again indicates a lattice contribution to the reflectivity signal.

## 4.2. Co<sub>2</sub>FeAl

### 4.2.1. Ultrafast demagnetization

Next is the discussion of the results for Co<sub>2</sub>FeAl. The curves measured for the samples annealed at different temperatures are shown in Fig. 4.7. The demagnetization curves in Fig. 4.7(a) are very similar to those of Co<sub>2</sub>MnSi in Fig. 4.1(a), but the maximum of demagnetization is reached later. For the Co<sub>2</sub>FeAl series, the reflectivity was fitted in order to obtain the values for the relaxation time  $\tau_E$ , as shown in Fig. 4.7(b). This is possible because the electron contribution (i.e. the parameter  $a$  in Eq. (3.20)) is small compared to the lattice contribution, so the reflectivity curves show an exponential decay with a time constant of  $\tau_E$  that can be fitted directly. The fitted curves (represented by gray squares) are drawn on a larger range than the actual fitting interval. The fitting interval has to be limited to a few picoseconds, because after this time the reflectivity signal shows additional features, e.g. from heat diffusion. Note that around  $\Delta\tau = 0$  there is a small feature which gradually becomes more prominent with increasing annealing temperature. It resembles the feature observed for the Co<sub>2</sub>MnSi films grown

<sup>33</sup> As a reminder: The limiting parameter is the pulse width  $w$ , which is roughly 60 fs.

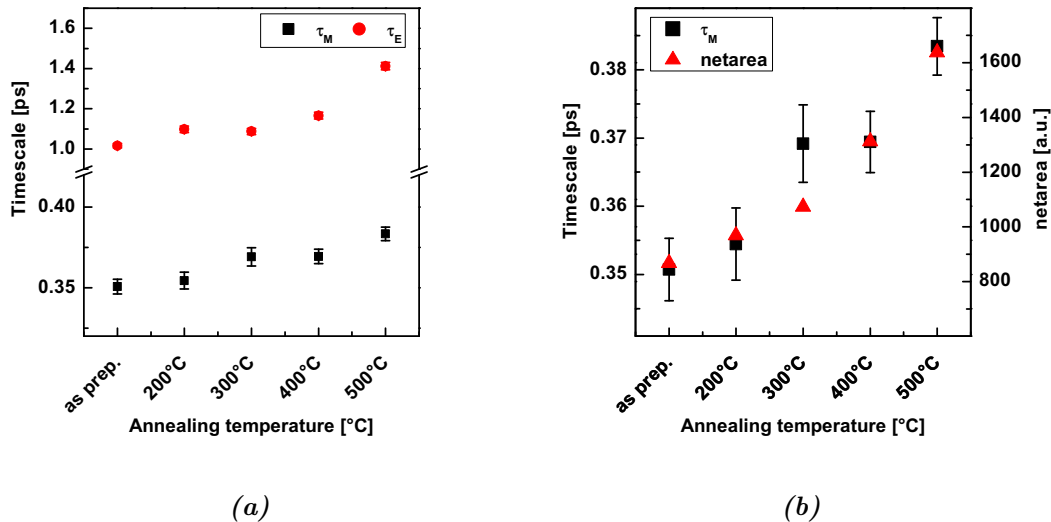


**Figure 4.8.:** Results of the fits for Co<sub>2</sub>FeAl samples with varying annealing temperature, series DE90225E: (a) fitted timescales, (b) comparison between extracted  $\tau_M$  and XRD data (displayed as netarea). The demagnetization time  $\tau_M$  and thus the polarization increase with the annealing temperature. Note the almost perfect congruence between the fitted values of  $\tau_M$  and the XRD results.

on MgO (cf. Fig. 4.4(b)) and thus it is also interpreted as the overlap of electron and lattice contributions, where the former obviously become stronger for samples annealed at higher temperatures.

The results of the fits are shown in Fig. 4.8. The fitted demagnetization times  $\tau_M$  are clearly larger than for Co<sub>2</sub>MnSi, as expected from the higher spin polarization ( $P = 86\%$  compared to  $P = 66\%$ ). Also, both  $\tau_M$  and  $\tau_E$  increase with the annealing temperature of the sample. This trend is exactly the same as in the XRD measurements (cf. Fig. 3.19(c)) and reflects the fact that the polarization is higher for samples which are annealed at higher temperatures. The important insight is that the demagnetization time  $\tau_M$  is clearly correlated to the degree of ordering determined from the XRD measurements. This is a direct proof that a better structure of the Heusler layer results in a higher polarization  $P$ .

#### 4.2.2. QMOKE

The next point is the discussion of the already mentioned strong quadratic magneto-optic Kerr effect (QMOKE) exhibited by the Co<sub>2</sub>FeAl films. The strength of the QMOKE also increases with the annealing temperature, but it has to be stressed

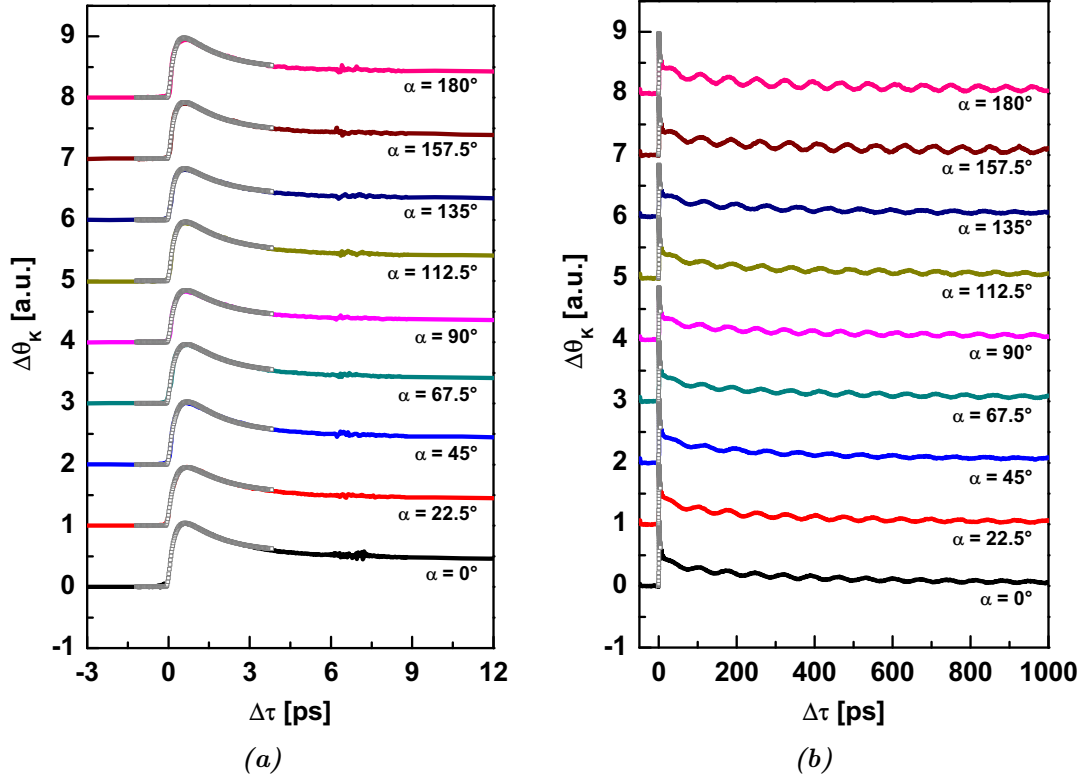


**Figure 4.9.:** *Co<sub>2</sub>FeAl*, series DE90225E: Angular dependence of Kerr rotation on (a) short timescale, (b) long timescale. The QMOKE in *Co<sub>2</sub>FeAl* adds an oscillatory contribution to the demagnetization signal on the long timescale.

here that the trend observed for the demagnetization time  $\tau_M$  is *not* influenced by the QMOKE.<sup>34</sup> Since the QMOKE is also sensitive to the ordering and thus most prominent for the sample annealed at 500° C, this sample is chosen for the following investigation. The investigation of the QMOKE is necessary to correctly interpret the measurements, and in particular to rule out that it influences the dynamics on the short timescale in Fig. 4.7.

The main effect of the QMOKE is an additional oscillation in the demagnetization on the long timescale (up to 1 ns). This is reminiscent of the precessional motion according to the LLG (2.6), but it has to be stressed that here the origin of the oscillation is a different one, because in all measurements the field is applied in-plane (cf. Fig. 3.4). In Fig. 4.9 the measurements on the sample annealed at 500° C for different angles  $\alpha$  of sample orientation are shown. In contrast to Fig. 2.6,  $\alpha = 0^\circ$  here corresponds to a field applied along the (100) axis of the

<sup>34</sup> A good indicator for this is that the oscillation caused by the QMOKE, which is discussed below, starts well after the end of the chosen fitting range.

MgO substrate, which is equivalent to the (110) axis of the Heusler L2<sub>1</sub> structure [CJHA07]. The additional oscillation is clearly visible on the long timescale (Fig. 4.9(b)), and it is still present in the asymmetric part of the Kerr signal that is displayed. This means that while it is not as prominent as in the raw data (not shown here), it is not completely symmetric for different directions of the field and thus does not cancel out in the difference of the signals for opposite directions of the external field  $\vec{H}$ . Therefore, it has to be of magnetic origin. The reflectivity (not shown here) shows no oscillatory feature. In the following, the dynamic QMOKE has to be studied in detail to examine its influence on the performed dynamics measurements. In particular, it is necessary to check if the evaluation of the data is influenced by the QMOKE. The dynamic QMOKE has to date not been studied in detail, although its effects are quite intriguing. There is a number of observations to be made on the presented measurements. But before going into the details of the dynamics QMOKE, a short overview of the static QMOKE in Co<sub>2</sub>FeAl is given.

Fig. 4.10 shows angular-dependent hysteresis loops for a Co<sub>2</sub>FeAl sample annealed at 500°C. The loops have been decomposed into their asymmetric and symmetric parts (cf. chapter 2.4). The strength of the QMOKE is given by the symmetric part of the hysteresis loop. The measurements show that the sample has easy axes at  $\alpha = 0^\circ$  and  $90^\circ$  and hard axes at  $\alpha = 45^\circ$  and  $135^\circ$ . This means that the easy axes correspond to the {110} axes of the Heusler.<sup>35</sup> The QMOKE is strongest near the hard axes, but its maximum is *not* found directly at the position of the hard axes. This is due to the fact that the QMOKE has several contributions (cf. Eq. (2.18)), two of which are proportional to

$$(1 - \cos(4\alpha)) M_L M_T \quad \text{and} \quad \sin(4\alpha) (M_L^2 - M_T^2),$$

respectively. These contributions vanish for measurements performed exactly along the prominent axes. Along the easy axes, QMOKE is only detectable for applied fields of about  $H_C$ , i.e. directly at the points of magnetization reversal. For easy axis reversal the terms dependent on  $\alpha$  vanish just as for hard axis reversal. However, there remains a contribution proportional to  $M_L M_T$  that is independent of  $\alpha$ .

Applying the field along the easy axis one has  $M_T = 0$ , and  $M_L$  changes abruptly from -1 to +1 upon reversal of the magnetization, limiting the the only non-zero QMOKE contribution to this very point. While the actual shape of

---

<sup>35</sup> The edge of the sample corresponds to the MgO (100) direction and to the (110) direction of the Heusler's L2<sub>1</sub> structure, as usual [CJHA07].

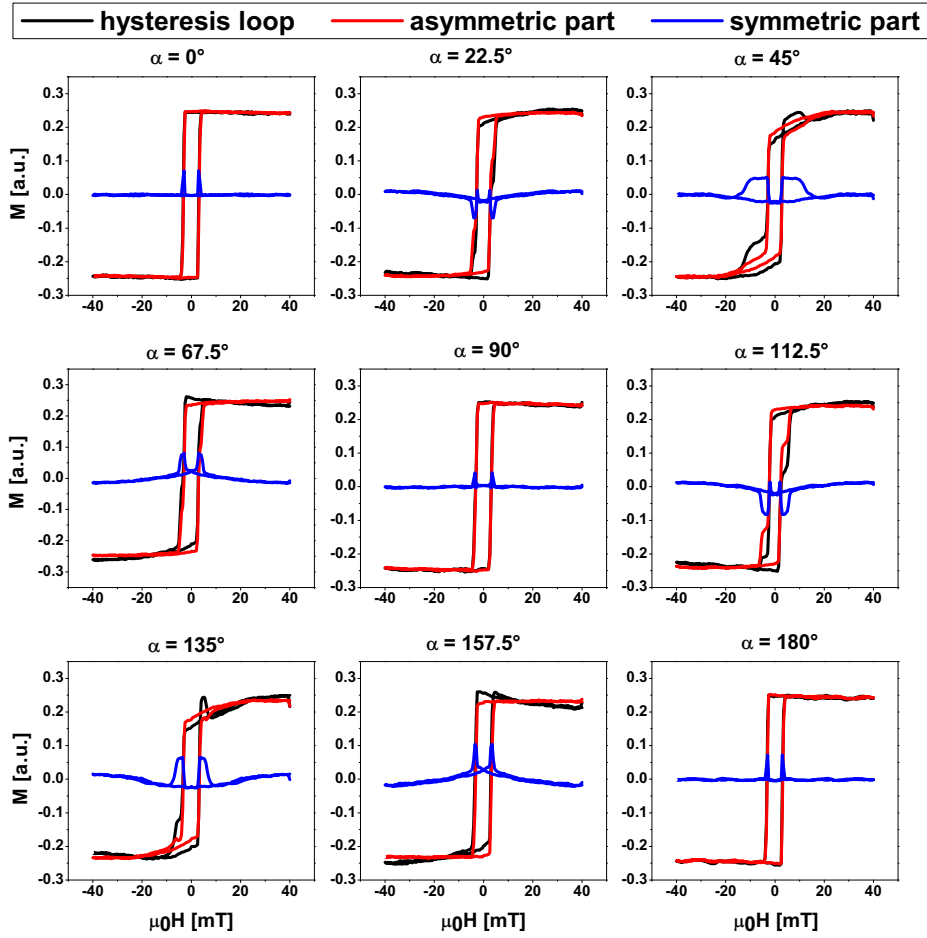


**Figure 4.10.:** Hysteresis loops for a  $\text{Co}_2\text{FeAl}$  sample annealed at  $500^\circ\text{C}$ . The strong QMOKE contribution is extracted from the loops by decomposition into asymmetric and symmetric part.

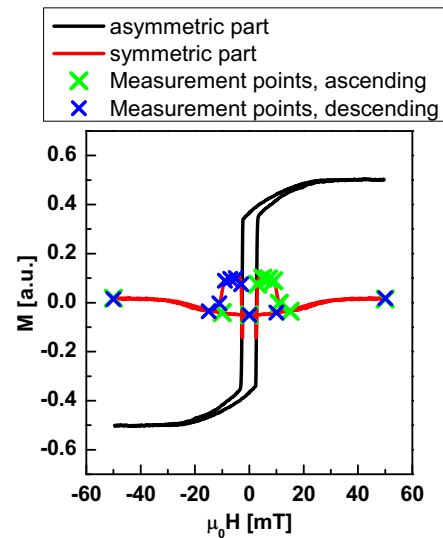
the QMOKE signal is difficult to understand due to its strong dependence on the details of the magnetization reversal process, namely the timely evolution of  $M_L$  and  $M_T$ , the angular dependent hysteresis loops reflect very well the fourfold symmetry of the  $\text{L2}_1$  structure. This symmetry is also reflected in the symmetric part of the hysteresis, i.e. the QMOKE signal, but features small differences, e.g. for  $45^\circ$  and  $135^\circ$ . This does not indicate a different behavior, but is rather caused by the large error for  $\alpha$  (about  $3^\circ$ ) due to the fact that the sample is oriented manually. Deviations of the orientation from the prominent axis strongly influence the prefactors of the QMOKE contributions mentioned above, leading to the observed differences of the hysteresis loops for axes of the same type.

On the one hand, it was stated that the QMOKE is very sensitive to the magnetization reversal process, and on the other hand the demagnetization curves are computed as the difference of the Kerr rotation for maximum fields of opposite sign. This means that the sample was exposed to a fast, total change in the external field and the measurements shown in Fig. 4.9 seem unfit to study the dynamic QMOKE in detail. A better approach is to saturate the sample at maximum field and then gradually change the magnetization, measuring dynamics at points of prominent QMOKE strength. This will be called the 'descending' part of the measurement. Arriving at the maximum field of the opposite sign, the procedure

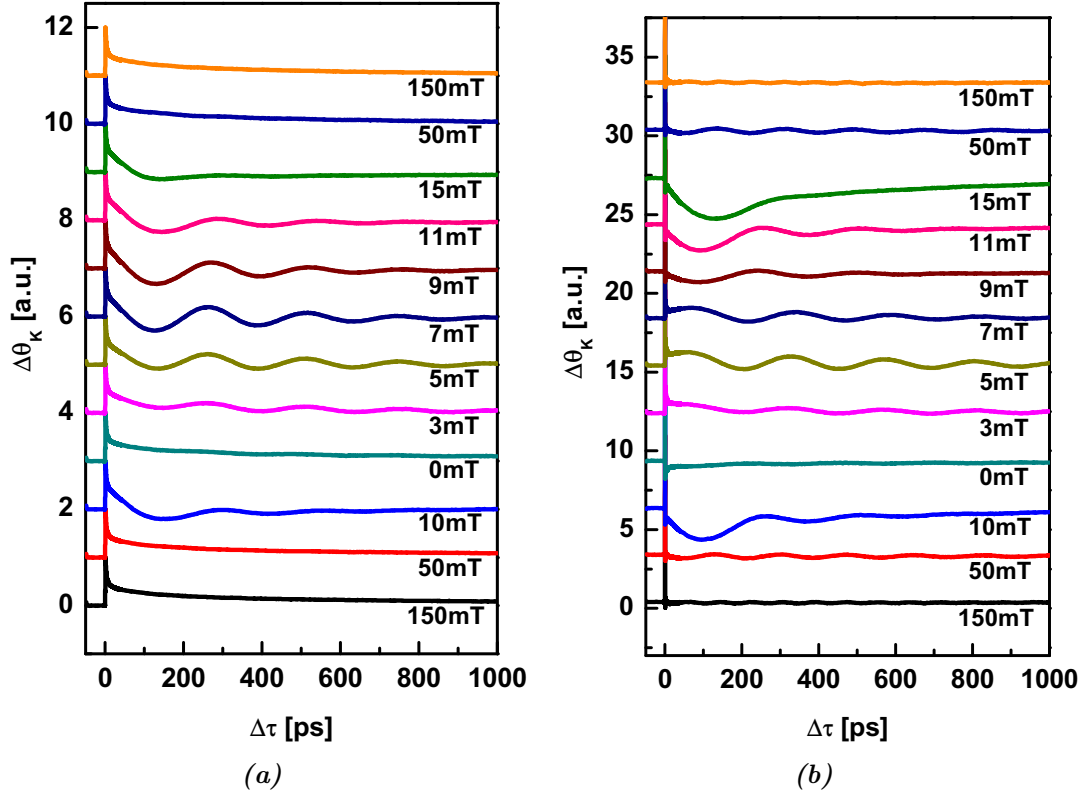
is reversed until the original field is reached, but the width of each step is chosen the same as for the first path. This will be called the 'ascending' part of the measurement. The procedure is illustrated in Fig. 4.11. It yields measurements for fields of opposite sign of the external field with equal strength of QMOKE. To gain more insight on the QMOKE, the difference and the sum of the associated points of the descending and the ascending measurements can be investigated. The assumption is that due to the gradual change of the field the magnetization reversal is also induced in a gradual way, facilitating the investigation of the QMOKE.

Figure 4.12 shows the results of the measurements performed as illustrated in Fig. 4.11. The dependence of the oscillation on the sequence of gradually changed external fields the oscillation is clearly visible. To prove that the oscillation is indeed induced by the QMOKE, the magnitude of the oscillation, determined in an appropriate way, has to be compared to the strength of the QMOKE signal. This is done by extracting the oscillatory part of the signals in Fig. 4.12, which is then Fourier transformed. The extraction is performed by subtracting the background from the signal. The background is assumed to be of a double-exponential form, with contributions from both incoherent magnons and from the restoration of the reflectivity due to remagnetization. These processes and their distinctive timescales have been studied in detail by Djordjević and Münzenberg [DM07]. The subtraction of the background was performed as described by Lenk [Len08].

The results are presented in Fig. 4.13(a), where the (normalized) FFT amplitude of the oscillation is plotted against the (also normalized) strength of the



*Figure 4.11.: Measurement points for Co<sub>2</sub>FeAl applying a gradually changed external field.*



**Figure 4.12.:** QMOKE-induced oscillation in  $\text{Co}_2\text{FeAl}$ : (a) Asymmetric and (b) symmetric part of the Kerr signal from measurements for gradual change of external field. From bottom to top, for each field value the difference (sum) of the descending and ascending measurements (cf. Fig. 4.11) has been taken to calculate the asymmetric (symmetric) part.

QMOKE determined as described at the end of chapter 2.4. The FFT amplitude is in general stronger for higher strength of the QMOKE, but a direct relation can not be determined from the data. The data points scatter a lot, which can be attributed to the inaccurate determination of the oscillation amplitude. The latter is hampered by the rather low resolution of the FFT (approximately 1 GHz) and the fact that some of the oscillations hardly last longer than a few periods. Nevertheless, it seems that the oscillation is indeed caused by the QMOKE, but further analysis has to follow. To determine the nature of the oscillation, the dispersion relation of the oscillation is plotted in Fig. 4.13(b). Although the points of measurement are sparsely distributed over the field range, the important details are visible: Due to its characteristic dispersion, the mode is definitely identified as a Kittel mode.<sup>36</sup> However, since the orientation  $\alpha$  of the sample was chosen to be

<sup>36</sup> There is no time to enter into the spin wave theory here. The interested reader will find extensive work in the literature (e.g. [Len08]).

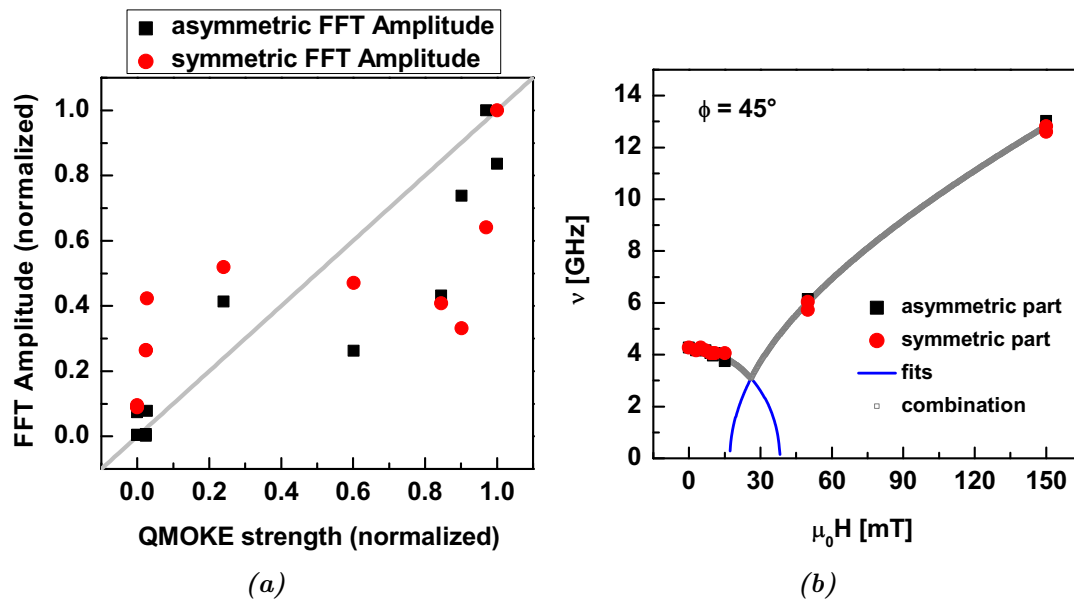


**Figure 4.13.:** Evaluation of the QMOKE-induced oscillation in Co<sub>2</sub>FeAl: (a) Correlation between QMOKE and oscillation for the asymmetric and symmetric part of the Kerr signal. Here, the normalized oscillation amplitude (received via FFT) is compared to the strength of the QMOKE signal. The gray line has a slope of one, modeling the case of a direct proportionality between the displayed quantities. The dispersion (b) reveals the induced oscillation to be a Kittel mode. Note that the dispersion is different from the standard Kittel formula, because the external field is applied at an angle  $\phi = 45^\circ$  with respect to the easy axis.

$45^\circ$ , the external field is likewise applied at an angle  $\phi = 45^\circ$  with respect to the easy axis of the sample (i.e., along the hard axis, as mentioned above). Therefore, when applying a small external field  $\mu_0 H$ , the magnetization is coherently rotated in the plane, until the field is strong enough to align the magnetization along the hard axis. This mechanism has been studied in detail by Müller et al. [MMMG08] for CrO<sub>2</sub> films, using an angle  $\phi$  of  $90^\circ$ . There, the (highly unusual) decrease of the frequency  $\nu$  with  $\mu_0 H$  for small fields is explained in terms of the dependence of the free energy  $\mathcal{F}$  on the angle  $\phi$ .  $\mathcal{F}(\phi)$  has two minima that shift towards one another with rising external field. At a critical value of  $\mu_0 H_{ext}$  the two minima concur, the free energy becomes flat, and the precession around the minimum (which is the cause of the oscillation) is no longer possible. This results in a drop of  $\nu$  to zero for the configuration where  $\phi$  has a value of  $90^\circ$ . The complete dispersion relation can be deduced analytically in this case. It was used to fit both branches of the measured dispersion relation, as shown in Fig. 4.13(b). However, the relation given by Müller et al. is based on the assumption of a twofold symmetry for  $\phi$ , while in the case of the Heusler L2<sub>1</sub> structure a fourfold symmetry

is present. Nevertheless, the considerations leading to the dispersion relation for the latter case should be completely analogous to the former case, because the twofold symmetry can be mapped onto the fourfold symmetry. Since for the fit in Fig. 4.13(b) the formulas for the twofold symmetry have been used, the fitted  $\nu$  does not reach zero. Instead, the fits of the two branches intersect, and as a first approximation this is taken as the minimum of the dispersion. A thorough analysis would require more data for external fields  $\mu_0 H$  between 20 and 40 mT. Then, a comparison to a theoretical model should be possible.

Finally it can be concluded that the  $\text{Co}_2\text{FeAl}$  samples exhibit a clearly slower demagnetization than the  $\text{Co}_2\text{MnSi}$  samples, consistent with the higher polarization  $P$  mentioned in the discussion of the samples. The QMOKE is very strong for this Heusler compound, but it shows no influence on the short timescale (below 20 ps). Measurements on the larger timescale, however, are clearly influenced by the QMOKE, and there is no obvious way of eliminating it from the measurement, as it is still present in the results of the detailed analysis, e.g. in Fig. 4.12. It has also been shown that the QMOKE induces a uniform oscillation of the magnetization. The dispersion of the oscillation matches the Kittel formula for the realized case of an external field applied along a hard axis.

## 4.3. CoFeGe

### 4.3.1. Ultrafast demagnetization

The evaluation of the CoFeGe samples will be a bit shorter than the previous ones. In contrast to the measurements on the  $\text{Co}_2\text{MnSi}$  and  $\text{Co}_2\text{FeAl}$  samples, for CoFeGe several different parameters (substrate type, cap layer, annealing and concentration) are varied rather than only one or two. Only one typical result for the measurements performed will be presented before the discussion of the results obtained. Additionally, in this section the occurrence of the stress wave observed for many of the reflectivity measurements will be treated in detail.

Figure 4.14 shows the measurements for series LG0611B0Xa, comprising polycrystalline samples on glass. The dynamics of these samples will be discussed exemplarily, while for the rest of the CoFeGe samples only the results will be presented. The four samples in Fig. 4.14 are of two different Ge concentrations (25% and 28%), and one of each concentration is capped with a thin layer of ruthenium. The samples have not been annealed. It is apparent that the reflectivity measurements are very noisy in comparison to the other measurements presented in this thesis, and they also show oscillations. Since this is not the case for other mea-

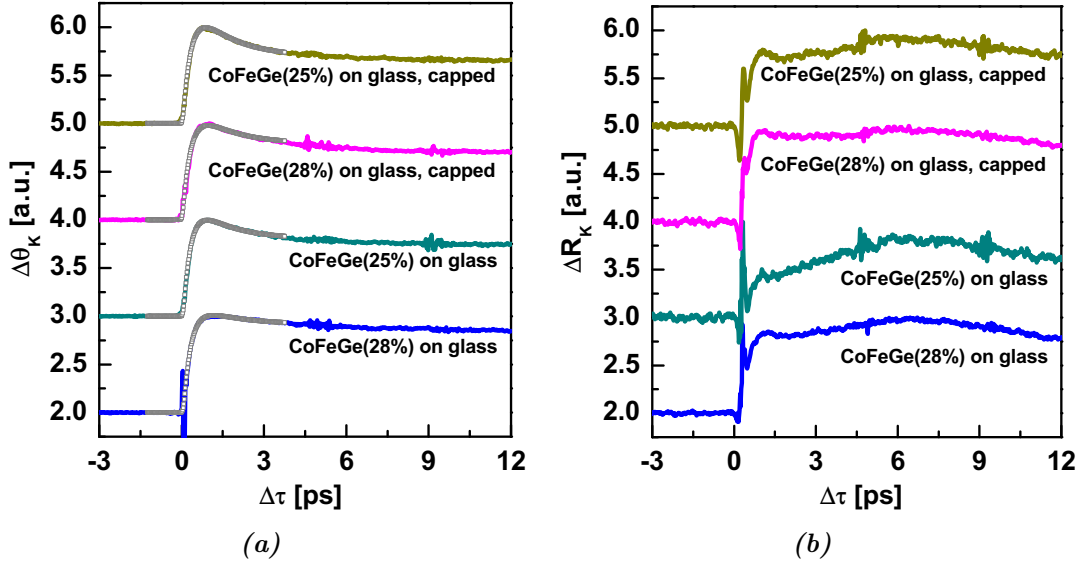


**Figure 4.14.:** CoFeGe, series LG0611: (a) Kerr rotation, (b) reflectivity. The samples are polycrystalline and have not been annealed. Again, only the demagnetization was fitted. Note that the reflectivity signal is noisy and shows strong oscillations. Also, the blue demagnetization curve (sample with 28% Ge, on glass) shows a slowing down of the relaxation compared to the other three curves.

measurements on CoFeGe, e.g. the annealed analogues of these samples (not shown here), both features can be regarded as properties of the non-annealed samples. However, the demagnetization curve for the non-annealed sample with 28% Ge (the blue curve in Fig. 4.14(b)) shows a slowing down of the relaxation that is clearly different from the other curves. Nevertheless, since this is an isolated measurement, it can be concluded that the slowing down is merely an artifact and does not indicate a trend due to the composition. This is bolstered by comparison to the capped sample of the same concentration (in the same figure) and to the annealed version of the sample (not shown; see Fig. 4.15 for results). Apart from this anomaly, the differences between the samples are small. For the fit only the demagnetization has been taken into account.

The results of the fit for all CoFeGe samples are shown in Fig. 4.15. First of all, the last four samples from the overview are of series LG0603B0X and compare CoFeGe with 25% Ge to pure CoFe. There is a clear difference visible, with values of  $\tau_M$  for CoFeGe being about 50% higher than those for CoFe. This is expected, because adding Ge to CoFe should yield a larger polarization than it is obtained for pure CoFe. The samples of CoFe can of course be interpreted as CoFeGe with 0% Ge content, so the performed measurements only provide two extreme values.

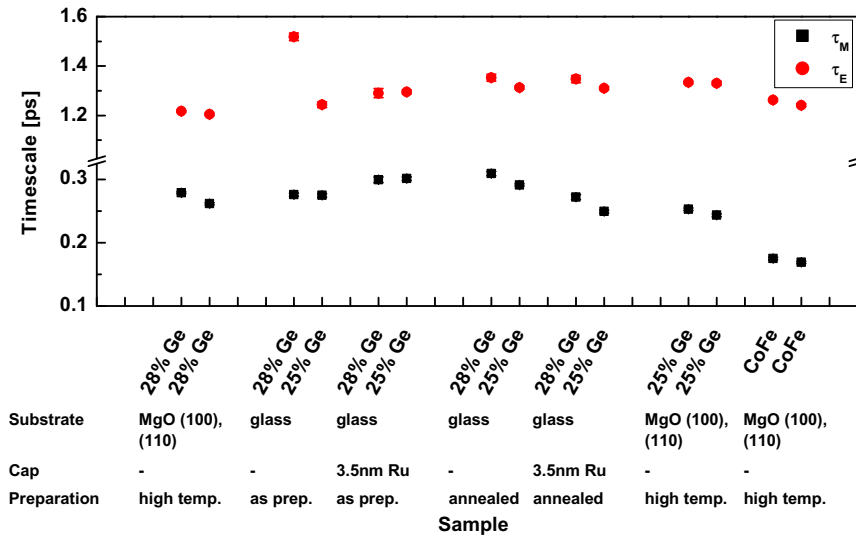


**Figure 4.15.:** Comparison of fitted timescales for all CoFeGe samples. The additional parameters are given below the sample composition. MgO as substrate type denotes samples on MgO(100) (left point) and MgO(110) (right point). Note the heightened  $\tau_E$  for the third sample, representing the anomaly for blue curve in Fig. 4.14(b)

It would be interesting to investigate CoFeGe samples with a wider range of Ge concentrations in order to learn more about the dependence of the dynamics on the Ge content.

The anomalous slowing down of the relaxation of the first sample of series LG0611B0Xa (corresponding to the third sample in this overview) is reflected in a measurably larger relaxation time  $\tau_E$ . Also, all samples grown on MgO(100) show higher values of  $\tau_M$  than those on MgO(110). This is interesting, because one would not necessarily expect such a clear trend in a system where the film changes its orientation according to the orientation of the substrate, with both orientations of the film being compatible with the corresponding substrate orientation. It indicates that the interface of the sample is more flawless for the first case.<sup>37</sup> Next, the polycrystalline samples on glass show on average a slower demagnetization than the ordered samples on MgO, contrary to what is expected, since the samples on glass are polycrystalline. For the uncapped samples on glass annealing increases  $\tau_M$ , indicating a better ordering of the Heusler layer. This observation matches the results of XRD investigations for CoFeGe samples with Ge concentrations above 25% performed by Maat et al. [MCC08]. Also, the values of  $\tau_M$  (and thus  $P$ ) are higher for concentrations of 28% than for 25%, consistent with the

<sup>37</sup> Remember that the polarization  $P$  and thus the demagnetization time  $\tau_M$  are very sensitive to defects at any interface.

results of investigations on spin valves performed by Maat et al. in the same work. The influence of the cap layer on the non-annealed samples is different from that on the annealed samples, raising  $\tau_M$  for the former while lowering it for the latter. A possible explanation is that the additional interface between the Heusler and the cap layer disturbs the ordering of the annealed structure, while for the non-annealed samples the ordering is not very high at all and the cap layer has a different effect which raises  $\tau_M$ . The latter might be a positive impact of the cap layer on the thermal properties of the sample. Samples on glass are in general more susceptible to thermal effects slowing down the demagnetization than samples on MgO, since the thermal conductivity of glass is much lower than that of MgO.<sup>38</sup> Here, care has to be taken when interpreting these experiments and further experiments are necessary to give a profound interpretation of the influence of the cap layer. Good candidates for such investigations are XRD measurements on the samples on glass and the determination of the grain size via a TEM picture of the Heusler/substrate interface. These would help to decide whether the observed effect of the cap layer is a result of poor film quality or indeed reflects a change in order and polarization.

### 4.3.2. Reflectivity experiments

As already noted, the reflectivity of the CoFeGe samples from series LG0603B0X shows a clean heat-induced shock wave. While this prohibits the extraction of the relaxation time  $\tau_E$  from the measurements, it contains interesting physics by itself. Therefore, it will be analyzed here shortly. The analysis also proves that the values of  $\tau_E$  are about the same for CoFeGe and CoFe, substantiating the result of the fit of the demagnetization. The reflectivity for one sample (CoFeGe with 25% Ge on MgO(100)) is shown in Fig. 4.16. It shows an oscillation in form of a damped sine plus an exponential background. The simple idea is that this oscillation is caused by a heat-induced expansion of the lattice, which then oscillate around their initial positions until the lattice cools down and the oscillation is damped out. Such processes have been studied in more detail (regarding, for example, the propagation of the stress wave through the sample) in the literature [TGMT86]. The oscillation superimposes the expected reflectivity signal representing the electron temperature according to the 2TM, and has a different sign. This latter fact has been observed before in the measurements presented whenever lattice contributions are visible in the reflectivity. Both the damped oscillation and the exponential background have been extracted and are also plotted in Fig. 4.16.

---

<sup>38</sup> This is discussed for Co<sub>2</sub>MnGe in more detail.

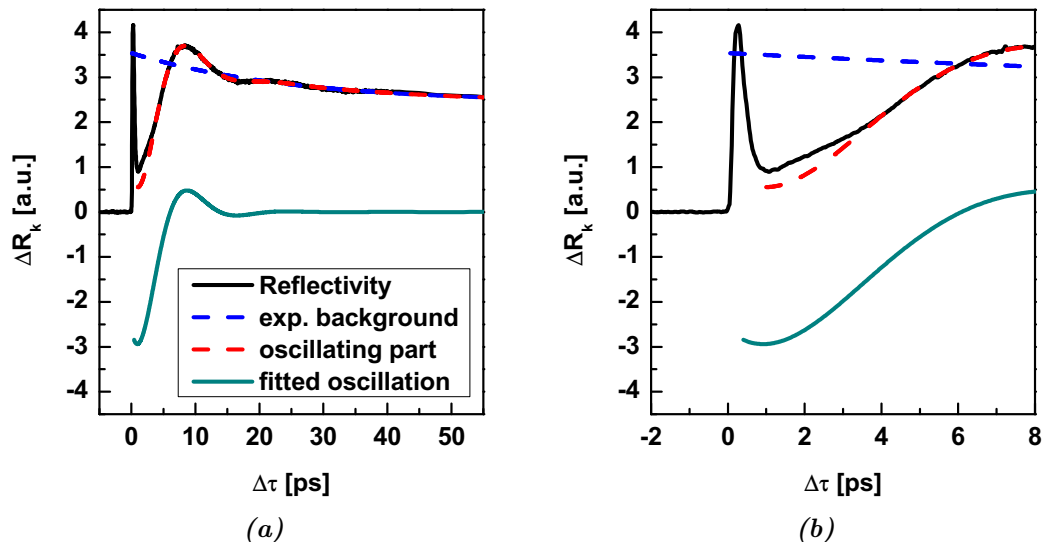


**Figure 4.16.:** Induced stress wave in the reflectivity signal of CoFeGe (sample with 25% Ge, on MgO(100)): Reflectivity signal with stress wave and fit on (a) long and (b) short timescale. The stress wave is visible as an oscillation in the form of a damped sine over an exponential background.

Note that the harmonic part of the oscillation does not start until about 3 ps, which is therefore chosen as the beginning of the fit range.

The representation of the stress wave has to be completed with an initial rise expressing the elongation of the lattice prior to the start of the oscillation. While the generic choice would be an exponential behavior, this is not necessarily the case here, due to the fact that directly after excitation the reflectivity does not reflect the behavior of the electron system. This is discussed, for example, by Hohlfeld [Hoh98]. It seems more appropriate to complete the stress wave by subtracting the measured reflectivity from an exponential decay with a decay time of the value  $\tau_E$  for pure CoFe (where the stress wave is *not* present) starting at the maximum of the reflectivity signal. Of course, one might criticize that investigating by this method whether the measured reflectivity of CoFeGe contains an exponential decay is circular reasoning. However, while the method does not provide a strict proof for this assumption, it is a convenient tool to cross-check the results from the demagnetization fits. The reconstructed stress wave obtained by this method is included in Fig. 4.17. It is no longer a strictly smooth function (in a sense of well-defined, low-valued second derivatives), containing a small irregularity at the point where the two parts of the function are matched together. However, it can

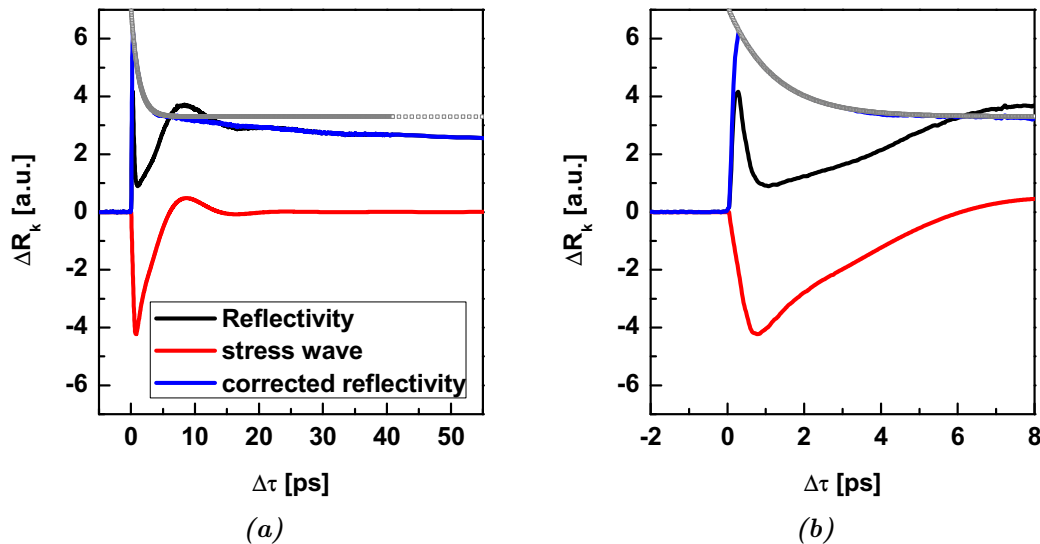


**Figure 4.17.:** Suggested correction of the induced stress wave in the reflectivity signal of CoFeGe (sample with 25% Ge, on MgO(100)): Reflectivity signal with stress wave and correction on (a) long and (b) short timescale. The gray squares represent a relaxation with the value of  $\tau_E$  for CoFe. Note that the oscillation is almost completely removed by the correction.

be used to correct the reflectivity signal very well, eliminating the oscillation also completely and resulting in a reflectivity curve reminiscent of the results for, e.g., Co<sub>2</sub>FeAl (cf. Fig. 4.7(b)). This demonstrates that the value of  $\tau_E$  for CoFe is reconcilable with the value for CoFeGe.

All in all, while several interesting observations on the measurements on CoFeGe can be made, further research is necessary to verify the trends observed. The effect of varying the Ge concentration is in accordance with XRD investigations on CoFeGe, but the effects of annealing and of using a cap layer are not yet completely clear for the case of a glass substrate. However, it has to be stressed here, that the samples under investigation did not provide a systematic alteration of these parameters, but were rather meant to investigate a large variety of effects, which complicates the evaluation. The picture will be a different one for the Co<sub>2</sub>MnGe samples discussed in the next section, where the change in parameters is limited to the substrate type and a gradual change of the Ge concentration. Even so, the pump-probe investigations proved able to identify certain effects of the CoFeGe sample properties, e.g. the trends concerning the Ge concentration or the deceptiveness of the measurements for polycrystalline samples. Also, it was possible to identify the additional measurements required to deepen the understanding of the

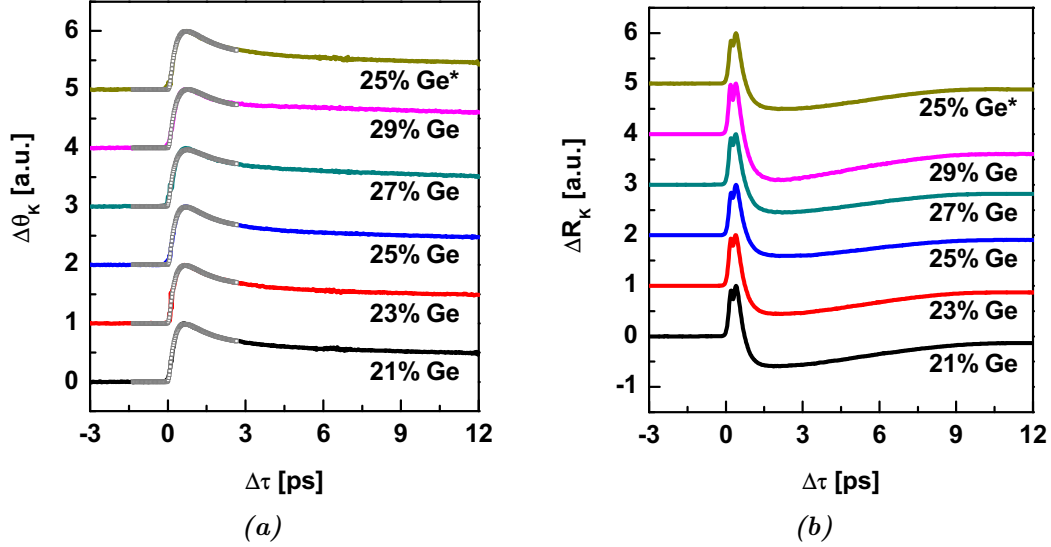


**Figure 4.18.:**  $\text{Co}_2\text{MnGe}$ , series LG0604B0X on  $\text{MgO}(100)$ : (a) Kerr rotation, (b) reflectivity. The germanium concentrations for each sample are given in the plots, where the '\*' denotes a sample with different cap layer. While the demagnetization curves show the double-exponential behavior predicted by the 3TM, the reflectivity is again marked by the overlap of electron and lattice contributions of different sign.

sample, as can be seen by reference to the discussion of the effect of the cap layer.

## 4.4. $\text{Co}_2\text{MnGe}$

In the following, the  $\text{Co}_2\text{MnGe}$  samples provided by Hitachi GST are discussed. The series LG0604B0X comprises six different compositions of  $\text{Co}_2\text{MnGe}$ . There are three subseries with equivalent compositions whereas the substrate type is chosen from  $\text{MgO}(100)$ ,  $\text{MgO}(110)$ , and polycrystalline samples on glass, respectively. The series is therefore suitable to investigate the effects of gradually altering the sample composition on the dynamics, while allowing for inferences on the effect of different substrates. In the context of this thesis, however, the aim of the investigation is to test the applicability of the pump-probe investigation to differentiating the small variations in the dynamics that are expected for the gradual variation of the sample composition. Again, only one generic measurement will be presented before the results are discussed. Also, a comparison is made between the 'simple' method of evaluation used by Müller et al. [Mül07] and the fitting of the measurement curves.

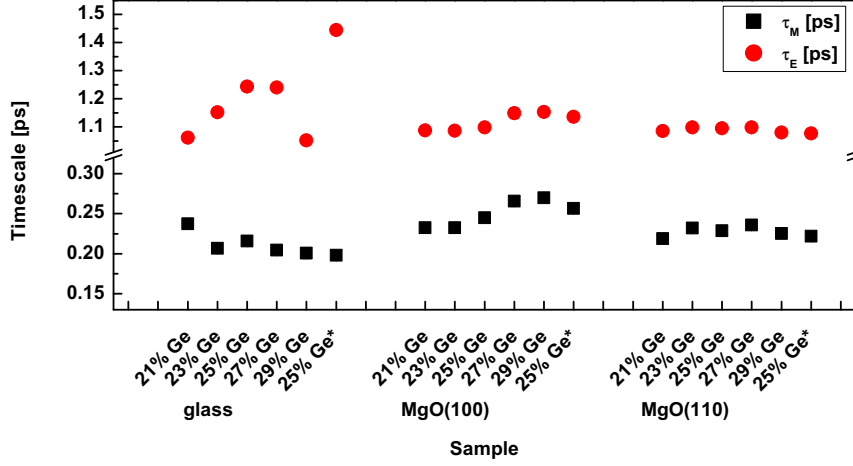


**Figure 4.19.:** Comparison of fitted timescales for  $\text{Co}_2\text{MnGe}$  samples of gradually changed composition on different substrates. The '\*' denotes a sample with different cap layer. The samples on MgO substrate show a smooth variation of the demagnetization time  $\tau_M$  with the Ge concentration and similar values of the relaxation time  $\tau_E$ , while the values for the samples on MgO scatter, especially for  $\tau_E$ .

The results for the samples on MgO(100) are shown in Fig. 4.18. The results are similar to those for the  $\text{Co}_2\text{MnSi}$  with varied annealing temperature (cf. Fig. 4.4). The demagnetization curves are in good qualitative agreement with the theory of the 3TM (cf. Fig. 3.9), whereas the reflectivity again shows an overlying lattice contribution. The latter has therefore not been used for the fit of the demagnetization (represented as gray squares). Again, the measurement signal is of higher quality for the samples on MgO than for the polycrystalline ones on glass (not shown here).

At first glance the demagnetization curves for different concentrations look mostly identical. Nevertheless, the fit of the curves reveals clear trends in the demagnetization. The result of the fits is shown in Fig. 4.19. First of all, the measurements for the samples on MgO(100) and (110) show similar trends with a smooth variation of  $\tau_M$  with the Ge concentration. All values of  $\tau_E$  are very similar for the samples on MgO substrates. The latter point can be seen as a sign of quality of the fits, because the relaxation time should not scatter more than the demagnetization time. This is, however, the case for the samples on glass, where the value for  $\tau_M$  is clearly larger for 21% Ge than for the rest, and the values for  $\tau_E$  scatter strongly. This result is in accordance with the observation that the measurements for the samples on glass are of lower quality. Apart from lower

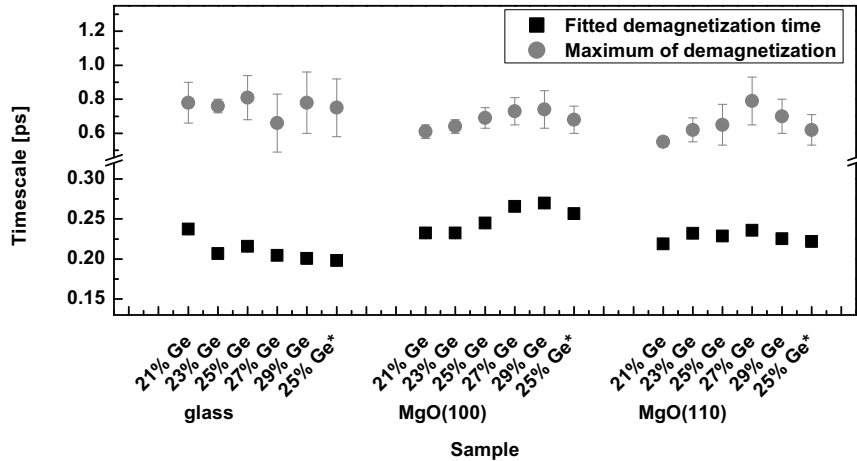


**Figure 4.20.:** Comparison of evaluation methods for the  $\text{Co}_2\text{MnGe}$  samples. The '\*' denotes a sample with different cap layer.

structural quality of these polycrystalline samples one possible reason is the heat accumulation in the sample, because the thermal conductivity of glass is about 25 times lower than that of MgO.<sup>39</sup> All in all, the pump-probe technique proves itself able to provide the resolution necessary to identify the effect of the gradual change in germanium concentration used in the samples. The highest values of  $\tau_M$  are reached for Ge concentrations of 29% and 27% respectively. As in the case of  $\text{CoFeGe}$  (cf. Fig. 4.15), the (100) orientation of the MgO substrate is preferable to the (110) orientation, yielding higher maximum polarizations. Since for the (100) direction of the MgO substrate the demagnetization time increases monotonously with the Ge content of the sample, samples of concentrations above 30% should also be checked for a possibly even higher  $P$ .

The last point of the evaluation of the data for  $\text{Co}_2\text{MnGe}$  is the comparison of the two evaluation methods available. This series of a Heusler compound with gradually changed composition is well-suited to expose the difference in the applicability of the two methods. Figure 4.20 confronts the results for the evaluation of the measurements on  $\text{Co}_2\text{MnGe}$  obtained according to the two evaluation methods. Note the larger error bars for the determination of the maximum of the demagnetization. Large errors are inherent in this method. In accordance with the lower quality of the measurements on the samples on glass, the errors are largest for these samples. Comparing the results of the two methods, it is apparent that

<sup>39</sup> Values for glass can be calculated following the method of Choudhary and Potter [CP05], while for MgO precise measurements have been performed [SFP98].

in parts the maximum values of the demagnetization show different trends than the fitted values of  $\tau_M$ . While the general trend for the samples on MgO(100) is preserved, in the case of MgO(110) it is more pronounced for the maxima than for the fitted  $\tau_M$ , and completely ambiguous for the polycrystalline samples on glass. Next, the relative values between the subseries on different substrates show a different behavior for the two methods. The result of the fit orders the sample quality as a function of the substrate type, with the MgO(100) substrate having the best order (slowest demagnetization), followed by the MgO(110) substrate. The glass substrate lies clearly beyond this, with one exception for the trend-breaking sample of lowest germanium concentration. The results of the 'simple' evaluation method differ from this even qualitatively. The values obtained for the glass samples are (on average) slightly higher than those for the MgO samples, corresponding to the already mentioned thermal effects for these samples, which displace the maximum of the demagnetization. In addition, the difference between the MgO(100) and MgO(110) samples is not apparent, since the average values for these two subseries are about the same.

All in all, the results for the more elaborate method of fitting the demagnetization curves are clearly better, for they identify the different behavior of the substrates and are more suited to resolve the differences in dynamics for the samples of different concentrations. For the method of determining the maximum of demagnetization, the trends are not clearly pronounced. Furthermore, this method is more prone to thermal effects adulterating the results, as can be seen by the example of the measurements on the polycrystalline samples. The main reason is that the position of the maximum is determined not only by the demagnetization time  $\tau_M$ , but also by the relaxation time  $\tau_E$ . For example, a very small  $\tau_E$  will shift the maximum to smaller delay times. The fit of the demagnetization is able to separate the effects of  $\tau_M$  and  $\tau_E$ , especially when  $\tau_E$  can be determined separately. Therefore, the fit should be the choice for the systematic investigation of a sample series with a varied parameter.

## 4.5. CoMnSb

The last sample under investigation is of the half Heusler compound CoMnSb. This compound is of interest because it contains the fourth period element antimony as the third component, whereas for the other compounds investigated the third components are of the second (Al, Si) or third (Ge) period. Due to

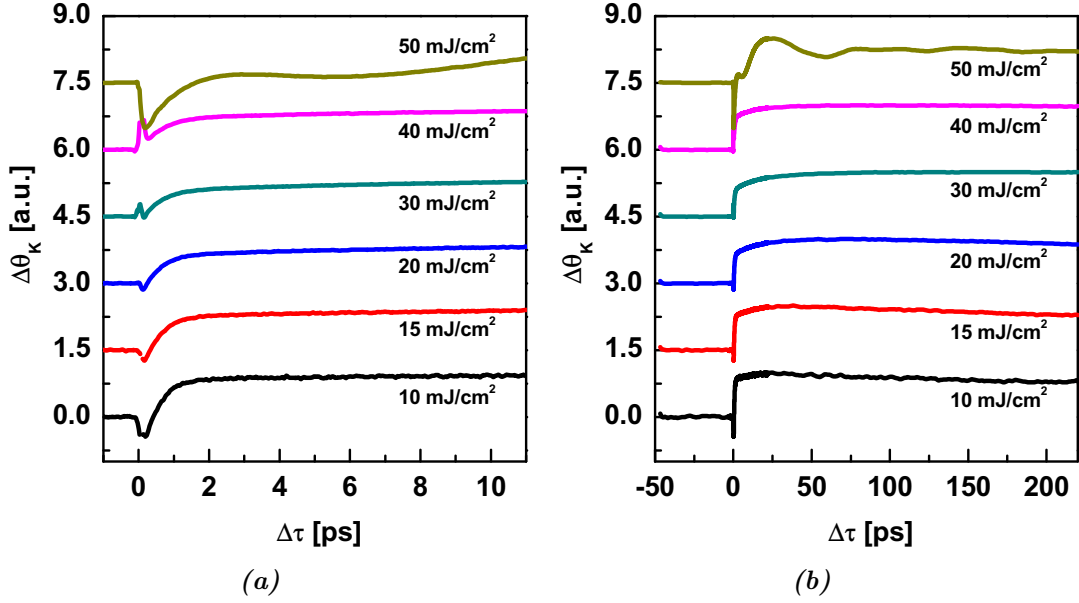


**Figure 4.21.:** Fluence-dependent investigation of CoMnSb: Kerr rotation on (a) very short timescale and (b) long timescale. A step-like feature inherent to half-metallic behavior is visible, but it occurs on a timescale of 1 ps in contrast to the expected 100 fs. Note that the demagnetization measurement for the highest fluence ( $F = 50 \text{ mJ/cm}^2$ ) is equivalent to the corresponding reflectivity measurement (see Fig. 4.23(a)), indicating sample damage.

the enlarged spin-orbit coupling  $\xi$  for heavier elements,<sup>40</sup> it is expected that this sample shows effects which are slightly different from the other samples, especially concerning the relation between  $\tau_M$  and  $P$  (see Fig. 3.7). This is also of interest because CoMnSb is predicted to have a very high spin polarization  $P$  of about 99%, and it is discussed whether this is disturbed by the spin-orbit coupling. Also, this compound exhibits a Curie temperature  $T_C$  of only 474 K [LLH<sup>+</sup>06] and is therefore suited to shed light on the impact of (too) strong thermal heating on the measurement results.

The demagnetization measurements on the CoMnSb sample for fluences between 10 and 50 mJ/cm<sup>2</sup> are shown in Fig. 4.21. At first glance it seems that the CoMnSb sample indeed has a high spin polarization, because the demagnetization curves show a step-like rise during the first picosecond followed by a slow demagnetization with a maximum value at delay times  $\Delta\tau$  between 20 and 200 ps. As will become clear later on, it is important that the step is about ten times longer than would be expected from the lifetime of non-thermal electrons. The demagnetization obviously slows down for higher values of fluence up to 40 mJ/cm<sup>2</sup>. For

<sup>40</sup> Remember that  $\xi \sim Z^2$ , where  $Z$  denotes the atomic number of the element.

the highest fluence ( $F = 50 \text{ mJ/cm}^2$ ) the demagnetization signal is completely identical to the corresponding reflectivity signal (see Fig. 4.23(a)). Since the sample is not completely demagnetized even at this high fluence (as it is not expected considering that it has a thickness of  $d = 100 \text{ nm}$ ), this fact indicates the destruction of the sample at the spot of the measurement. This is in contrast to the other films studied in this thesis, where sample damage does not occur even at highest fluences.

The aims of the investigation of CoMnSb include the study of the effect of altering the fluence on the results obtained by the pump-probe measurements. This is of importance, because normally one would want to measure at a preferably high fluence in order to obtain a clear signal. It can be seen from Fig. 4.21(b) that for the lowest two fluences the noise level is higher than for the higher ones. On the other hand, the sample is strongly heated for high fluences, which is unfavorable because it can lead to a thermally induced slowing down of the demagnetization which fakes half-metallic behavior. This is of special concern for the Heusler compound CoMnSb, since as mentioned its Curie temperature is rather low ( $T_C = 474 \text{ K}$ ).

Figure 4.22 shows the results of the fluence-dependent measurements on CoMnSb. For comparison, both the fitted demagnetization time  $\tau_M$  and the delay time of the maximum of the demagnetization are given. Since the CoMnSb sample obviously exhibits a slowing down of the demagnetization, the fit was performed according to Eq. (A.18), which describes the magnetization dynamics in the case of high spin polarizations  $P$ .<sup>41</sup> Of course, no value can be given for the highest fluence. There is a clear trend visible insofar as the obtained demagnetization time rises with the fluence up to a value of  $F = 30 \text{ mJ/cm}^2$  and drops again for the value of  $40 \text{ mJ/cm}^2$ . This is largely in accordance to the observations made in Fig. 4.21(b). Also, the two methods basically yield the same trend. The only difference is that the fit resolves a dif-

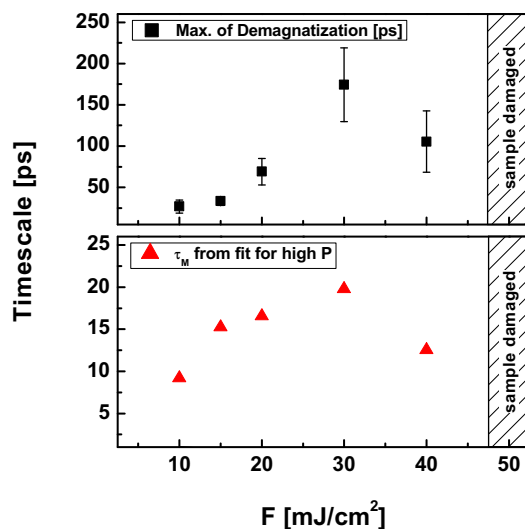


**Figure 4.22.:** Comparison of evaluation methods for CoMnSb.

<sup>41</sup> See chapter A.3 in the appendix for the derivation of the formula.

ference between the lowest two fluences. While the results might seem as if the dependence of the results on the fluence chosen is extreme, it has to be stressed here that the case of CoMnSb is special because this compound has such a low Curie temperature of  $T_C = 474$  K, which is less than 200 K above room temperature. The other Heusler compounds investigated have much higher values of  $T_C$ , typically around 1000 K. Since this is equivalent to a distance from room temperature which is more than three times higher than for CoMnSb, the chosen fluence of  $F = 30$  mJ/cm<sup>2</sup> is a reasonable choice for the investigations performed. While sometimes thermal effects can be intuited in the measurements on the other compounds, their impact on the obtained demagnetization times  $\tau_M$  can be deemed mostly harmless.

Nevertheless, the low Curie temperature of CoMnSb leads to difficulties in interpreting the observed values of the demagnetization time. The slow demagnetization on the range of 10 ps could normally be interpreted as a clear sign for a high polarization, in accordance with the value of 99% calculated by Galanakis and Mavropoulos [GM07]. The strong fluence dependence, however, indicates that apart from the blocking of the Elliot-Yafet spin-flip scattering discussed in the context of the 3TM there are different mechanisms at work that slow down the demagnetization. This is supported by the fact that the first step of the demagnetization takes rather long, namely about 1 ps. This is shown for the example of the lowest fluence in Fig. 4.21(a). The step-like feature of the X3TM, which should be very pronounced for high polarizations  $P$ , takes place on the much shorter thermalization times of the hot electrons, about 100 fs. Therefore, it has to be ruled out that the observed slowing down of the demagnetization is a direct indication for a high value of  $P$ .

An explanation for the observed scenario has recently been given by Koopmans et al. [KMDL<sup>+</sup>09] using a microscopic version of the three temperature model (M3TM). In this model, the efficiency of the demagnetization is described by a parameter  $R$  which is dependent on the *spin-flip probability*  $a_{sf}$ , the Curie temperature, and the *atomic magnetic moment*  $\mu_{at}$ ,

$$R \sim a_{sf} T_C^2 / \mu_{at},$$

and has the dimension of a frequency. For material of low  $R$ , the demagnetization is slower than the equilibration of electrons and lattice, which is given by the relaxation time  $\tau_E$ . This leads to the so-called 'type II dynamics': Since the demagnetization is more efficient when the electron temperature  $T_e$  is still high and lower as soon as electrons and lattice are in equilibrium, the demagnetization

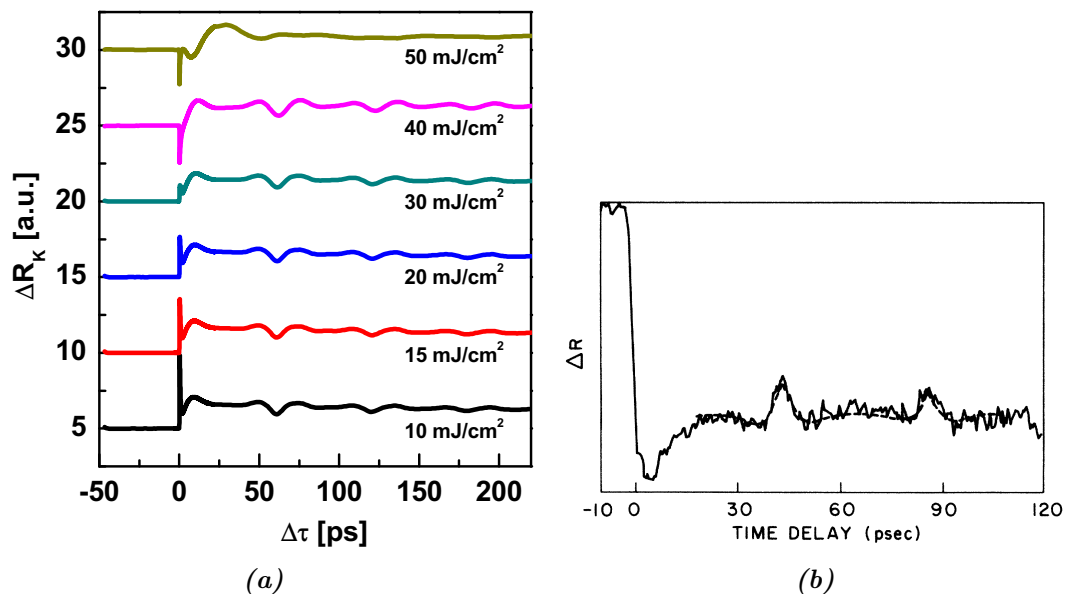


**Figure 4.23.:** (a) Stress pulse in the reflectivity of the half Heusler CoMnSb. (b) Acoustic echo in Ni as measured by Thomsen et al. [TGMT86].

will show a two-step behavior beginning with fast demagnetization and changing to slower demagnetization at a time of approximately  $\tau_E \sim 1$  ps, as observed in Fig. 4.21(a). The fluence dependence of the demagnetization time  $\tau_M$  is explained by fluctuations of the magnetization arising when  $T_s$  approaches  $T_C$ . Note that the model by Koopmans et al. does *not* include non-thermal electrons, but assumes the electrons to be in equilibrium at all times.

It has to be concluded that the dynamics measured for CoMnSb can be explained by the M3TM and are not an evidence of a high polarization  $P$ . On the other hand, the measurements do not falsify the prediction of a high  $P$ . Since the M3TM neglects the influence of the polarization (and the non-thermal electrons), its applicability to the case of CoMnSb does not provide any statements concerning  $P$ . Here, a microscopic model that uses the Landau-Lifshitz-Bloch equation (cf. chapter 2.1) and includes the polarization would be of help in determining the spin polarization correctly.

A very interesting behavior is found for the reflectivity of CoMnSb, depicted in Fig. 4.23(a): The signal shows a periodic, but clearly non-harmonic oscillation with a period of roughly 50 ps. This signal is caused by the *acoustic echo* of a stress pulse, i.e. basically a coherent longitudinal phonon, which travels through the film and is reflected at its backside. The period of the oscillation is equal to the traveling time of the stress pulse through the film, and it can also be observed

that the damping of the pulse is rather low. The observed signal is similar to the observations made by Thomsen et al. for thin films of nickel and  $\alpha$ -arsenic telluride ( $\text{As}_2\text{Te}_3$ ) [TGMT86]. The result of their reflectivity measurement on a 120 nm Ni film is shown in Fig. 4.23(b). Note that the form of the actual stress wave is completely congruent with the one observed for the reflectivity of CoMnSb.

## 4.6. Comparison of results and X3TM

Having finished the discussion of the single measurements, it is now time to derive a uniform picture from the data. This section will address one of the main topics of this thesis, namely the refinement of the method proposed by Müller et al. presented in chapter 3.3 to determine the spin polarization  $P$  from the experimental values of the demagnetization time  $\tau_M$ . Therefore, in the first part of this chapter, the fitted demagnetization times  $\tau_M$  extracted from the measurements on the Heusler compounds will be used to create a new  $\tau_M$  vs.  $P$ -plot suitable to determine the polarization for samples from the fit of  $\tau_M$  in future measurements. In addition, it is shown that the proposed expansion of the 3TM (also introduced in chapter 3.3) is able to naturally explain the spectrum of different demagnetization curves obtained from samples of highly different polarizations  $P$ .

Figure 4.24 shows measurements from Müller et al. [Mül07] on samples of different polarizations  $P$ .<sup>42</sup> Here, it is again obvious that the dynamics of the samples, in particular the timescale  $\tau_M$ , are greatly affected by the difference in polarization. Remember that this is predicted by the 3TM if one regards the fact that a high value of  $P$  blocks the direct channel of energy transfer between electrons and spins (cf. Fig 3.9). In Fig. 4.24, all curves have been fitted using the solution of the normal 3TM for the samples with  $\tau_M < 1$  ps (Fig. 4.24(a)) and with the solution for the case of high  $P$  (Fig. 4.24(b)), respectively. It has to be stressed again that Müller et al. used the position of the maximum of the demagnetization as the value for  $\tau_M$ , in contrast to the fit of the analytical solution used in the course of this thesis.

The data from Fig. 4.24, along with the demagnetization data collected in the course of this thesis, can now be used to install a new  $\tau_M$  vs.  $P$ -plot that is suitable to determine the polarization of a sample from the values of  $\tau_M$  received from the fit of the 3TM to the demagnetization curves. The  $\tau_M$  vs.  $P$ -plot from Müller et al. is redisplayed in Fig. 4.25(a).<sup>43</sup> The variation of this plot designed

---

<sup>42</sup> The curve for  $\text{Co}_2\text{MnSi}$  has been replaced by data for CMS15 from Fig. 4.1

<sup>43</sup> Details of this plot are given in the reference.

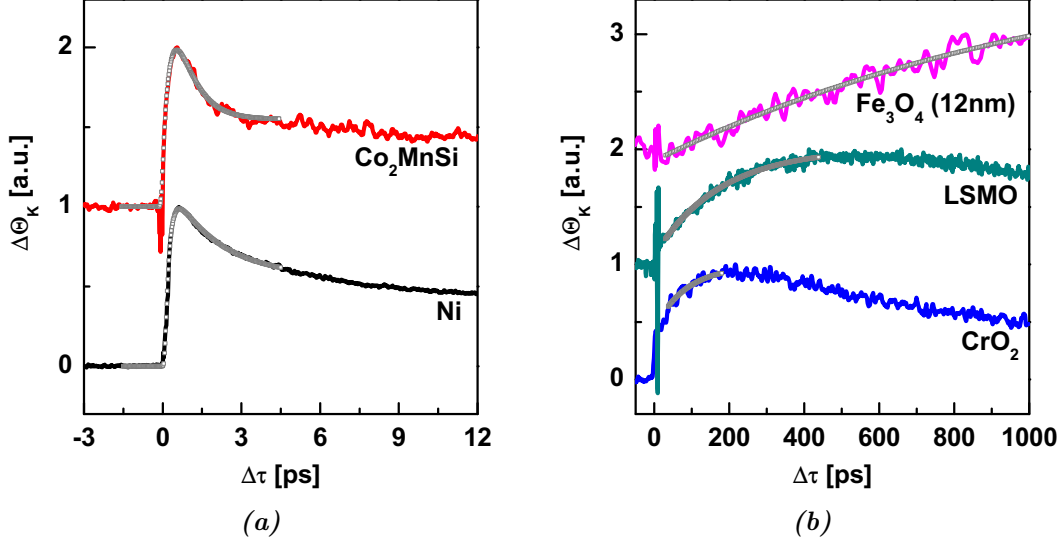


**Figure 4.24.:** Demagnetization of samples with different polarization: Examples for (a) fast demagnetization and (b) slow demagnetization. This plot shows how the different values of polarization  $P$  result in a spectrum of highly different demagnetization curves. All curves have been fitted to extract  $\tau_M$ , where the normal 3TM and the solution for high  $P$  have been used for cases (a) and (b), respectively. The demagnetization curves have been taken from Müller et al. [Mül07], with the exception of  $\text{Co}_2\text{MnSi}$ , where the measurement on sample CMS15 from Fig. 4.1 has been inserted.

for the fitted values of  $\tau_M$  is shown in Fig. 4.25(b). In the latter plot, data points using fixed values of  $P$  that have been determined separately are marked by circles, with gray circles denoting measurements from Müller et al. and red circles denoting recent measurements. The black squares represent points for which  $P$  has been determined from  $\tau_M$  using the new plot. The new measurements used include the  $\text{Co}_2\text{MnSi}$  samples of 15 nm thickness on Si and MgO,  $\text{Co}_2\text{MnGe}$ (29%) on MgO(100),  $\text{CoFeGe}$ (28%) and  $\text{CoFe}$  on MgO(100) and (110) (averaged for each material),  $\text{Co}_2\text{FeAl}$  annealed at 500° C, and  $\text{CoMnSb}$  measured at a fluence  $F = 30 \text{ mJ/cm}^2$ . In both plots, the solid lines model materials of opposing extreme values of anisotropy energies, namely  $4 \mu\text{eV}$  and  $1000 \mu\text{eV}$ . For the position of these lines, the determining parameter in the range of low  $P$  is actually the value  $\tau_{el,0}/c^2$  from Eq. (3.13), which corresponds to the intercept of the two lines with the  $\tau_M$ -axis. It is important to note that the plot of Fig. 4.25(a) was created to fit the data points of lowest  $P$ , namely Gd, Ni, Fe, Co, and Py, because due to the inverse proportionality to  $(1 - P)$ ,  $\tau_M$  is much more sensitive to changes of  $P$  for low polarizations. To account for this difference in accuracy, for the creation of

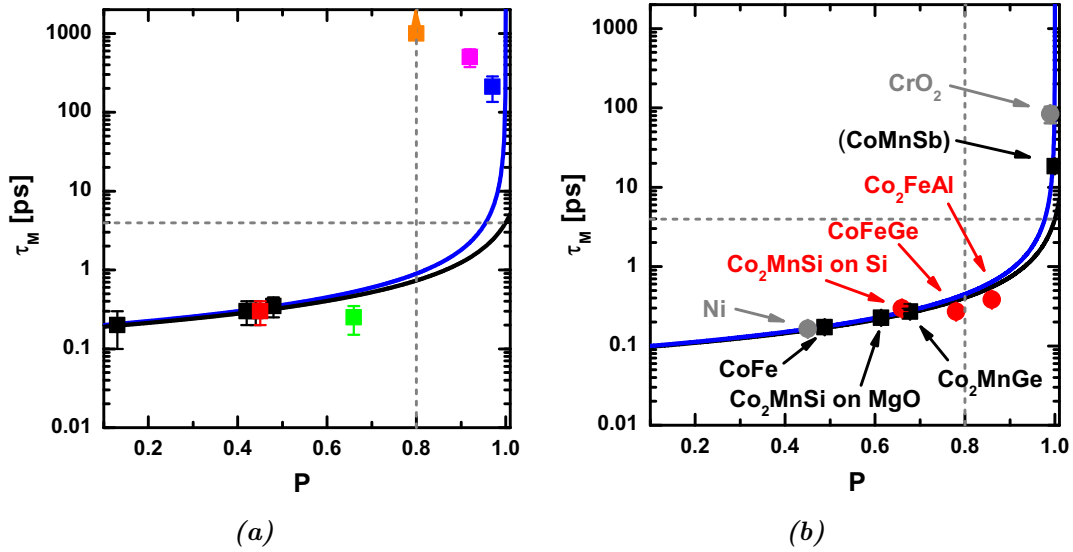


**Figure 4.25.:** Relation between demagnetization time  $\tau_M$  and polarization  $P$ : (a) plot from Müller et al., using the time of the maximum of demagnetization as  $\tau_M$  [MWD<sup>+</sup>09], (b) new plot using the fitted value of  $\tau_M$ . In (b), circles mark materials where the polarization has been determined independently, whereas squares mark data where  $P$  has been determined from  $\tau_M$ . In addition, for gray points the demagnetization curves were taken from Müller et al., while for red and black points the curves have been measured in the context of this thesis. Sample details are included in the text. The gray lines mark the value of 80% for  $P$ , above which a material is counted as half-metallic. For a value of  $\tau_M$  higher than 4 ps (horizontal lines), the Elliot-Yafet scattering is completely blocked. Note that the large value of  $\tau_M$  for  $\text{CoMnSb}$  would normally indicate a very high  $P$  of virtually 100%. However, this can not be concluded from the measurements as has been discussed in chapter 4.5.

Fig. 4.25(b) the  $\tau_M(P=0)$ -value was adjusted to match all the data points given by circles, but the point for Ni was considered to be of highest importance. The new plot is in this form suited for the evaluation of the fit results, as can be seen from the fact the first data evaluated according to it (given by the black squares) reflect the trends noted in the sections above and assume realistic values. The horizontal gray lines in Fig. 4.25 indicate the value of 80% for  $P$ , which according to Müller et al. is the critical value above which a material is half-metallic. The horizontal gray lines mark the values of  $\tau_M = 4$  ps where due to high polarization the Elliot-Yafet scattering is completely blocked [MWD<sup>+</sup>09].

A final statement has to be made concerning the result for  $\text{CoMnSb}$  included in Fig. 4.25(b). The large value of  $\tau_M$  for  $\text{CoMnSb}$  would normally indicate a very high  $P$  of virtually 100%. However, it is important to remember that this can *not* be concluded from the measurements since the dynamics of  $\text{CoMnSb}$  is slowed down due to its low Curie temperature, as has been discussed in chapter 4.5.

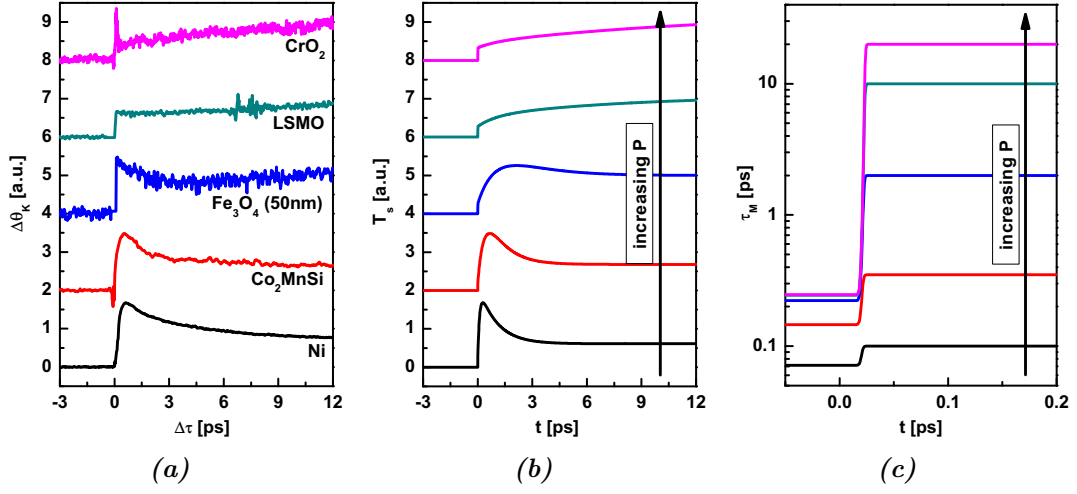


**Figure 4.26.:** Comparison of experimental data to expanded 3TM: (a) demagnetization data from Fig. 4.24 with data for a different  $\text{Fe}_3\text{O}_4$  sample [MWD<sup>+</sup>09], (b) numerical solution of the expanded 3TM, (c) timely evolution of demagnetization time  $\tau_M$  used in the simulation (on logarithmic scale). The data in (a) are ordered according to their spin polarization, as is the case for the simulated curves in (b). For the experimental curves of  $\text{Fe}_3\text{O}_4$  and LSMO, data points around  $\Delta\tau = 0$  showing remnants of the autocorrelation artifact (cf. chapter B.2) have been removed.

With these remarks the implementation of the new method for evaluating the pump-probe data applying a fit of the 3TM is thereby completed.

The culmination of the analysis of the experimental data is the combination of the relation between polarization  $P$  and demagnetization time  $\tau_M$  on the one hand and the results of the expanded three temperature model on the other hand. Here, it will become obvious that the impact of the X3TM is not limited to the modeling of the step-like feature observed in several of the measurements (cf. e.g. Fig. 4.6 for  $\text{Co}_2\text{MnSi}$ ). The expanded model is rather able to explain the existence of the wide spectrum of demagnetization times collected in the  $\tau_M$  vs.  $P$ -plot in a natural way.

The following remarks provide a continuation of the studies by Müller et al [Mül07]. The data used in this reference to illustrate the significantly different behavior for materials of different polarizations is displayed again in Fig. 4.26(a). In the plot presented here, data for a different  $\text{Fe}_3\text{O}_4$  sample taken from the same work was used [MWD<sup>+</sup>09]. Also, for  $\text{Fe}_3\text{O}_4$  and LSMO data points around  $\Delta\tau = 0$  showing remnants of the autocorrelation artifact (cf. chapter B.2) have been removed for clarity, but are included in the original work. Figure 4.26(b) shows the result of the numerical solution of the X3TM for different values of  $\tau_{es,2}$  (cf. Eq. (3.17)). The temporal evolution of the resulting  $\tau_M$ 's are displayed in

Fig. 4.26(c). Here, it is important to remark that the characteristic timescale  $\tau_{es,2}$  is the *only* parameter varied in the simulations.<sup>44</sup> As stated in chapter 3.3, it reflects the time-independent energy transfer channel mediated by Elliot-Yafet type spin-flip scattering, and thus its variation models cases of different polarization  $P$ . Comparing Figs. 4.26(a) and (b), it becomes apparent that the simulation results are stunningly congruent with the experimental data. The complete spectrum of different demagnetization curves is qualitatively reproduced by the expanded three temperature model. Of course, there are some minor discrepancies, e.g. for the relaxation of Ni and the imperfect behavior of  $\text{Fe}_3\text{O}_4$ . This is, however, not surprising, given the fact that in the simulation only one parameter is varied, whereas the samples in Fig. 4.26 differ in a number of parameters. In particular, the same model is used to describe metallic and oxidic materials, which is definitely a strong simplification.

Lastly, it is time to sum up the statements and observations on the X3TM made in various parts of this thesis. The successful demonstration of the application of the X3TM in explaining the dependence of  $\tau_M$  on  $P$  is also a justification for the assumption that the non-thermal electrons play a decisive role in the underlying physics. While the mechanism of the time-dependent  $\tau_{es}$  might have seemed like nothing more than an educated guess upon its introduction in chapter 3.3, there is now clear evidence that such a mechanism makes correct predictions with respect to the demagnetization. However, the treatise provided in this section is far from being a strict proof for the proposed role of the non-thermal electrons and the connection of the step-like feature to the spin-flip energy  $\Delta_{sf}$ . It is no wonder that the step-like feature in the dynamics can be described by introducing (at least) two additional parameters of the X3TM into the conventional 3TM. Nevertheless, there is strong evidence that the assumptions of the X3TM are correct. This is because on the one hand, they are based on the physics of the electron system, which is directly involved in the laser excitation process, and on the other hand, because the timescale of the step-like feature matches the lifetime of the non-thermal electrons. Frankly, the 'smoking gun' experiment verifying the X3TM mechanism is as yet missing. Here, it is only possible to propose a number of future investigations on the topic:

1. The present femtosecond pump-probe investigations are unfit to give a clear impression of the dynamics on timescales of the lifetime of non-thermal electrons of about 100 fs. More insight can be gained by using short enough pulses, which most probably requires a laser system with a pulse length  $w$  of

---

<sup>44</sup> Of course, this changes  $\tau_M$  for both  $t < t_0$  and  $t > t_0$ , as can be seen in Fig. 4.26(c).

5 to 10 fs. Such investigations would also reveal more details of the structure of the temporary evolution of the channel between electrons and spins, which was in the context of this thesis modeled to be step-like by itself.

2. The dependence of the step-like feature on the spin-flip energy  $\Delta_{sf}$  was derived from the simple picture of the spin-resolved density of states. This picture is of adequate accuracy for the investigation and modeling performed, but it disregards, for example, the actual band structure. Therefore it is interesting to further investigate the connection between the step-like feature and  $\Delta_{sf}$ . Ideally, this is done by obtaining an estimate for  $\Delta_{sf}$  from band structure calculations and performing pump-probe experiments on a set of preferably similar samples, which differ only (but strongly) in the value of  $\Delta_{sf}$ . This should reveal the presumed dependence.
3. One of the easier methods to investigate the step-like feature is to perform pump-probe investigations for variable excitation energy (i.e., laser wavelength). The experiments with varying excitation energy should trigger qualitatively different dynamics if the values chosen are in the vicinity of  $\Delta_{sf}$ . Furthermore, this method might even be able to check the existence of the pseudogaps that are present, for example, in many of today's Heusler compounds.

These proposals conclude the comparison of the experimental data to the X3TM, and also the presentation of the performed investigations at all. However, the given proposals emphasize that the inherent physics of the processes observed is not yet fully explained and definitely a topic of future research. In particular, the new microscopic model by Koopmans et al. [KMDL<sup>+</sup>09] that was suited to explain the dynamics of CoMnSb should be integrated into the expansion of the 3TM, or an approach using the (also microscopic) Landau-Lifshitz-Bloch equation can be implemented.

# Chapter 5.

## Summary and Outlook

All-optical pump-probe experiments provide a valuable tool to investigate and understand the magnetization dynamics on the ultrafast timescale. In the course of this thesis, it was possible to demonstrate how time-resolved MOKE experiments on the femtosecond timescale provide a deepened understanding of the present models of magnetization dynamics. The investigation of materials of different degree of half-metallicity, measured in terms of the spin polarization  $P$ , has proven itself valuable in exploring the underlying physics of the femtosecond dynamics. The investigated samples from the class of Heusler compounds have been particularly useful for this purpose, because the wide variety of compositions for these alloys allow for a systematic altering of sample characteristics over a wide parameter range.

It has to be pointed out that the concept of half-metallicity as introduced in chapter 2.3 is a very fundamental and comprehensible one, yet it gives access to rich physics in the pump-probe investigations. Also, the quadratic MOKE that has been treated in chapter 2.4 is relevant to the understanding of the dynamics in materials that exhibit QMOKE. Chapter 3.2 introduced the phenomenological two- and three temperature models used to explain the magnetization dynamics on the femtosecond timescale. For the three temperature model (3TM) the expansion by Müller et al. [MWD<sup>+</sup>09] connecting the polarization of the magnetic material to its characteristic timescale  $\tau_M$  of the demagnetization has been presented in chapter 3.3. There, an additionally expanded three temperature model (X3TM) has been proposed that explains the step-like feature of demagnetization appearing on the range of 100 fs via non-thermal electrons. Also, the role of the spin specific heat  $C_s$  that has up to now been neglected in the 3TM has been discussed in chapter 3.4, and an estimate of the error made by neglecting  $C_s$  has been given.

The evaluation of the measurements on Heusler compounds in chapter 4 has been performed on multiple levels. In the direct evaluation of the Heusler samples the demagnetization behavior of various compounds has been investigated with the

---

aim of determining the connection between the composition and structural quality of the Heusler films and their characteristic demagnetization time  $\tau_M$ . Here, two details shall be pointed out: For the investigation of  $\text{Co}_2\text{FeAl}$  in chapter 4.2 it has been proven that  $\tau_M$  (and thus the polarization  $P$ ) scales with the structural quality of the film determined from XRD measurements. The measurements on  $\text{Co}_2\text{MnGe}$  in chapter 4.4 provide an investigation where a single parameter, the Ge concentration, is varied over a range of almost ten percent, while identical samples on different types of substrates have been used. This has been proven useful to identify the effect of the Ge concentration and the substrate type on the spin polarization. Along with the basic investigations of the Heusler samples, several effects occurring in the samples have been identified. Examples are the quadratic MOKE in  $\text{Co}_2\text{FeAl}$  (chapter 4.2) and the thermally induced stressed wave in  $\text{CoFeGe}$  (chapter 4.3). While such effects can be considered as impeding the evaluation, they often contain rich physics by themselves. This is especially true for the dynamic QMOKE, which is up to now uncharted territory.

On a wider scope, two things are important in the evaluation. First, the measurements on the Heusler compounds provide examples of materials with an intermediate range of polarizations  $P$ . They fill up the gap between ferromagnets like Ni and Fe with low polarizations of 40 to 50% on the one hand and high- $P$  oxides like LSMO and  $\text{CrO}_2$  on the other side. The complemented plot of  $\tau_M$  vs.  $P$  has been modified in chapter 4.6 to allow for the usage of values of  $\tau_M$  obtained from the fit of the 3TM to the experimental data. As has been discussed in the evaluation of  $\text{Co}_2\text{MnGe}$  (chapter 4.4), this process is preferable to the previous method using the position of the maximum of the demagnetization, because it is able to separate effects of demagnetization and relaxation. The new  $\tau_M$  vs.  $P$ -plot can be used to directly determine the polarization of a sample from the fit of the demagnetization measurements. The second point of the advanced evaluation is the validation of the expanded 3TM. As discussed in chapter 4.6, the X3TM explains the variety of different dynamics exhibited by samples of varied polarization  $P$  at ease. The X3TM successfully regards the non-thermal electrons to explain the different observed dynamics and the step-like feature accompanying it.

During the evaluation, several proposals for expansions of the work presented in this thesis have already been made. As it has been pointed out in the discussion of the results for  $\text{Co}_2\text{MnGe}$ , the all-optical pump-probe technique can be used for systematic studies of samples with varied composition. To obtain clearer trends, the composition should be altered over an even wider range than for the used  $\text{Co}_2\text{MnGe}$  samples. A main issue of future experiments is a further validation of

the expansion of the 3TM. While the successful application of the X3TM strongly hints at the correctness of the assumptions of the expansion, a real proof has yet to be provided. Therefore, several experiments advancing the investigation of the X3TM have been made in chapter 4.6. Also, the example of the measurements on CoMnSb in chapter 4.5 show that the evaluation of demagnetization data can be quite intriguing. The timescale on which the step-like feature occurs for CoMnSb can be used to easily identify that the observed slowing down of the dynamics is not caused by a high polarization, but is rather explained by the microscopic three temperature model (M3TM) of Koopmans et al. [KMDL<sup>+</sup>09]. However, since this model does not directly regard the polarization, a complete description is as of now lacking. It has been proposed that an approach based on the microscopic modeling of the Landau-Lifshitz-Bloch equation [ACFK<sup>+</sup>07] would provide more insight here. The final conclusion is that beyond the insight gained in this thesis, the field of femtosecond magnetization dynamics still provides unexplained physics and will continue to intrigue researchers interested in a detailed description of the fundamental physics of magnetization processes.

# Appendix A.

## Explicit calculations

### A.1. Analytical solution of the 2TM

We explicitly demonstrate how to obtain an analytical solution of the 2TM, because we will need this solution for the 3TM. We will assume homogeneous heating of the sample and neglect heat diffusion. We start with the reproduction of Eqs. (3.5):

$$\begin{aligned} C_e \cdot \frac{dT_e}{dt} &= g_{el-lat} \cdot (T_l - T_e) + P(t) \\ C_l \cdot \frac{dT_l}{dt} &= g_{el-lat} \cdot (T_e - T_l) \end{aligned} \tag{A.1}$$

To simplify the calculations we further assume the source term to be a  $\delta$ -function,

$$P(t) = P_0 \cdot \delta(t),$$

which means the pulse arrives at  $t = 0$  and instantly deposits its energy. We can obtain solutions for other shapes of the source term later on by convolution with the result [Dal08]. In the following we will use the lower integration boundary  $t_{min} < 0$ , for which the system is in equilibrium. Furthermore, the specific heats shall be constant for the analytical solutions. To be precise we would have to write  $\Delta T_i$  to express that we calculate temperature changes, but we omit the  $\Delta$  for convenience. Adding Eqs. (A.1) and using  $T_e(t_{min}) = T_l(t_{min}) = 0$  we deduce

$$\begin{aligned} \int_{t_{min}}^t \left( C_e \cdot \frac{dT_e}{dt} + C_l \cdot \frac{dT_l}{dt} \right) dt &= (C_e T_e + C_l T_l)(t) = \int_{t_{min}}^t P(t) dt = P_0 \cdot \theta(t) \\ \Rightarrow \Delta &:= C_e T_e + C_l T_l = P_0 \cdot \theta(t) \end{aligned}$$

## Appendix A. Explicit calculations

---

The quantity  $\Delta$  we introduced is in fact a function of time, but its behavior for a  $\delta$ -like source term is rather trivial. Note that  $\Delta$  in general measures the amount of pump fluence  $P$  absorbed by the sample. We can treat it as a constant for most of the discussion. If we express Eqs. (A.1) using  $\Delta$  we obtain

$$\begin{aligned} C_e \cdot \frac{dT_e}{dt} &= \frac{g_{el-lat}}{C_l} \cdot (\Delta - T_e \cdot (C_e + C_l)) \\ C_l \cdot \frac{dT_l}{dt} &= \frac{g_{el-lat}}{C_e} \cdot (\Delta - T_l \cdot (C_e + C_l)). \end{aligned}$$

From this we can see that the dynamics can be expressed using only one time-dependent variable  $(T_e - T_l)(t)$ . Defining  $\gamma = (C_e + C_l)/(C_e C_l)$  we obtain the equation

$$\frac{dT_e}{dt} - \frac{dT_l}{dt} = -\gamma g_{el-lat} \cdot (T_e - T_l).$$

In the resulting expressions

$$\begin{aligned} T_e - T_l &= A_0 + A_1 \cdot e^{-\gamma g_{el-lat} t} \\ C_e T_e + C_l T_l &= \Delta, \end{aligned} \tag{A.2}$$

the constant  $A_0$  can be dropped instantly because we demand  $T_e = T_l$  for  $t \rightarrow \infty$ . Furthermore, we see that the dynamics is governed by a single characteristic timescale  $\tau_E = (\gamma g_{el-lat})^{-1}$ , the *relaxation time*. While  $\tau_E$  under certain conditions governs the reflectivity signal of the sample (this is discussed in detail by Hohlfeld [Hoh98]), its general behavior is tricky to understand and we shall not discuss it here in too much detail. Our calculation so far lead us to the preliminary result

$$\begin{aligned} T_e &= \frac{A_1 C_l}{C_e + C_l} \cdot e^{-t/\tau_E} + \frac{\Delta}{C_e + C_l} \\ T_l &= -\frac{A_1 C_e}{C_e + C_l} \cdot e^{-t/\tau_E} + \frac{\Delta}{C_e + C_l}, \end{aligned} \tag{A.3}$$

into which we can now insert the boundary conditions. We already ensured that the system reaches the new equilibrium temperature  $T_1 := T_e(t \rightarrow \infty) = T_l(t \rightarrow \infty)$ . Since  $T_l(0) = 0$  we see that  $A_1 = \Delta/C_e$  is time-dependent, but only to the point that it is zero before the pulse arrives and constant afterwards. At  $t = 0$  the electron temperature reaches its maximum value  $T_{2,e}$  given by

$$T_{2,e} = \frac{\Delta}{C_e} \stackrel{t=0}{=} \frac{P_0}{C_e}.$$

This is trivial because at  $t = 0$  the complete energy of the pulse is transferred to the electron system. The new equilibrium temperature also turns out to take on the expected form

$$T_1 = \frac{P_0}{C_e + C_l}.$$

To summarize the result we express Eqs. (A.3) via the two temperatures and yield

$$\begin{aligned} T_e(t) &= \theta(t) \left[ T_1 + (T_{2,e} - T_1) \cdot e^{-t/\tau_E} \right] \\ T_l(t) &= \theta(t) \left[ T_1 \left( 1 - e^{-t/\tau_E} \right) \right], \\ \tau_E &= \left( g_{el-lat} \cdot \frac{C_e + C_l}{C_e C_l} \right)^{-1} \\ T_{2,e} &= \frac{P_0}{C_e}, \quad T_1 = \frac{C_e T_{2,e}}{C_e + C_l} = \frac{P_0}{C_e + C_l}, \quad P_0 = \frac{\alpha_{abs} F}{d} \end{aligned} \tag{A.4}$$

In order to account for realistic pulse shapes, one can simply multiply the source term with the form of the pulse as a (normalized) function of time. This is equivalent to a convolution of the result (A.4) with this shape function.<sup>45</sup> The shape function for a Gaussian pulse reads

$$G(t) = \sqrt{\frac{2}{\pi w^2}} \cdot e^{-\frac{2t^2}{w^2}} \tag{A.5}$$

Performing some algebra, one obtains

$$\begin{aligned} [T_e * G](t) &= T_1 \cdot \text{step}_0(t) + (T_{2,e} - T_1) \cdot \text{step}_E(t) \cdot e^{-\left(\frac{t}{\tau_E} - \frac{w^2}{8\tau_E^2}\right)} \\ [T_l * G](t) &= T_1 \cdot \left[ \text{step}_0(t) - \text{step}_E(t) \cdot e^{-\left(\frac{t}{\tau_E} - \frac{w^2}{8\tau_E^2}\right)} \right], \\ \text{step}_0(t) &= \frac{1}{2} \cdot \left( 1 + \text{erf} \left\{ \frac{\sqrt{2}t}{w} \right\} \right), \quad \text{step}_E(t) = \frac{1}{2} \cdot \left( 1 + \text{erf} \left\{ \frac{\sqrt{2}t}{w} - \frac{\sqrt{2}w}{4\tau_E} \right\} \right). \end{aligned} \tag{A.6}$$

Comparing (A.6) to (A.4), we see that in principle only the form of the step for the temperatures has changed from  $\theta(t)$  to a step modeled by the error function, which is somehow intuitive given the fact that  $\int G(t) \sim \text{erf}(\sqrt{2}t/w)$ .

Calculating the corresponding value for  $\Delta_G$  (now for the temperatures obtained for a Gauss pulse) reflects this, for expressing the  $T_1$  and  $T_{2,e}$  in terms of  $P_0$  we obtain

$$\Delta_G = C_e [T_e * G(t)] + C_l [T_l * G(t)] = \frac{P_0}{2} \cdot \text{erf}_1(t). \tag{A.7}$$

---

<sup>45</sup> Remember the definition of the convolution:  $[f * g](t) = \int_{-\infty}^{+\infty} du f(u) \cdot g(t - u)$ .

We can use this equation to cross-check the results of our simulations, as stated by Hohlfeld [Hoh98]. This will also be valid in the case of the 3TM where we consider the spins, too, but only up to the point where the specific heat  $C_s$  of the spins is negligible compared to the specific heats  $C_e$  and  $C_l$  of electrons and lattice.

## A.2. Analytical solution of the 3TM

We will continue the discussion by providing the analytical solution of the 3TM. Although the calculation is mostly straightforward, we want to present it here to give the reader more insight into the structure of the solution. This is important to understand the applicability of the 3TM and to sort out the cases where the modeling performed has to be handled with care.

As stated in 3.2, we start solving the 3TM by separating the equations for the electrons and the lattice, which yields the 2TM and the result (A.4) for a  $\delta$ -shaped pulse. Again, this is possible because we assume that the spin system itself does not influence the electron and lattice dynamics. We now add the equations for the spin system, which reads

$$C_s \cdot \frac{dT_s}{dt} = g_{el-sp} \cdot (T_e - T_s) + g_{lat-sp} \cdot (T_l - T_s).$$

Inserting our results for  $T_e$  and  $T_l$  from the 2TM yields

$$\begin{aligned} \frac{dT_s}{dt} &= \frac{(T_e - T_s)}{\tau_{es}} + \frac{(T_l - T_s)}{\tau_{ls}} \\ &= \theta(t) \cdot \left[ -T_s \left( \frac{1}{\tau_{es}} + \frac{1}{\tau_{ls}} \right) + \right. \\ &\quad \left. + T_1 \left( \frac{1}{\tau_{es}} + \frac{1}{\tau_{ls}} \right) \left( 1 - e^{-\frac{t}{\tau_E}} \right) + \frac{T_{2,e}}{\tau_{es}} e^{-\frac{t}{\tau_E}} \right]. \end{aligned} \quad (\text{A.8})$$

Here, we introduced the *electron-spin relaxation time*  $\tau_{es} = C_s/g_{el-sp}$  and the *lattice-spin relaxation time*  $\tau_{ls} = C_s/g_{lat-sp}$ . Note that the equation received is a linear inhomogeneous differential equation of first order, i.e. it can be written in

the form

$$\begin{aligned}
y'(t) &= a \cdot y(t) + b(t) & (A.9) \\
a &= -\left(\frac{1}{\tau_{es}} + \frac{1}{\tau_{ls}}\right), \quad y(t) = \theta(t) \cdot T_s(t), \\
b(t) &= \theta(t) \cdot \left[-\frac{T_1}{a} \left(1 - e^{-\frac{t}{\tau_E}}\right) + \frac{T_{2,e}}{\tau_{es}} e^{-\frac{t}{\tau_E}}\right].
\end{aligned}$$

A solution to equations of the form (A.10) can be obtained using the method known as variation of the constant [FK01]. As in the case of the 2TM we can leave out the Heaviside function  $\theta(t)$  for the calculation and reintroduce it afterwards. The ansatz

$$y(t) = c(t) \cdot e^{A(t)}, \quad A(t) := \int a(t) dt$$

will lead to

$$c(t) = y_0 + \int_{t_0}^t e^{-A(s)} b(s) ds.$$

As always, we first obtain the solution of the homogeneous equation,

$$\frac{dT_s}{dt} = -\left(\frac{1}{\tau_{es}} + \frac{1}{\tau_{ls}}\right) \cdot T_s \quad \Rightarrow \quad T_s(t) = c \cdot e^{-\frac{t}{\tau_M}},$$

where we introduced the *demagnetization time*

$$\tau_M = \left(\frac{1}{\tau_{es}} + \frac{1}{\tau_{ls}}\right)^{-1}. \quad (A.10)$$

Next, we will vary the constant  $c = c(t)$ . Note that  $a = -1/\tau_M$  and therefore  $A(t) = -t/\tau_M$ . Using  $T_s(t < 0) = 0$  we can omit  $y_0$  and shift the lower boundary for the integral to 0. We finally arrive at

$$\begin{aligned}
c(t) &= \frac{T_1}{\tau_M} \cdot \left[ \tau_M \left( e^{\frac{t}{\tau_M}} - 1 \right) - \left( \frac{1}{\tau_M} - \frac{1}{\tau_E} \right)^{-1} \left( e^{t \left( \frac{1}{\tau_M} - \frac{1}{\tau_E} \right)} - 1 \right) \right] + \\
&\quad + \frac{T_{2,e}}{\tau_{es}} \cdot \left[ e^{t \left( \frac{1}{\tau_M} - \frac{1}{\tau_E} \right)} - 1 \right].
\end{aligned}$$

We can now define  $T_2 := T_{2,e} \cdot \tau_M / \tau_{es}$  and receive the final result

$$\begin{aligned} T_s(t) &= T_1 + \frac{1}{\tau_E - \tau_M} \cdot \left[ (T_1 \tau_M - T_2 \tau_E) \cdot e^{-\frac{t}{\tau_M}} + (T_2 - T_1) \tau_E \cdot e^{-\frac{t}{\tau_E}} \right] \quad (\text{A.11}) \\ T_1 &= \frac{P_0}{C_e + C_l}, \quad T_2 = \frac{P_0 \cdot g_{el-sp}}{C_e (g_{el-sp} + g_{lat-sp})}, \quad P_0 = \frac{\alpha_{abs} F}{d}. \end{aligned}$$

To obtain the solution for a realistic pulse which we will use as our fitting formula, we will convolute (A.11) with the Gaussian pulse (A.5) as we did with the solution of the 2TM (A.4). Again, calculation is straightforward and yields

$$\begin{aligned} [T_s * G](t) &= T_1 \cdot \text{step}_0(t) + \frac{T_1 \tau_M - T_2 \tau_E}{\tau_E - \tau_M} \cdot \text{step}_M(t) \cdot e^{-\left(\frac{t}{\tau_M} - \frac{w^2}{8\tau_M^2}\right)} + \\ &+ \frac{(T_2 - T_1) \tau_E}{\tau_E - \tau_M} \cdot \text{step}_E \cdot e^{-\left(\frac{t}{\tau_E} - \frac{w^2}{8\tau_E^2}\right)} \quad (\text{A.12}) \end{aligned}$$

The step function  $\text{step}_M$  is defined analogously to  $\text{step}_E$ :

$$\text{step}_M(t) = \frac{1}{2} \cdot \left( 1 + \text{erf} \left\{ \frac{\sqrt{2}t}{w} - \frac{\sqrt{2}w}{4\tau_M} \right\} \right)$$

The constants appearing in Eq. (A.12) are connected to the fundamental parameters as follows:

$$\begin{aligned} \tau_E &= \left( g_{el-lat} \cdot \frac{C_e + C_l}{C_e C_l} \right)^{-1}, \quad \tau_M = \left( \frac{g_{el-sp} + g_{lat-sp}}{C_s} \right)^{-1} \\ T_1 &= \frac{P_0}{C_e + C_l}, \quad T_2 = \frac{P_0 \cdot g_{el-sp}}{C_e (g_{el-sp} + g_{lat-sp})}, \quad P_0 = \frac{\alpha_{abs} F}{d} \end{aligned}$$

Note that  $\tau_M$  depends on  $C_s$ , which is important for the range near  $T_C$ , where  $C_s$  increases dramatically, as discussed in chapter 3.4.

### A.3. Solution of the 3TM for high polarization $P$

Now we will treat the case where we have to obtain the demagnetization time  $\tau_M$  for the case of high polarization  $P$ . It is hardly feasible to use the complete analytical solution (A.12) of the 3TM, because the measurements hardly show the distinct double-exponential behavior in this case and the high number of parameters makes it hard to receive a good result from the fit. Therefore it is more convenient to use a different approach for this case, making use of the fact that

the demagnetization time  $\tau_M$  is included in the slow exponential rise of the spin temperature observed for high  $P$ . Consider the 3TM for a material of high  $\tau_M$  for times clearly after the pump pulse has arrived. In particular, we will assume that the electron system has already equilibrated with the lattice to a common temperature  $T = T_e = T_l$ . For e.g. nickel this is the case for delay times of about  $5\text{ ps}$ , which is considerably below the demagnetization time for high polarization.

In contrast to the considerations above we will not assume  $C_s \ll C_e, C_l$  in the following. In this case the 3TM reads as follows:

$$(C_e + C_l) \cdot \frac{dT}{dt} = (g_{el-sp} + g_{lat-sp}) \cdot (T_s - T) \quad (\text{A.13})$$

$$C_s \cdot \frac{dT_s}{dt} = (g_{el-sp} + g_{lat-sp}) \cdot (T - T_s) \quad (\text{A.14})$$

Using the relations  $(g_{el-sp} + g_{lat-sp}) = C_s/\tau_M$  and  $C_e + C_l + C_s = C$  we can transform the system to a more convenient form:

$$\frac{d(T - T_s)}{dt} = -\frac{C}{C_e + C_l} \cdot \frac{T - T_s}{\tau_M} \quad (\text{A.15})$$

$$(C_e + C_l) \cdot \frac{dT}{dt} + C_s \cdot \frac{dT_s}{dt} = 0 \quad (\text{A.16})$$

The latter equation simply yields  $(C_e + C_l) \cdot T + C_s \cdot T_s = P_0 = \text{const.}$ , because the complete pulse energy has already been absorbed. The former equation is trivial and has the solution

$$A_0 + A_1 \cdot e^{-\frac{C}{C_e + C_l} \cdot \frac{t}{\tau_M}}.$$

The constant  $A_0$  can be dropped because we demand  $T = T_s$  for  $t \rightarrow \infty$ . The constant  $A_1$  is not easily assigned a physical meaning, but this is not really necessary either. Using the abbreviation  $T_1 = P/C$  we can write our result in the form

$$T(t) = T_1 + A_1 \cdot \frac{C_s}{C} \cdot e^{-\frac{C}{C_e + C_l} \cdot \frac{t}{\tau_M}}, \quad (\text{A.17})$$

$$T_s(t) = T_1 - A_1 \cdot \frac{C_e + C_l}{C} \cdot e^{-\frac{C}{C_e + C_l} \cdot \frac{t}{\tau_M}}. \quad (\text{A.18})$$

If the equilibrium temperature can be determined separately,<sup>46</sup> it will only have two fitting parameters, namely  $A_1$  and the exponent. Note, however, that the exponent does not directly reflect  $\tau_M$ , but is weighted by the ratios of the specific

---

<sup>46</sup> This is the case if the system reaches equilibrium clearly before diffusion has a significant effect, so the fitting range can be kept short. Therefore, it is somewhat unlikely in this case.

## Appendix A. Explicit calculations

---

heats, which will enlarge the error for the determination of the demagnetization time and thus  $P$ . In general, we expect to underestimate  $\tau_M$ .

# Appendix B.

## Technical details

### B.1. Calculation of the laser fluence

In this section we will show how the laser fluences  $F$  given in this thesis were calculated. While this may seem to be a trivial task, past publications show extreme differences in the range of fluences given, but most of them do not give any insight on how the numbers were obtained. However, knowledge of the (absorbed) fluence is important if one tries to compare experimental data to simulations based on the 3TM. For example, Beaurepaire gave in his original publication [BMDB96] a value of  $F = 7 \text{ mJ/cm}^2$ , stating that fluences slightly higher would irreversibly damage his nickel samples. On the other hand, in this work and in previous publications [Djo06, Mül07] values of about  $50 \text{ mJ/cm}^2$  are given with proof that Ni samples did not take any damage from exposure.

As we already mentioned in chapter 3.5, we assume our beam profile to be Gaussian with a width of  $d_\sigma = 2\sigma$  of approximately  $60 \mu\text{m}$ . To calculate the fluence  $F$  we use the simplifying assumption that the incident laser power  $P_0$  is distributed homogeneously over a circle of diameter  $d_\sigma$ . This is a good approximation, because most of the power of a beam with Gaussian profile is concentrated in the  $d_\sigma/2 = 1\sigma$  interval. The fluence of the incident pulses with frequency  $f$  is then simply calculated according to the formula

$$F = \frac{P_0}{A \cdot f} = \frac{4P_0}{\pi d_\sigma^2 f} \quad (\text{B.1})$$

It is important to note that  $P_0$  is the power of the laser beam actually arriving at the sample. Therefore, it has been measured directly in front of the sample, behind the chopper in Fig. 3.14(b). The chopper had been switched off while assuring that the beam could pass the chopper unclipped.<sup>47</sup>

---

<sup>47</sup> In our setup, the losses for the pathway the beam has to travel from the polarizer used to set the power to the sample add up to approximately 50%.

## B.2. Comments on data processing

Of the various challenges one has to face when evaluating femtosecond pump-probe measurements, we shall briefly discuss the two issues which are most important for the evaluation of the data presented in chapter 4. First, the measured Kerr rotation  $\theta_K$  contains in general both symmetric and asymmetric contributions with respect to the reversal of the magnetization  $\vec{M}$ . As stated by Koopmans [Koo03], the Kerr rotation can be decomposed into these two contributions,

$$\theta_K = \theta_s + \theta_a$$

and the asymmetric part  $\theta_a$  which contains the (linear) magnetic contributions can be extracted by performing measurements at opposite directions of the applied field  $\vec{H}$ , leading to states of opposite magnetization  $\vec{M}$ . The difference between those measurements then yields the asymmetric part,

$$\theta_K(\vec{M}) - \theta_K(-\vec{M}) = 2\theta_a(\vec{M}).$$

This method has been applied to *all* measurements in this thesis to extract the Kerr signals given as results.

However, some of the data provided still contain contributions from the symmetric part  $\theta_s$ . This part includes the autocorrelation signal of the pump and probe pulses, which arises around a delay time  $\Delta\tau \approx 0$  and whose width is of the order of the pulse length  $w$ . If  $\theta_s$  is large compared to  $\theta_a$ , the process of measuring at opposite directions of field is very sensitive to small deviations from the ideal of measuring at exactly opposite fields while keeping all other parameters fixed. If, for example, the noise of the measurement has a certain level or the second measurement (with reversed field) has an offset in the delay time  $\Delta\tau$  due to mechanical inaccuracies of the delay stage, there will still be a remnant from the autocorrelation artifact visible in the difference  $\theta_K(\vec{M}) - \theta_K(-\vec{M})$ . An example for such remnants can be seen in Fig. 4.24(b).

The second point of concern for the evaluation is the fitting of the analytical solution of the 3TM to the experimental results. For this purpose, Eq. (A.12) is used, which contains five parameters by itself (two temperatures  $T_1$  and  $T_2$ , two timescales  $\tau_M$  and  $\tau_E$  and the pulse width  $w$ ), and for the actual fitting process two additional parameters, an offset  $T_0$  for the temperature and an offset  $t_0$  for the delay time, have to be regarded. While the temperature offset  $T_0$  and the pulse width  $w$  are kept fixed, the remaining five parameters have to be fitted to the data. For the fitting, a common implementation of the Levenberg-Marquardt

algorithm is used. However, an actual fit, i.e. the fitting of all parameters at once in order to reduce the  $\chi^2$  value as much as possible, is barely possible. Not only is it a great numerical effort, but it is also not given that the result of minimal  $\chi^2$  fits the data well. This is a result of the strong correlation between the fit parameters of this highly non-linear, especially between the temperatures and the timescales. In addition, the results of the fit strongly depend on the chosen fitting interval, mostly due to the fact that a longer fitting interval contains the onset of diffusion, but the fitting interval must not be shortened to the regime of the timescales that have to be extracted. While a full fit of the data therefore is not gainful, reproducible results of satisfactory accuracy are received following the certain procedure:

1. The fit interval has to be chosen in a way to ensure that the main features predicted by the 3TM, i.e. the exponential demagnetization and relaxation, are included. A good compromise between this required minimal length and the greatest possible reduction of influences from the diffusion are several picoseconds, if the sample does not show a strong slowing down of the demagnetization. In the latter case, the solution of the 3TM for high polarizations  $P$  discussed in chapter A.3 can be used.
2. The parameters are fitted step by step. The problem of high correlations is eliminated, if one fits the temperatures and the timescales separately. The procedure has to be repeated several times until stable results are achieved. The offset  $t_0$  of the delay time is estimated from the slope of the demagnetization curve and kept fixed for the first few fitting iterations. It is then expected to remain stable when included in the fit, otherwise the results can not be accepted and a different set of starting values has to be chosen.
3. So far the procedure will yield results in a local minimum for  $\chi^2$ . There is no guarantee, however, that this local minimum is reached by the correct values of the timescales. This is again a problem of high correlation of the fit parameters. Since the parameter of interest is the demagnetization time  $\tau_M$ , a 'manual' check of the fit result is performed: The curve produced by the fit has to match the data in its important features. This means that the demagnetization and the first part of the relaxation of the experimental data have to be matched by the fitted curve. Such a procedure is reasonable since these parts contain the actual information on the dynamics. A good criterion to ensure that the check yields reproducible data is that the maximum of

the fitted curve has to match the point of maximum demagnetization in the experimental data.

Following this procedure, results are obtained that are quite stable to starting the fit with a different set of initial conditions. Experience shows that deviations are in the range of a few percent. It has to be noted, however, that when comparing data between fits of different sets of samples the fit interval has to be chosen as similar as possible, or otherwise the comparison may suffer from deviations of the fit parameters. Also, this discussion emphasizes the advantage of being able to determine some of the parameters by different methods, e.g. the relaxation time  $\tau_E$  from the reflectivity. This should be done whenever possible.

# Bibliography

- [ACFK<sup>+</sup>07] U. Atxitia, O. Chubykalo-Fesenko, N. Kazantseva, D. Hinzke, U. Nowak, and R. W. Chantrell. Micromagnetic modeling of laser-induced magnetization dynamics using the Landau-Lifshitz-Bloch equation. *Applied Physics Letters*, 91(23):232507, 2007.
- [Arg55] Petros N. Argyres. Theory of the Faraday and Kerr Effects in Ferromagnetics. *Phys. Rev.*, 97(2):334–, January 1955.
- [BMDB96] E. Beaurepaire, J.-C. Merle, A. Daunois, and J.-Y. Bigot. Ultrafast Spin Dynamics in Ferromagnetic Nickel. *Phys. Rev. Lett.*, 76(22):4250–, May 1996.
- [CJHA07] A. Conca, M. Jourdan, C. Herbort, and H. Adrian. Epitaxy of thin films of the Heusler compound  $\text{Co}_2\text{Cr}_{0.6}\text{Fe}_{0.4}\text{Al}$ . *Journal of Crystal Growth*, 299(2):299 – 302, 2007.
- [CP05] M. K. Choudhary and R. M. Potter. Heat Transfer in Glass-Forming Melts. In D. L. Pye, A. Montenegro, and I. Joseph, editors, *Properties of Glass-Formation Melts*. CRC Press, 2005.
- [CS04] J M D Coey and S Sanvito. Magnetic semiconductors and half-metals. *Journal of Physics D: Applied Physics*, 37(7):988–993, 2004.
- [CV02] J. M. D. Coey and M. Venkatesan. Half-metallic ferromagnetism: Example of  $\text{CrO}_2$  (invited). *Journal of Applied Physics*, 91(10):8345–8350, 2002.
- [Dal08] Francesco Dalla Longa. *Laser-induced magnetization dynamics*. PhD thesis, TU Eindhoven, 2008.
- [Djo06] Marija Djordjević. *Magnetization dynamics in all-optical pump-probe experiments: spin-wave modes and spin-current damping*. PhD thesis, University of Göttingen, 2006.

- [DLM<sup>+</sup>06] M. Djordjević, M. Lüttich, P. Moschkau, P. Guderian, T. Kampfrath, R. G. Ulbrich, M. Münzenberg, W. Felsch, and J. S. Moodera. Comprehensive view on ultrafast dynamics of ferromagnetic films. *physica status solidi (c)*, 3(5):1347–1358, 2006.
- [DM07] Marija Djordjević and Markus Münzenberg. Connecting the timescales in picosecond remagnetization experiments. *Physical Review B (Condensed Matter and Materials Physics)*, 75(1):012404, 2007.
- [Ell54] R. J. Elliott. Theory of the Effect of Spin-Orbit Coupling on Magnetic Resonance in Some Semiconductors. *Phys. Rev.*, 96(2):266–, October 1954.
- [FK01] Helmut Fischer and Helmut Kaul. *Mathematik für Physiker, Bd.1*. Teubner, 2001.
- [FKW<sup>+</sup>05] Gerhard H Fecher, Hem Chandra Kandpal, Sabine Wurmehl, Jonder Morais, Hong-Ji Lin, Hans-Joachim Elmers, Gerd Schonhense, and Claudia Felser. Design of magnetic materials: the electronic structure of the ordered, doped Heusler compound  $\text{Co}_2\text{Cr}_{1-x}\text{Fe}_x\text{Al}$ . *Journal of Physics: Condensed Matter*, 17(46):7237–7252, 2005.
- [GM07] I. Galanakis and Ph. Mavropoulos. Spin-polarization and electronic properties of half-metallic Heusler alloys calculated from first principles. *Journal of Physics: Condensed Matter*, 19(31):315213 (16pp), 2007.
- [HB96] W. Hübner and K. H. Bennemann. Simple theory for spin-lattice relaxation in metallic rare-earth ferromagnets. *Phys. Rev. B*, 53(6):3422–, February 1996.
- [HBG<sup>+</sup>07] J. Hamrle, S. Blomeier, O. Gaier, B. Hillebrands, H. Schneider, G. Jakob, K. Postava, and C. Felser. Huge quadratic magneto-optical Kerr effect and magnetization reversal in the  $\text{Co}_2\text{FeSi}$  Heusler compound. *Journal of Physics D: Applied Physics*, 40(6):1563–1569, 2007.
- [Hec05] Eugene Hecht. *Optik*. Oldenbourg, 2005.

- 
- [Hoh98] Julius Hohlfeld. *Ultrafast Electron-, Lattice- and Spin-Dynamics in Metals Investigated by Linear and Nonlinear Optical Techniques*, chapter 2.6, pages 24–32. VWF, 1998.
- [Ker77] John Kerr. On Rotation of the Plane of Polarization by Reflection from the Pole of a Magnet. *Philosophical Magazine*, 5:321–343, 1877.
- [KMDL<sup>+</sup>09] B. Koopmans, G. Malinowski, F. Dalla Longa, D. Steiauf, M. Fahnle, T. Roth, M. Cinchetti, and M. Aeschlimann. Explaining the paradoxical diversity of ultrafast laser-induced demagnetization. *Nat Mater*, advance online publication:–, December 2009.
- [Koo03] Bert Koopmans. Laser-Induced Magnetization Dynamics. In Burkard Hillebrands and Kamel Ounadjela, editors, *Spin Dynamics in Confined Magnetic Structures I*, volume 87 of *Topics in applied physics*, pages 256–323. Springer, 2003.
- [KRT<sup>+</sup>07] S.V. Karthik, A. Rajanikanth, Y.K. Takahashi, T. Ohkubo, and K. Hono. Microstructure and spin polarization of quaternary  $\text{Co}_2\text{Cr}_{1-x}\text{V}_x\text{Al}$ ,  $\text{Co}_2\text{V}_{1-x}\text{Fe}_x\text{Al}$  and  $\text{Co}_2\text{Cr}_{1-x}\text{Fe}_x\text{Al}$  Heusler alloys. *Acta Materialia*, 55(11):3867 – 3874, 2007.
- [Len08] Benjamin Lenk. Beobachtung von Damon-Eshbach-Moden mittels Femtosekundenspektroskopie. Diploma thesis, University of Göttingen, 2008.
- [LLH<sup>+</sup>06] Shandong Li, Meimei Liu, Zhigao Huang, Feng Xu, Wenqin Zou, Fengming Zhang, and Youwei Du. CoMnSb: A magnetocaloric material with a large low-field magnetic entropy change at intermediate temperature. *Journal of Applied Physics*, 99(6):063901, 2006.
- [LPRV08] Aitor F. Lopeandia, F. Pi, and J. Rodriguez-Viejo. Nanocalorimetric analysis of the ferromagnetic transition in ultrathin films of nickel. *Applied Physics Letters*, 92(12):122503, 2008.
- [LWM<sup>+</sup>09] H. Lee, Y.-H. A. Wang, C. K. A. Mewes, W. H. Butler, T. Mewes, S. Maat, B. York, M. J. Carey, and J. R. Childress. Magnetization relaxation and structure of CoFeGe alloys. *Applied Physics Letters*, 95(8):082502, 2009.
- [MAT02] Jacques Miltat, Goncalo Albuquerque, and Andre Thiaville. An Introduction to Micromagnetics in the Dynamic Regime. In Kamel
-

- Hillebrands, Burkard; Ounadjela, editor, *Spin Dynamics in Confined Magnetic Structures I*, volume 83 of *Topics in applied physics*, pages 1–33. Springer, 2002.
- [MCC08] S. Maat, M. J. Carey, and J. R. Childress. Current perpendicular to the plane spin-valves with CoFeGe magnetic layers. *Applied Physics Letters*, 93(14):143505, 2008.
- [Mey03] Gereon Meyer. *In situ Abbildung magnetischer Domänen in dünnen Filmen mit magnetooptischer Rasternahfeldmikroskopie*. PhD thesis, FU Berlin, 2003.
- [MFG84] O. E. Martinez, R. L. Fork, and J. P. Gordon. Theory of passively mode-locked lasers including self-phase modulation and group-velocity dispersion. *Opt. Lett.*, 9(5):156–158, 1984.
- [MLBZ89] E. R. Moog, C. Liu, S. D. Bader, and J. Zak. Thickness and polarization dependence of the magneto-optic signal from ultrathin ferromagnetic films. *Phys. Rev. B*, 39(10):6949–, April 1989.
- [MMMG08] G. M. Müller, M. Münzenberg, G.-X. Miao, and A. Gupta. Activation of additional energy dissipation processes in the magnetization dynamics of epitaxial chromium dioxide films. *Physical Review B (Condensed Matter and Materials Physics)*, 77(2):020412, 2008.
- [MMW79] M. Maszkiewicz, B. Mrygon, and K. Wentowska. Rounding of Specific Heat of Nickel near the Critical Temperature. *Physica Status Solidi (a)*, 54(1):111–115, 1979.
- [Mül07] Georg Müller. *Laser-induzierte Magnetisierungsdynamik in Halbleitern und ferromagnetischen Nanostrukturen*. Diploma thesis, University of Göttingen, 2007.
- [MWD<sup>+</sup>09] Georg M. Müller, Jakob Walowski, Marija Djordjević, Gou-Xing Miao, Arunava Gupta, Ana V. Ramos, Kai Gehrke, Vasily Moshnyaga, Konrad Samwer, Jan Schmalhorst, Andy Thomas, Andreas Hütten, Günter Reiss, Jagadeesh S. Moodera, and Markus Münzenberg. Spin polarization in half-metals probed by femtosecond spin excitation. *Nat Mater*, 8(1):56–61, January 2009.
- [OIBC<sup>+</sup>98] R. M. Osgood III, S. D. Bader, B. M. Clemens, R. L. White, and H. Matsuyama. Second-order magneto-optic effects in anisotropic

- 
- thin films. *Journal of Magnetism and Magnetic Materials*, 182(3):297–323, March 1998.
- [Ons31a] Lars Onsager. Reciprocal Relations in Irreversible Processes. I. *Phys. Rev.*, 37(4):405–, February 1931.
- [Ons31b] Lars Onsager. Reciprocal Relations in Irreversible Processes. II. *Phys. Rev.*, 38(12):2265–, December 1931.
- [PCF04] S. Picozzi, A. Continenza, and A. J. Freeman. Role of structural defects on the half-metallic character of  $\text{Co}_2\text{MnGe}$  and  $\text{Co}_2\text{MnSi}$  Heusler alloys. *Phys. Rev. B*, 69(9):094423, Mar 2004.
- [PHP<sup>+</sup>02] K. Postava, D. Hrabovský, J. Pištora, A. R. Fert, Š. Višňovský, and T. Yamaguchi. Anisotropy of quadratic magneto-optic effects in reflection. *Journal of Applied Physics*, 91:7293–7295, May 2002.
- [Sch00] Franz Schwabl. *Statistische Mechanik*, chapter 6.5.2, pages 290–301. Springer, 2000.
- [SFP98] A. J. Slifka, B. J. Filla, and J. M. Phelps. Thermal Conductivity of Magnesium Oxide From Absolute, Steady-State Measurements. *Journal of Research of the National Institute of Standards and Technology*, 103:357–363, 1998.
- [SHO<sup>+</sup>07] Y Sakuraba, M Hattori, M Oogane, H Kubota, Y Ando, A Sakuma, and T Miyazaki. Half-metallic band structure observed in  $\text{Co}_2\text{MnSi}$ -based magnetic tunnel junctions. *Journal of Physics D: Applied Physics*, 40(5):1221–1227, 2007.
- [SKRH05] J. Schmalhorst, S. Kammerer, G. Reiss, and A. Hütten. Inelastic electron tunneling spectroscopy and bias voltage dependence of magnetic tunnel junctions with polycrystalline  $\text{Co}_2\text{MnSi}$  electrode. *Applied Physics Letters*, 86(5):052501, 2005.
- [SRK<sup>+</sup>06] Mahdi Sargolzaei, Manuel Richter, Klaus Koepf, Ingo Opahle, Helmut Eschrig, and Igor Chaplygin. Spin and orbital magnetism in full Heusler alloys: A density functional theory study of  $\text{Co}_2\text{YZ}$  ( $Y = \text{Mn, Fe}$ ;  $Z = \text{Al, Si, Ga, Ge}$ ). *Physical Review B (Condensed Matter and Materials Physics)*, 74(22):224410, 2006.
-

## Bibliography

---

- [TGMT86] C. Thomsen, H. T. Grahn, H. J. Maris, and J. Tauc. Surface generation and detection of phonons by picosecond light pulses. *Phys. Rev. B*, 34(6):4129–4138, Sep 1986.
- [Vis86] S Vishnovsky. Magneto-optical permittivity tensor in crystals. *Czechoslovak Journal of Physics B*, 36:1424–1433, 1986.
- [Wal07] Jakob Walowski. Non-local/ local Gilbert damping in nickel and permalloy thin films. Diploma thesis, University of Göttingen, 2007.

# Acknowledgments

First of all I would like to thank Prof. Markus Münzenberg for providing me with the opportunity to work in his group. Not only did he propose the interesting topic of this thesis, but he was also always available to discuss the experiments and their results. I furthermore thank Prof. Thomas Pruschke for agreeing to work as secondary attester.

I enjoyed working in my group very much and would like to thank all of its members for their good collaboration and fellowship. In particular, I want to thank Benjamin Lenk and Jakob Walowski for introducing me to the experimental setup and spending many time with me working in the laboratory and interpreting the results.

All the samples investigated in this thesis have been provided by groups from external facilities. I would like to thank Dr. Andy Thomas, Daniel Ebke, and Dr. Jan Schmalhorst from the group of Prof. Günter Reiss at the University of Bielefeld for providing the  $\text{Co}_2\text{MnSi}$ ,  $\text{Co}_2\text{FeAl}$ , and  $\text{CoMnSb}$  samples and the structural data. The  $\text{CoFeGe}$  and  $\text{Co}_2\text{MnGe}$  samples have been provided by Hitachi Global Storage Technologies. Here, I want to thank Dr. Stefan Maat and Matthew J. Carey for their collaboration. I furthermore thank Dr. Jaroslav Hamrle (TU Kaiserslautern) for the discussion on the quadratic magneto-optic Kerr effect.

The thesis has been proofread by Felix Büttner, Benjamin Lenk, my brother Alexander Mann, and Jakob Walowski. I would like to thank all of them for this effort and all the suggestions they made for the script.

Lastly, I thank my parents for supporting my studies.